

The Pennsylvania State University

The Graduate School

Graduate Program in Acoustics

**MULTILAYER TRANSFER MATRIX CHARACTERIZATION  
OF COMPLEX MATERIALS WITH SCANNING ACOUSTIC MICROSCOPY**

A Thesis in

Acoustics

by

Jeong Nyeon Kim

© 2013 Jeong Nyeon Kim

Submitted in Partial Fulfillment  
of the Requirements  
for the Degree of

Master of Science

August 2013

The thesis of Jeong Nyeon Kim was reviewed and approved\* by the following:

Richard L. Tutwiler  
Senior Scientist,  
Associate Professor of Acoustics  
Thesis Co-Advisor

Bernhard R. Tittmann  
Schell Professor of ESM  
Thesis Co-Advisor

Victor W. Sparrow  
Professor of Acoustics  
Interim Head of Graduate Program in Acoustics

\*Signatures are on file in the Graduate School

## ABSTRACT

A multilayer structured thin film system, such as a biomedical thin film, Micro Electric Mechanical System (MEMS) / Nano Electric Mechanical System (NEMS) devices, and semiconductors, is widely used in various fields of industry. To non-destructively evaluate the multilayer structured thin film system, a mechanical scanning acoustic reflection microscope has been well recognized as a useful tool in recent years. Especially, the  $V(z)$  curve method with the scanning acoustic microscope is used to characterize the very small area of the system.

In this study,  $V(z)$  curve simulation software has been developed for simulating a transducer's output when we transmit an ultrasound wave into the specimen. In the software, the Thompson-Haskell transfer matrix method is applied to solve for the reflectance function. All input and output interfaces were incorporated in a Graphical User Interface (GUI) for users' convenience. Surface acoustic wave velocities were calculated from the simulated  $V(z)$  curves. For the precise calculation advanced signal processing techniques were utilized.

The surface acoustic wave velocity is compared to that from an experiment with a bulk solid. I also tested the simulation's thickness sensitivity by simulating models with different thicknesses in the nanoscale. A series of experiments with multilayered solids were carried out and the results were compared with the simulation results. It was the first time a comparison was performed of analytical versus experimental  $V(z)$  curves for a multilayered system. For the multilayered specimen, silicon (100) was used as a substrate. Titanium (thickness: 10 nanometer) and platinum (thickness: 100 nanometer) were deposited respectively.

## TABLE OF CONTENTS

LIST OF FIGURES .....	vi
LIST OF TABLES.....	viii
LIST OF SYMBOLS .....	viii
ACKNOWLEDGEMENTS.....	xi
Chapter 1 Introduction .....	1
1.1 Background .....	2
1.1.1 Multilayer Structured Thin Film Systems and Adhesive Condition.....	2
1.1.2 Conventional, Current, and Alternative Methods .....	3
1.2 Invention of Scanning Acoustic Microscopy and V(z) Curve Method.....	4
1.2.1 Scanning Acoustic Microscopy .....	4
1.2.2 V(z) Curve Method .....	5
1.3 Objectives.....	7
Chapter 2 Theory .....	8
2.1 Principle of Scanning Acoustic Microscopy .....	8
2.1.1 Pulse vs. Tone-Burst .....	9
2.1.2 Operating Principle of Scanning Acoustic Microscopy.....	11
2.2 V(z) Curve Method .....	14
2.2.1 Acquiring a V(z) Curve .....	15
2.2.2 V(z) Curve and Surface Acoustic Wave Velocity .....	16
2.2.3 Optimization of Measurement Precision.....	17
2.2.4 Mathematical Model for V(z) Curves.....	18
2.3 Reflectance Function in Multilayered Solids .....	28
Chapter 3 Simulation Software .....	35
3.1 Simulation of a V(z) Curve .....	36

3.1.1 Simulation Setup.....	36
3.1.2 Simulation Result.....	39
3.2 Calculation of Surface Acoustic Wave Velocity.....	40
3.2.1 STEP 1. Spatial Domain to Frequency Domain .....	41
3.2.2 Converting Frequency Axis to Velocity Axis.....	42
3.2.3 STEP 2. Frequency Domain to Spatial Domain .....	43
3.2.4 STEP 3. Spatial Domain to Frequency Domain .....	45
Chapter 4 Simulation and Experiment.....	47
4.1 Simulation vs. Experiment in bulk material (Silicon (100)) .....	49
4.2 Thickness Sensitivity of Simulation.....	51
4.3 Simulation vs. Experiment in Multilayered Materials .....	54
Chapter 5 Discussion and Future Works.....	57
Chapter 6 Conclusion.....	60
References.....	61
Appendix A $V(z)$ simulation software – Scripts and Functions .....	65
Appendix B Specifications of Acoustic Lenses .....	70
Appendix C $V(z)$ simulation software – Additional Features.....	78
Appendix D Material Properties .....	81

## LIST OF FIGURES

Figure 1-1. Olympus UH3, the scanning acoustic microscope used in this study. ....	5
Figure 2-1. <b>(A)</b> Simulated Pulse Signal vs. <b>(B)</b> Simulated Tone-Burst Signal. ....	9
Figure 2-2. Scanning Acoustic Reflection Microscopy. ....	11
Figure 2-3. Operating Flow of Scanning Acoustic Microscopy. ....	12
Figure 2-4. An ultrasonic image acquired by the Olympic UH3 scanning acoustic microscope with the operating setup parameters. ....	13
Figure 2-5. Decomposition of a $V(z)$ curve. ....	14
Figure 2-6. Graphical representation of steps to obtain a $V(z)$ curve ....	15
Figure 2-7. Calculation of surface acoustic wave velocity from the $V(z)$ curve. ....	16
Figure 2-8. Coordinate system and geometry to model the $V(z)$ curve. ....	19
Figure 2-9. Geometries when the ultrasonic beam is focused on the surface of the specimen (Left) and when it is defocused toward the specimen (Right). ....	26
Figure 2-10. Geometry of incident wave from coupling medium to the multilayered solid to model the reflectance function, $R(\theta)$ . ....	28
Figure 3-1. Initial view of the $V(z)$ simulation software. ....	35
Figure 3-2. Initial view of ‘Simulation Setup’ window (Right) and drop-down lists (Left). ....	36
Figure 3-3. Updated view of the ‘Simulation Setup’ window. ....	38
Figure 3-4. Simulation result. From the left to the right, acoustic fields in outgoing and incoming direction, amplitude and phase of the reflectance function, and a $V(z)$ curve of the given model. ....	39
Figure 3-5. Maximized $V(z)$ curve simulation figure. ....	39
Figure 3-6. Steps to calculate the surface acoustic wave velocity from a simulated $V(z)$ curve. ....	40
Figure 3-7. Selected portion (in the dotted box here, red in the software) of a simulated $V(z)$ curve for FFT. ....	41
Figure 3-8. Power spectrum of the selected signal. ....	42

Figure 3-9. Selection of a lobe (in the dotted box here, red in the software) for an inverse FFT.....	44
Figure 3-10. Inverse FFT of the selected lobe. ....	44
Figure 3-11. Selection of a portion (in the dotted box here, red in the software) of the signal for FFT.....	45
Figure 3-12. Surface acoustic wave velocity calculated from the $V(z)$ curve in Fig. 3-5.....	46
Figure 4-1. Crystalline orientation of different types of silicon.....	48
Figure 4-2. Two $V(z)$ curves from a simulation and an experiment for silicon (100). ....	49
Figure 4-3. Simulation models to examine the thickness sensitivity .....	51
Figure 4-4. Three $V(z)$ curve simulations of the models in Group 1.....	51
Figure 4-5. Two $V(z)$ curve simulations of the models in Group 1.....	52
Figure 4-6. A multilayered model for simulation (Left) and its real samples prepared for experiment (Right). ....	54
Figure 4-7. $V(z)$ curves obtained from the simulation and the experiment. ....	55
Figure A-1. Scripts and functions that construct the $V(z)$ simulation software.....	65
Figure A-2. Flow chart for a source code, Vz.m.....	66
Figure A-3. Flow chart for source codes, Vz_Function.m and Vz_Setup.m.....	67
Figure A-4. Flow chart for source codes, Vz_Vsaw_Calc1_FFT.m, Vz_Vsaw_Calc_Setup.m, and Vz_FFT_Calc.m.....	68
Figure A-5. Flow chart for source codes, Vz_Vsaw_Calc2_iFFT.m, Vz_Vsaw_Calc_Setup.m, and Vz_iFFT_Calc.m.....	69
Figure C-1. Usage example of the ruler icons. ....	78
Figure C-2. $V(z)$ curve vs. $V(z)$ curve figure window.....	79
Figure C-3. ‘OPEN Vz Curves’ dialog. ....	79
Figure C-4. Two selected $V(z)$ curves for comparison.....	80
Figure C-5. Selection of a $V(z)$ curve or both $V(z)$ curves to display.....	80

## LIST OF TABLES

Table 2-1. Terms in the $V(z)$ equation and their physical meanings and dependance.....	26
Table 4-1. Elastic properties of selected materials and parameters for simulation and experiment.....	47
Table 4-2. Surface acoustic wave velocity of silicon (100).....	50
Table 4-3. Surface acoustic wave velocities calculated from the $V(z)$ curves in Fig. 4-3.....	52
Table 4-4. Surface acoustic wave velocities calculated from the $V(z)$ curves in Fig. 4-4.....	53
Table 4-5. Surface acoustic wave velocities calculated from $V(z)$ curves in Fig. 4-6.....	55
Table B-1. Specification of AL1M3125 .....	70
Table B-2. Specification of AL2M3125 .....	71
Table B-3. Specification of AL2M631 .....	72
Table B-4. Specification of AL4M350 .....	73
Table B-5. Specification of AL4M631 .....	74
Table B-6. Specification of AL6M615 .....	75
Table B-7. Specification of AL8M607 .....	76
Table B-8. Specification of AL1G607.....	77
Table D-1. Properties of solid materials.....	81
Table D-2. Properties of plastic materials.....	90
Table D-3. Properties of liquids.....	92

## LIST OF SYMBOLS

$V_w$	Acoustic wave velocity in water (coupling media)
$V_{saw}$	Surface acoustic wave velocity
$V_{Lens}$	Acoustic wave velocity in acoustic lens
$V_L$	Longitudinal acoustic wave velocity in a solid material
$V_S$	Shear acoustic wave velocity in a solid material
$f$	Transducer's operating frequency



$\Delta z$	Space between minimal / peaks
$d$	Distance from transducer plane to back focal plane
$f_0$	Distance from back focal plane to lens curvature
$f_L$	Distance from lens curvature to front focal plane (focal length)
$z$	Distance from front focal plane to Specimen plane
$u_i^+$	Acoustic field on $i^{\text{th}}$ plane in outgoing direction in spatial domain
$u_i^-$	Acoustic field on $i^{\text{th}}$ plane in incoming direction in spatial domain
$U_i^+$	Acoustic field on $i^{\text{th}}$ plane in outgoing direction in frequency domain
$U_i^-$	Acoustic field on $i^{\text{th}}$ plane in incoming direction in frequency domain
$R_t$	Radius of transducer
$R_{ap}$	Radius of aperture
$R_c$	Radius of curvature
$k_w$	Wavenumber in water (coupling media)
$k_x$	x-component of wavenumber in water (coupling media)
$k_y$	y-component of wavenumber in water (coupling media)
$k_z$	z-component of wavenumber in water (coupling media)
$\lambda_w$	Wavelength in water (coupling media)
$k_{Lens}$	Wavenumber in acoustic lens
$\bar{c}$	$V_w / V_{Lens}$
$k_x^{'}$	x-component of wavenumber in acoustic lens
$k_y^{'}$	y-component of wavenumber in acoustic lens
$k_z^{'}$	z-component of wavenumber in acoustic lens
$k_r$	Radial component of wavenumber
$r$	Radial distance on transducer
$P_i$	Pupil function
$R$	Reflectance function
$*$	Convolution operation
$\theta_i$	Incident wave angle
$\theta_{ap}$	Aperture angle of acoustic lens
$\zeta$	Arbitrary point on x-axis in convolution operation
$\eta$	Arbitrary point on y-axis in convolution operation
$x^{'}$	Arbitrary point on x-axis

$y'$	Arbitrary point on y-axis
$\rho$	Density in water (coupling medium)
$\rho_n$	Density in $n^{\text{th}}$ layer of multilayered solid
$\alpha_n$	Longitudinal acoustic wave velocity in $n^{\text{th}}$ layer of multilayered solid
$\beta_n$	Shear acoustic wave velocity in $n^{\text{th}}$ layer of multilayered solid
$\phi_n$	Longitudinal wave potential in $n^{\text{th}}$ layer of multilayered solid
$\psi_n$	Shear wave potential in $n^{\text{th}}$ layer of multilayered solid
$k_{nx}$	x-component of wavenumber in $n^{\text{th}}$ layer of multilayered solid
$k_{an}$	Longitudinal wave vector of wavenumber in $n^{\text{th}}$ layer of multilayered solid
$k_{\beta n}$	Shear wave vector of wavenumber in $n^{\text{th}}$ layer of multilayered solid
$\eta_{an}$	z-component of $k_{an}$
$\eta_{\beta n}$	z-component of $k_{\beta n}$
$a_n, b_n, c_n, d_n$	Unknown constants in $\phi_n$ and $\psi_n$
$\{C_n\}$	unknown constant vector in $n^{\text{th}}$ layer of multilayered solid
$\omega$	Angular frequency
$\theta_n$	First critical angle of incident
$\gamma_n$	Second critical angle of incident
$u_n$	Tangential component of displacement vector in $n^{\text{th}}$ layer of multilayered solid
$v_n$	Normal component of displacement vector in $n^{\text{th}}$ layer of multilayered solid
$\sigma_n$	Tangential component of stress vector in $n^{\text{th}}$ layer of multilayered solid
$\tau_n$	Normal component of stress vector in $n^{\text{th}}$ layer of multilayered solid
$\{S_n\}$	Displacement & stress vector in $n^{\text{th}}$ layer of multilayered solid
$\mu_n$	Shear modulus (Lame's 2 <sup>nd</sup> parameter) in $n^{\text{th}}$ layer of multilayered solid
$f_{ps}$	Frequency in power spectrum
$Dz$	Total vertical distance of acoustic lens for $V(z)$ curve

## ACKNOWLEDGEMENTS

First and foremost, I would like to express my deep gratitude to my advisors, Dr. Richard Tutwiler and Dr. Bernhard Tittmann. Dr. Richard Tutwiler guided me throughout my master's research with great passion and patience. He has guided me not only with the research but also with qualities a graduate student should have. He has been a great advisor as well as an outstanding educator. Dr. Bernhard Tittmann introduced me to this fascinating field of academia and equipped me with fundamental knowledge and essential skills for further exploration. He also gladly allowed me to use any of his equipment including scanning acoustic microscope and acoustic lenses for the research. Their supervision made this work possible and successful.

The Graduate Program in Acoustics provided me with precious opportunities for learning from great scholars, and enabled me to perform at my best with this research. Moreover, it has been a warm nest to an international student. I would like to deliver my gratitude to Dr. Victor Sparrow, who is the chair of our program, for helping me settle back into an academic environment, and kindly accepting my request to have him as a committee member. I especially thank Karen Brooks, the former program coordinator, particularly for her kind help in finding solutions for when I had difficulties with personal and health issues. I also appreciate Karen Thal's help in resuming my graduate studies, and taking care of things involved with international graduate students' life in the U.S. I have never met such passionate scholars and students pursuing their professions before coming to the program. Even by interacting with them, I have been encouraged and inspired to do my best work.

I would like to thank the National Research Foundation of Korea (NRF) grant funded by the Korean government (MEST) and Dr. Ik Keun Park at Seoul National University of Science & Technology for providing me with an opportunity to work on this interesting and valuable research.

My special thanks to Dr. Chiaki Miyasaka for his passionate intellectual support. Dr. Chiaki Miyasaka always encouraged my curiosity related to the research. His knowledge about the scanning acoustic microscopy let this research have such a fruitful outcome.

I would like to thank Dr. Sanichiro Yoshida at Southeastern Louisiana University and Dr. Sourav Banerjee at the University of South Carolina. They provided me with valuable comments and great insight. Their comments shed light on future research for this field of study.

Special thanks to my friend, Mr. Dong Ryul Kawk, a visiting Ph. D candidate from Seoul National University of Science & Technology. He is a great experimentalist and helped me with all the experiments throughout the research. Without him, this research would have never been smooth as it is.

I also would like to thank John Mulry for correcting my English. I can image how much of a hassle it was. Yet, John Mulry delightfully accepted my favor and diligently edited my written English in this thesis.

I would like to thank my parents for the financial and emotional support for all these years of graduate school. Without their support, this journey could not have been possible. My father who is a successful engineer, inspired me to be a good scientist and engineer with solid responsibility and endless curiosity. My mother always supports me with warm words from afar and it has been sufficient fuel for me to deal with graduate school life.

Most of all, I wish to thank my wife, Seung Eun Lee for her never-ending support and silent but huge encouragement. She has been a wonderful companion ever since, and lifted me up to be a responsible man. Without her, I would have never been able to keep moving forward and reach this point.

**I dedicate this thesis to the memory of Dr. Chiaki Miyasaka, a great scientist, a highly devoted and passionate educator, and dear friend.**

## **Chapter 1**

### **Introduction**

Efforts of finding an alternative method to evaluate multilayer structured thin film systems without compromising their functionalities have triggered this study. To satisfy the major premise, and not to compromise or damage the functionalities, scanning acoustic microscopy has been remarked as a promising tool for characterization and analysis of such systems for the following reasons. First, scanning acoustic microscopy is non-destructive. Second, scanning acoustic microscopy can visualize both the surface and the subsurface of materials with a high degree of resolution (in micrometer scale) without any special treatment to the specimens. Third, the propagation of acoustic waves is directly related to the elastic properties of the materials, which allow quantitative determination of the elastic properties. To effectively and aggressively take advantages of these distinct features in assessment of multilayer structured thin film systems, especially adhesive status,  $V(z)$  curve simulation software which simulates transducer output when an ultrasonic wave is transmitted into the specimen has been developed through this study.

In this chapter, multilayer structured thin film systems and the assessment of their adhesive condition are described to provide background. Then, a brief history of the advent of scanning acoustic microscopy and the  $V(z)$  curve method are introduced. Lastly, the objectives of this study are stated.

## **1.1 Background**

### **1.1.1 Multilayer Structured Thin Film Systems and Adhesive Condition**

Multilayer structured thin film systems are extensively used in many applications due to their certain advantages, enhanced resistance to different types of damages, and reduced electrical resistance, friction, and special magnetic or dielectric properties. MEMS/NEMS devices, semiconductors, biosensors, data storages, solar cell, and thin film coatings are good examples of thin film systems.

Inspecting the multilayer structured thin film systems and assuring their functionalities have become important tasks because of their wide usages and significant roles. There are critical issues in the evaluation of the multilayer structured thin film systems including adhesive strength, yield strength, tensile strength, creep properties, and young's modulus.

Among the issues, adhesive strength between substrate and thin film is more emphasized for the following reasons [1]. First, the thin film, which is usually less than 1  $\mu\text{m}$  or the order of 50 nm for some applications, is so fragile that it must be supported by a more substantial substrate, and the adhesion of the two materials determines how much strength of the substrate can be shared with the film. Second, adhesion is a critical factor to establish the durability and longevity of thin film devices. Third, the structural quality of the film and the kinetics of their growth during the vacuum deposition process can be subjected to adhesion to the substrate in significant degree. For example, if the cohesion energy of film particles exceeds the adhesion energy between the substrate and the film, the film structure can be aggregated. Fourth, in some applications, films are desired to be cleaned and polished to allow for good adhesion as well as resistance to corrosion. Fifth, in surface chemistry and physics, adhesion is a fundamental parameter because it depends on inter-atomic and intermolecular forces. There are more reasons

than stated above but in this thesis the above reasons are considered adequate background information.

### **1.1.2 Conventional, Current, and Alternative Methods**

In early research, pull-off tests and peel tests were applied to evaluate the adhesive condition of multilayer structured thin film systems. Currently, the scratch test is the most commonly used technique to evaluate the adhesive condition. The scratch test is precise and provides quantitative results of an adhesion test. Yet, since it is a destructive method, as the two mentioned methods, it has certain drawbacks. The films' functionality cannot be maintained and the test could cause damage on the materials.

Through much research [2]-[24], alternative methods to evaluate the elastic properties of multilayer structured thin film systems have been proposed to overcome the disadvantages of the conventional and the current techniques. The  $V(z)$  curve method of scanning acoustic microscopy stands out [13]-[25] as a suitable tool due to its advantages. The advantages are, first and foremost, scanning acoustic microscopy is non-destructive. Second, scanning acoustic microscopy can visualize both the surface and the subsurface of materials with a high degree of resolution (in micrometer scale) without any special treatment to the specimens. Third, the propagation of acoustic waves is directly related to the elastic properties of the material which allows scanning acoustic microscopy to have quantitative determination of the elastic properties.

## **1.2 Invention of Scanning Acoustic Microscopy and V(z) Curve Method**

Development of scanning acoustic microscopy and the V(z) curve method in early stages are briefly introduced. More information on recent research related to evaluation of thin film systems can be found in the references.

### **1.2.1 Scanning Acoustic Microscopy**

S. Y. Sokolov suggested the possibilities of scanning acoustic microscopy and its advantages over conventional optical microscopes in 1949 [26]. He implied that the microstructure of a material could be visualized by using ultrasound with frequencies close to 3 GHz or higher. Yet, due to a lack of related technologies, the invention of such a microscope was delayed.

R. A. Lemons and C. F. Quate introduced the first scanning acoustic microscope in 1974 [27]. The first application of scanning acoustic microscope was transmission mode which places its specimen between two acoustics lenses. It is good for imaging thin specimens like biological samples but not for specimens with considerable thickness.

A. Atalar designed the reflection mode scanning acoustic microscope in 1977 [28]. Since its invention it has been accepted as a standard tool for imaging surfaces and subsurfaces of thick samples in industry.

R. D. Weglein found that unique acoustic signatures in different materials could be obtained by the V(z) curve method in reflection mode scanning acoustic microscopy in 1979 [29]. Since then, scanning acoustic microscopy has been equipped with not only imaging ability but also the capability of evaluating quantitative elastic properties of materials.



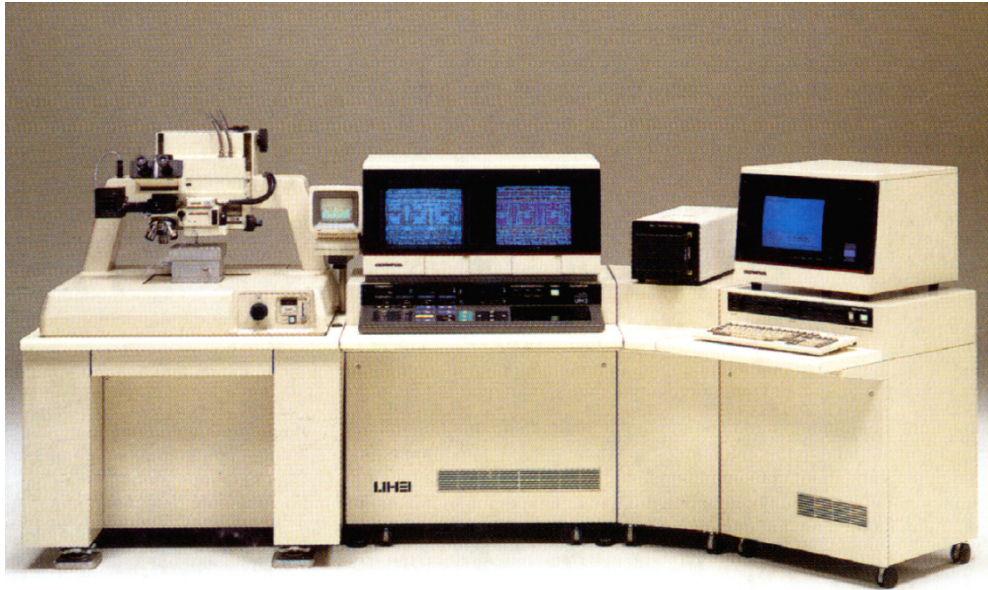


Figure 1-1. Olympus UH3, the scanning acoustic microscope used in this study.

### 1.2.2 $V(z)$ Curve Method

H. L. Bertoni et al. proposed a theoretical model that explained phenomena observed when an acoustic wave traveled from a liquid to the surface of a solid at or near the Rayleigh angle in 1973 [30].

M. A. Breazeale et al. experimentally proved Bertoni et al.'s theory which assumes that the incident wave resonantly couples with a leaky surface wave at the Rayleigh angle and the coupled energy interferes in the propagation of specularly reflected energy. The study also revealed that the reflected wave profile of a water-steel interface and that of a water-aluminum interface were distinctively different [31] in 1977.

A. Atalar et al. found that with changing the axial position of the sample, scanning acoustic microscopy can be used to study elastic properties of the surface and subsurface of materials and presented  $V(z)$  curves for the first time [28] in 1977.

A. Atalar also modeled the phenomena by using the angular spectrum approach in 1978 [32]. He applied Fourier transformations [33] to decompose the converging beam into a spectrum of plane waves.

R. D. Weglein revealed that the periodic variation of the interference phenomenon between the coupled energy of the incident wave with leaky surface waves and the energy of specularly reflected waves is uniquely material dependent. Moreover, in this study he showed the periodic null spacing ( $\Delta z$ ), which corresponds to the periodic variation in  $V(z)$  curves, is a function of Rayleigh wave velocity of materials. Thus, he proved that the  $V(z)$  curve method is a powerful tool to quantitatively evaluate elastic properties of materials in 1979 [29].

W. Parmon et al. modeled the interference phenomenon with a ray tracing method and proposed a mathematical model to calculate the spacing between minima ( $\Delta z$ ) in 1979 [34].

In the 1980's, there also were various works to find mathematical and/or physical models of the  $V(z)$  curve method and its applications. R. G. Wilson studied acoustic material signatures in different composite layered surfaces [35]. T. Kundu et al. mathematically modeled the reflectance function for multilayered solids [36].

Now, a lot of studies have been conducted to improve SAM's performance in many ways and the  $V(z)$  curve method always plays a key role for quantitative measurement and evaluation in many areas of science and technology. T. Endo et al. proved the effectiveness of the  $V(z)$  method on film thickness measurement in the range of sub-microns to a few micrometers [37]. More recently, F. Zhang characterized the mechanical properties of nanostructured physical vapor deposited on diamond-like carbon ultra-hard coatings using a photoacoustic guided-wave technique and line-focused acoustic microscopy [38]. C. Miyasaka verified that scanning acoustic microscopy can be applied to a nanoscaled thin film system [39].

### 1.3 Objectives

Even though there have been many studies with scanning acoustic microscopy to characterize thin or thick film systems there have not been extensive studies on nanoscaled thin film systems. Hence, in this study, to broaden the application range of the  $V(z)$  curve method to a multilayered thin film system, a simulation software tool for calculating the output voltage of a transducer emitting ultrasound on non-layered and multilayered systems was developed. In the software, I applied Atalar's angular spectrum approach [32] with spatial Fourier transformation [33] to find the acoustic field and to calculate the  $V(z)$  equation. The Thompson-Haskell matrix transfer method was implemented to solve for the reflectance function in a multilayered solid [36][40]. To achieve a decent accuracy of the surface acoustic wave velocity calculation from the  $V(z)$  curves, advanced digital signal processing techniques were utilized [41][42]. The GUI was provided for users' convenience. To ensure the reliability and to test the thickness sensitivity of the simulation, I carried out a series of comparisons with experimental measurements in a bulk solid and multilayered systems as well as simulations with different models. The specimen, silicon (100) was used as a substrate. Titanium (thickness: 10 nanometers) and platinum (thickness: 100 nanometers) were deposited respectively.

## **Chapter 2**

### **Theory**

In this chapter the fundamental principle of scanning acoustic microscopy is described with the  $V(z)$  curve method and its mathematical representation. The reflectance function in a multilayered solid is explained which is essential in this study.

The scanning acoustic microscopy discussed in this context is reflection mode scanning acoustic microscopy with the tone-burst wave mode.

#### **2.1 Principle of Scanning Acoustic Microscopy**

A scanning acoustic microscope is an apparatus that uses ultrasound. A scanning acoustic microscope has capabilities of visualizing both the surface and subsurface of the specimen while the conventional optical microscope can only visualize the surface of the specimen. It also provides images of the specimen with high resolution and high contrast. The resolution is defined by the operating frequency of the acoustic lens and velocity of the ultrasonic wave in the coupling medium for surface imaging and wave velocity in the specimen for subsurface imaging. The contrast is determined by acoustic elastic properties and the topology of the specimen. In addition, with scanning acoustic microscopy, one can acquire quantitative data of the specimen's elastic properties. More details about the resolution, the contrast factors, and the acoustic lens can be found especially in references [39] and [43].

### 2.1.1 Pulse vs. Tone-Burst

In this application a tone-burst wave is applied while many other experiments use a pulsed wave in similar applications. Thus, here, the differences between tone-burst waves and pulsed waves and the advantages of using a tone-burst wave over a pulsed wave in the evaluation of multilayer structured thin film systems are described.

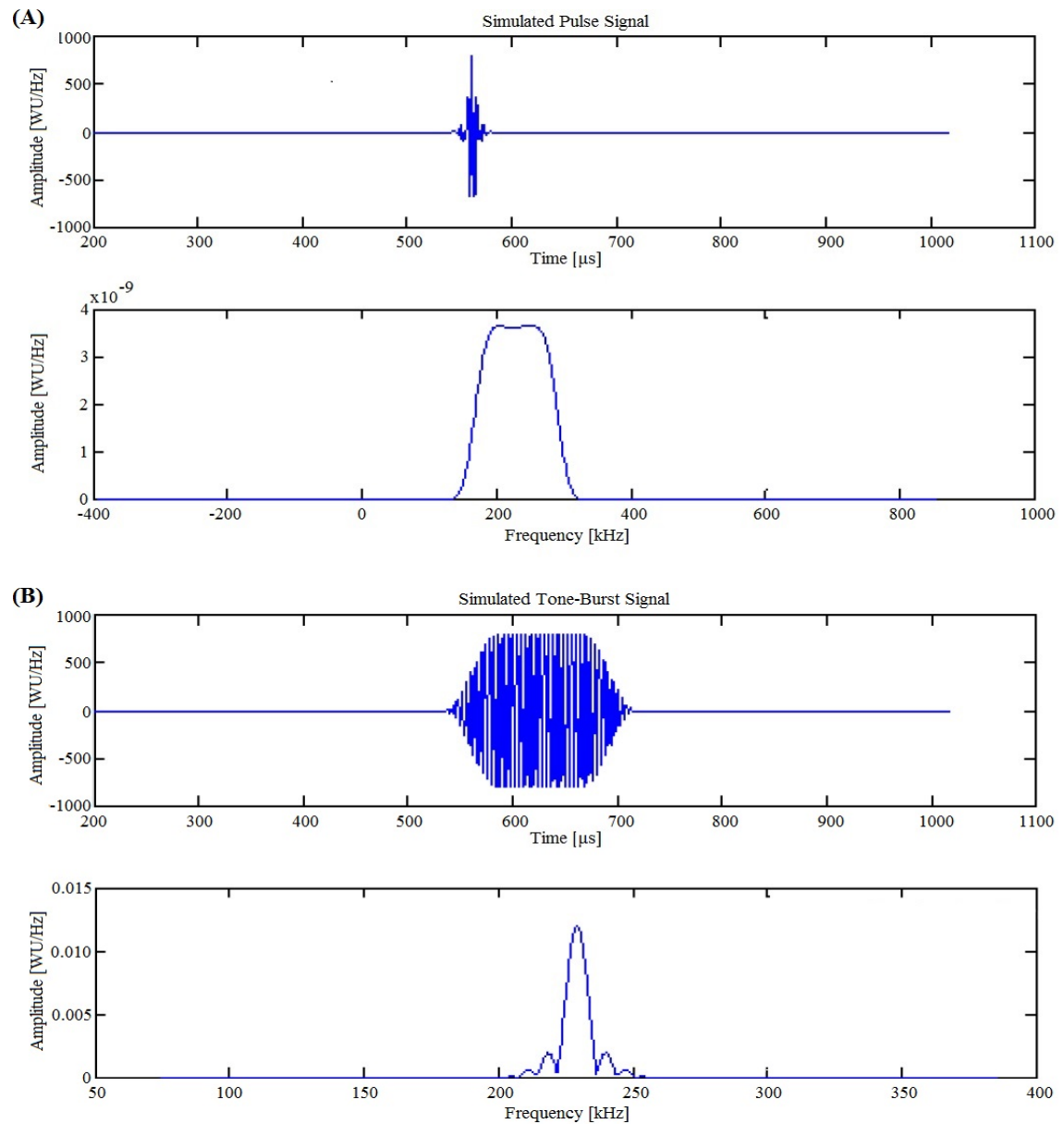


Figure 2-1. **(A)** Simulated Pulse Signal vs. **(B)** Simulated Tone-Burst Signal.

Figure 2-1 [44] shows a simulated pulse signal (A) and a simulated tone-burst signal (B) in both the time and frequency domains. In the time domain, the two signals have certainly different lengths of excitation periods. The length of the excitation period for both pulse and tone-burst depends on the designs of the system and the transducer. Yet, generally, tone-burst waves have apparently longer excitation periods (approximately 200 microseconds in Fig. 2-1 (B)) than pulse waves do (approximately 20 microseconds in Fig. 2-1 (A)). The different excitation period of the two input signals creates significant differences in many aspects.

First, the longer excitation periods require relatively smaller sampling rates. Therefore, with a rather modest sampling rate the long tone-burst can be precisely measured while a pulse wave generally requires a fast sampling rate. Second, the longer excitation of the tone-burst allows a larger amount of energy to be transmitted to the specimen compared to pulsed waves. That is, more energy can be received for post processing. Third, the longer duration also provides a better signal to noise ratio so that better quality results can be achieved. Fourth, since tone-burst signals tend to be well isolated in their analysis process, interfering reflections do not distort amplitude and time measurements. Fifth, in the frequency domain, a tone-burst signal has a significantly narrower bandwidth than the pulse wave does as Fig. 2-1 represents. This narrow frequency bandwidth allows precise frequency dependent measurements.

Due to the above reasons, a tone-burst signal is certainly more beneficial than a pulse signal especially when more is needed than simply detecting signals [44]. In this study, a 400 MHz operating frequency is mostly used to quantitatively evaluate elastic properties of specimens which have thicknesses of microns with no or multiple layers. And thus, applying a tone-burst is more suitable than applying a pulse wave.

### 2.1.2 Operating Principle of Scanning Acoustic Microscopy

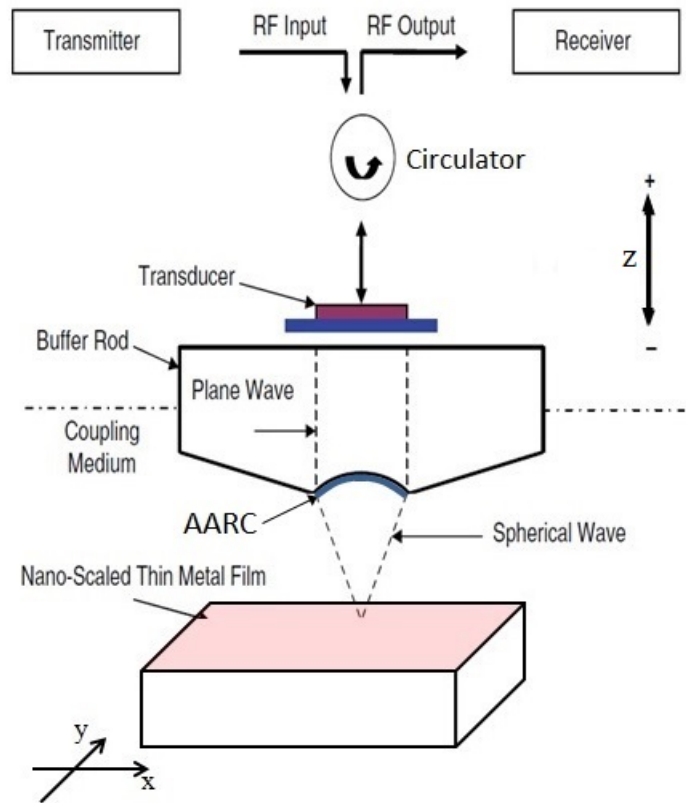


Figure 2-2. Scanning Acoustic Reflection Microscopy.

Figure 2-2 shows a schematic diagram of the scanning acoustic microscope. Its operating principle is described in the following, referring to Fig. 2-2.

A high power radio frequency (RF) signal, which is a tone-burst signal, is generated and sent into the system. The amplitude of the source signal is approximately 10 V. The tone-burst signal passes through the circulator which separates input and output signals. The input electrical signal vibrates the transducer located at the top of the buffer rod. Transducers for this application are usually fabricated with Zinc Oxide for its manufacturing advantages. The transducer transmits acoustic energy in the form of an ultrasonic plane wave into the buffer rod. Buffer rods are usually made from sapphire for fast propagation of the acoustic energy. The ultrasonic plane

wave travels through the buffer rod, and as it passes the aperture of the lens the wave transforms into a spherical wave, like an ultrasonic beam. On the aperture of lens there is anti-acoustic reflection coating, AARC as shown in the Fig. 2-2. The AARC compensates the impedance mismatching between the buffer rod and the coupling medium by acting as a matching layer. The ultrasonic beam propagates through the coupling medium, which is usually distilled water, and focuses onto the specimen. The ultrasonic beam is then reflected from the specimen, which carries the acoustic elastic information of the specimen. The reflected ultrasonic beam returns to the lens and transforms into an ultrasonic plane wave again as it passes through the aperture of the lens. The acoustic energy is converted back to an electrical signal through the transducer. The output voltage of the transducer has a ranging from 300 mV to 1 V when the input source is approximately 10 V at operating frequencies that range from 100 MHz to 1 GHz. This means there is approximately 30 dB to 80 dB of loss, and the output electric signal must be amplified by 30 dB to 80 dB to compensate for the loss. The amplitude of the compensated output signal is then interpreted by an image processing module and displayed at a certain point on a monitor. The process is for a single spot on the specimen and the flow is depicted in Fig. 2-3.

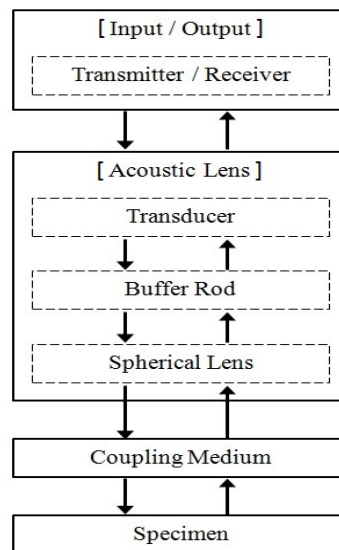


Figure 2-3. Operating Flow of Scanning Acoustic Microscopy.



To construct a two-dimensional ultrasonic image the specimen is mechanically scanned by moving the acoustic lens or the specimen stage. To visualize the surface of the specimen, the axial position ( $z$  in the Fig. 2-2) of the acoustic lens is set to the focal distance, which is usually denoted as  $z = 0 \mu\text{m}$ . To visualize the subsurface, the acoustic lens is mechanically moved down toward the specimen and defocuses the ultrasonic beam from the surface of the specimen and sets a new focal point under the surface. The new focal distance is usually denoted as  $z = -z \mu\text{m}$ . Figure 2-4 shows an example of ultrasonic image acquired by scanning acoustic microscopy with specific operating setup parameters. Scratches and other types of defects such as delaminations, which are in the size of microns, can be observed.

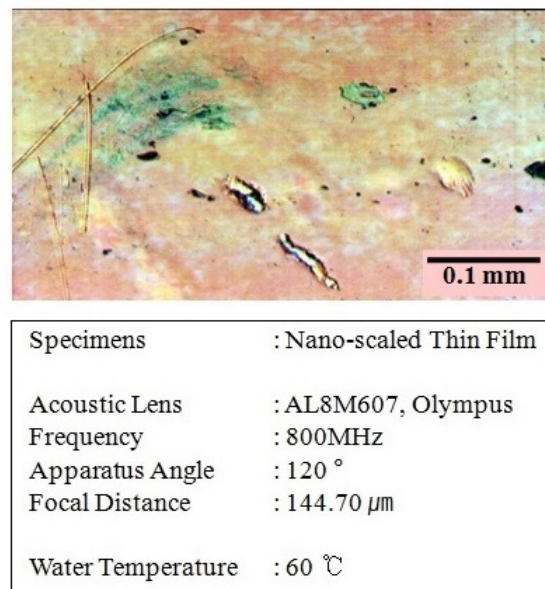


Figure 2-4. An ultrasonic image acquired by the Olympus UH3 scanning acoustic microscope with the operating setup parameters.

Note that the specimen in Fig. 2-4 is presented to demonstrate an ultrasonic image of scanning acoustic microscopy. Specimens used in this study did not have such defects and were used to evaluate acoustic elastic properties and adhesive conditions.

## 2.2 V(z) Curve Method

In addition to ultrasonic imaging, scanning acoustic microscopy has another feature, called V(z) curve analysis. A V(z) curve is a plot of the transducer's output voltage versus distance in the z-axis which is the vertical direction of the acoustic lens' movement. V(z) curve analysis utilizes the fact that the propagation of acoustic waves and the elastic properties of the material are directly related. How to obtain a V(z) curve is explained in the following sub-chapter.

The V(z) curve can be explained from the interference phenomena [30][31] which occur when an acoustic wave travels from a liquid to the surface of a solid at or near the Rayleigh angle. The coupled energy of an incident wave and a leaky surface acoustic wave at or near the Rayleigh angle affects the propagation of specularly reflected energy. The interference phenomena form the oscillation shape in the V(z) curve. Therefore, a decomposition of a V(z) curve consists of a longitudinal wave and surface acoustic wave components. Figure 2-5 shows a V(z) curve (A) and its decomposition into the longitudinal wave (B) and the surface acoustic wave (C) [42].

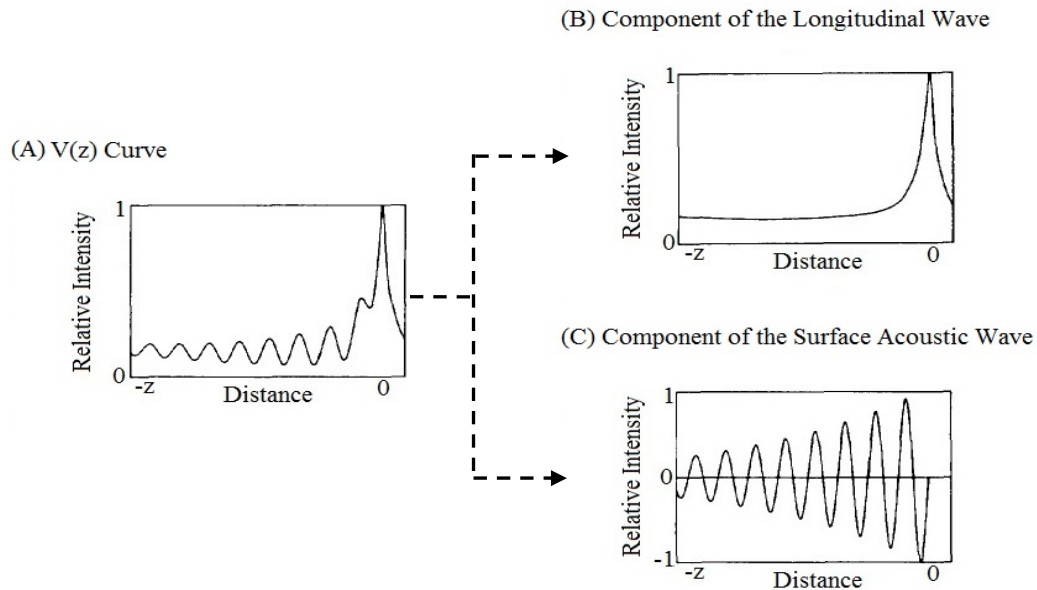


Figure 2-5. Decomposition of a V(z) curve.

### 2.2.1 Acquiring a $V(z)$ Curve

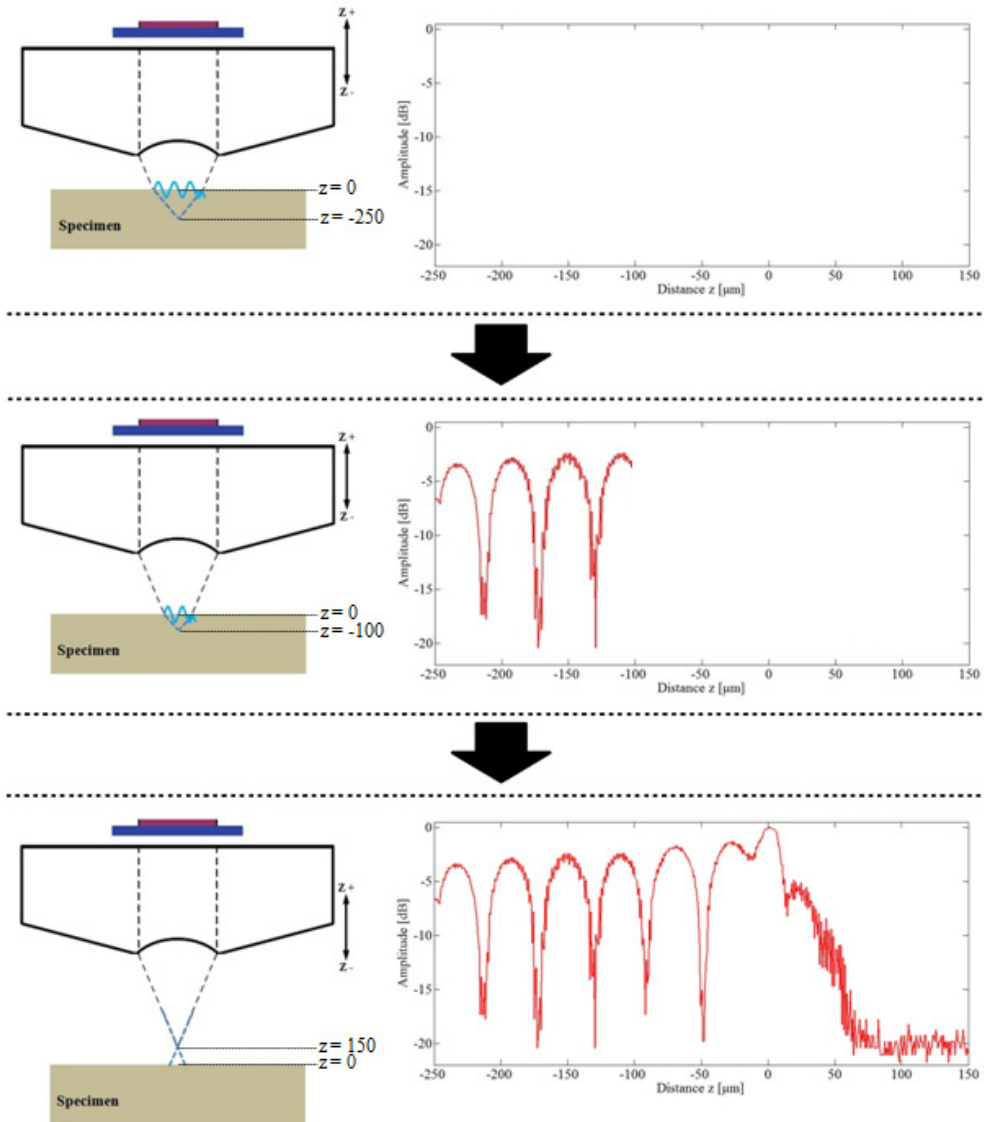


Figure 2-6. Graphical representation of steps to obtain a  $V(z)$  curve

Figure 2-6 graphically shows how to acquire a  $V(z)$  curve. First, move the acoustic lens down toward the specimen and defocus the acoustic beam. By doing so, a surface acoustic wave will appear on the specimen (Top in Fig. 2-6). Second, to generate a  $V(z)$  curve, move the

acoustic lens vertically up and display the output voltage of the transducer along with the vertical position of the acoustic lens. The interference phenomena discussed previously will give the oscillation shape to the  $V(z)$  curve (Middle in Fig. 2-6). Move the acoustic lens up as it passes its focal distance (Distance  $z = 0 \mu\text{m}$  in Fig. 2-6) and until the acoustic beam is totally defocused. As the lens reaches its focal distance, the amplitude of the  $V(z)$  curve is maximized due to the fact that more longitudinal waves are reflected back from the surface of the specimen (Bottom in Fig. 2-6). As the lens passes the focal distance and the beam starts to be defocused, the amplitude of the  $V(z)$  curve dramatically decreases (Bottom in Fig. 2-6).

### 2.2.2 $V(z)$ Curve and Surface Acoustic Wave Velocity

The primary purpose of taking a  $V(z)$  curve is to obtain the elastic properties of the material quantitatively. Since the  $V(z)$  curve represents the acoustic signature of the material, the acoustic-elastic properties, especially a surface acoustic wave velocity, can be calculated directly from the  $V(z)$  curve. The distance between minima ( $\Delta z$  in Fig. 2-7) of the  $V(z)$  curve is used to calculate the surface acoustic wave velocity of the material. Derivation details can be found in references [29], [34], [39] and [43]. Figure 2-7 shows the  $V(z)$  curve and the surface acoustic wave velocity equation.

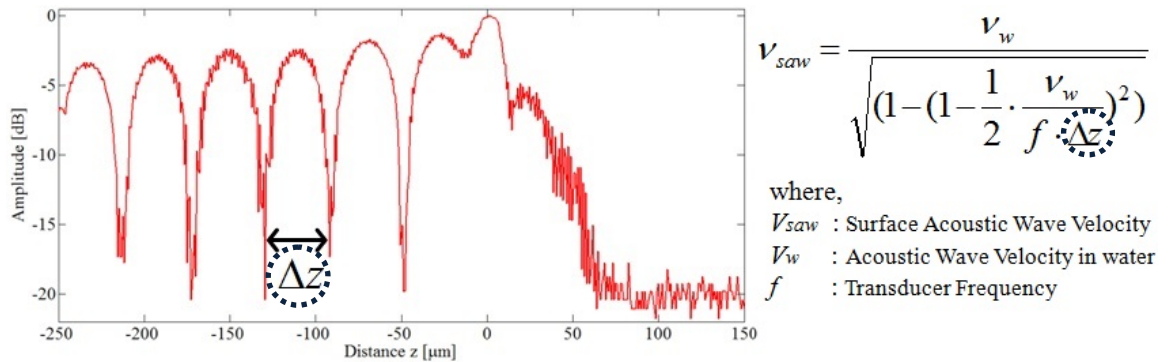


Figure 2-7. Calculation of surface acoustic wave velocity from the  $V(z)$  curve.

Again, the equation to calculate the surface acoustic wave velocity of the material from the space between minima in  $V(z)$  curves is

$$V_{saw} = \frac{V_w}{\sqrt{(1 - (1 - \frac{1}{2} \cdot \frac{V_w}{f \cdot \Delta z})^2)}} \quad (2.1a)$$

By assuming that  $1 \gg \frac{V_w}{f \cdot \Delta z}$  and taking squares in the both sides, Eqn. 2.1a can be simplified as shown below.

$$V_{saw} \cong \sqrt{V_w \cdot f \cdot \Delta z} \quad (2.1b)$$

### 2.2.3 Optimization of Measurement Precision

Before further exploration of the  $V(z)$  curves, the measurement precision should be discussed. By taking logarithms and differentiation of the two sides of Eqn. 2.1b, the following equation is acquired.

$$\frac{dV_{saw}}{V_{saw}} = \frac{1}{2} \frac{dV_w}{V_w} + \frac{1}{2} \frac{df}{f} + \frac{1}{2} \frac{d\Delta z}{\Delta z} \quad (2.2)$$

Equation 2.2 shows the error in the measurement of the surface acoustic wave velocity. The factors of the error are the acoustic wave velocity in the coupling medium ( $V_w$ ), the frequency of acoustic wave ( $f$ ), and the distance between minima ( $\Delta z$ ). Therefore, to minimize the error and enhance accuracy of the measurement the following procedure should be preformed. First, the temperature of the coupling medium should be constant to stabilize the acoustic wave velocity. Second, the acoustic lens should have a suitable operating frequency for the specimen with

narrow enough bandwidth. Third, the vertical movement of the acoustic lens should be accurately measured.

Many procedures to refine the measurement precision have been reported. Among of the many, the following are especially worth mentioning. Liang et al. developed a scanning acoustic microscope capable of obtaining complex  $V(z)$  curves based on a non-paraxial formulation of the  $V(z)$  integral and the reflectance function for a liquid-solid interface by inverting the  $V(z)$  curves formed at frequencies of 10 MHz or less[46]. Endo et al. improved the scanning acoustic microscopy mentioned above in terms of a mechanical movement and an increased frequency range up to 3 GHz for higher precision in the measurement [47].

A spherical lens is commonly used for ultrasonic imaging and quantitative data acquisition for elastic isotropic materials. However, the spherical lens may not provide information for materials which are not isotropic. Instead, a cylindrical lens, (a.k.a. line-focus lens) and a measurement method introduced by J. Kushibiki et al. for anisotropic materials was introduced, and the method is particularly useful for nanoscaled thin film systems with anisotropic substrates [42][48-52].

#### **2.2.4 Mathematical Model for $V(z)$ Curves**

Since one of the main objectives of this study is to simulate  $V(z)$  curves, its mathematical model should be thoroughly understood. In the simulation software the angular-spectrum approach of Atalar A. [32] is applied to calculate and display acoustic fields on the plane of the transducer, the back focal plane, the front focal plane, and the specimen, as well as the  $V(z)$  curve.

Figure 2-8 is the geometry of an acoustic lens with a specimen in the scanning acoustic microscope to mathematically model the  $V(z)$  curve. In Fig. 2-8, the transducer, back focal, front



The acoustic field  $u_0^+$  can be calculated by a Gaussian function [45] depending on the geometry of the transducer and acoustic properties of the buffer rod. The acoustic field  $u_1^+$  on the back focal plane (plane 1) can be calculated as below. Note that  $d$  is the distance from the transducer plane (plane 0) to the back focal plane (plane 1).

$$\begin{aligned} U_0^+(k_x, k_y) &= F\{u_0^+(x, y)\} \\ U_1^+(k_x, k_y) &= U_0^+(k_x, k_y)e^{(ik_z d)} \\ u_1^+(x, y) &= F^{-1}\{U_1^+(k_x, k_y)\} \end{aligned} \quad (2.4)$$

The acoustic field  $u_2^+$  on the front focal plane (plane 2) and the acoustic field  $u_1^+$  have the relation in Eqn. 2.5. Note that  $f_L$  is not frequency.  $f_L$  is the focal length in Fig. 2-8 in the following discussion.

$$u_2^+(x_2, y_2) = \frac{e^{ik_w f_L (1 + \bar{c}^2)}}{i\lambda_w f_L} \int_{-\infty}^{+\infty} \int_{-\infty}^{+\infty} u_1^+(x_1, y_1) P_1(x_1 + x_2, y_1 + y_2) e^{-i\frac{2\pi}{\lambda_w f_L}(x_1 x_2 + y_1 y_2)} dx_1 dy_1 \quad (2.5)$$

Where  $\bar{c} = \frac{V_w}{V_{Lens}}$ ,  $P_1$  is the pupil function which describes the shape of the lens, and

$$P_1(x, y) = \text{circ}\left\{\frac{\sqrt{x^2 + y^2}}{R_{ap}}\right\}. \text{ Since plane 2 is where the ray is focused we can legitimately}$$

suppose that  $x_2 \ll x_1$ ,  $y_2 \ll y_1$ . Then the pupil function can be simplified as  $P_1(x_1 + x_2, y_1 + y_2) \approx P_1(x_1, y_1)$ . Thus,  $u_2^+$  can be rewritten and  $U_2^+$  can be found as the following in Eqn. 2.6.

$$u_2^+(x_2, y_2) = \frac{e^{ik_w f_L (1 + \bar{c}^2)}}{i\lambda_w f_L} F[u_1^+(x_1, y_1) P_1(x_1, y_1)] \quad (2.6)$$



$$\begin{aligned}
U_2^+(k_x, k_y) &= F \left\{ \frac{e^{ik_w f_L (1+\bar{c}^2)}}{i\lambda_w f_L} F[u_1^+(x_1, y_1) P_1(x_1, y_1)] \right\} \\
&= i\lambda_w f_L e^{ik_w f_L (1+\bar{c}^2)} \\
&\quad \times u_1^+ \left\{ -\left(\frac{f_L}{k_w}\right) k_x, -\left(\frac{f_L}{k_w}\right) k_y \right\} P_1 \left\{ -\left(\frac{f_L}{k_w}\right) k_x, -\left(\frac{f_L}{k_w}\right) k_y \right\}
\end{aligned} \tag{2.7}$$

The acoustic field  $U_3^+$  on the specimen plane (plane 3) can be related with  $U_2^+$  on the front focal plane (plane 2) as below.

$$U_3^+(k_x, k_y) = U_2^+(k_x, k_y) e^{ik_z} \tag{2.8}$$

Here, since our case satisfies  $k_x^2 + k_y^2 \ll k_0^2$ , we can use the paraxial approximation which is

$$k_z = \sqrt{k_w^2 - k_x^2 - k_y^2} \approx k_w - \frac{1}{2} \left( \frac{k_x^2 + k_y^2}{k_w} \right) \tag{2.9}$$

Then,  $U_3^+$  can be rewritten as following.

$$U_3^+(k_x, k_y) = U_2^+(k_x, k_y) e^{ik_w z} e^{-i \left( \frac{k_x^2 + k_y^2}{2k_w} \right) z} \tag{2.10}$$

The incident acoustic wave is reflected on the specimen plane (plane 3) and the reflected acoustic field  $U_3^-$  can be determined from the incident acoustic field  $U_3^+$  on the same plane (plane 3). They are related by the reflectance function,  $R$ . The reflection function,  $R$  will be discussed in the following chapter.

$$U_3^-(k_x, k_y) = U_3^+(k_x, k_y) R \left( \frac{k_x}{k_w}, \frac{k_y}{k_w} \right) \tag{2.11}$$

We can find the acoustic field  $U_2^-$  on the front focal plane (plane 2) from the reflected acoustic field  $U_3^-$  and the previous relations. Then  $U_2^-$  and  $u_2^-$  can be found as shown below.

$$\begin{aligned}
 U_2^-(k_x, k_y) &= i\lambda_w f_L \cdot e^{ik_w f_L (1+\bar{c}^2)} u_1^+ \left\{ -\left(\frac{f_L}{k_w}\right) k_x, -\left(\frac{f_L}{k_w}\right) k_y \right\} \\
 &\times P_1 \left\{ -\left(\frac{f_L}{k_w}\right) k_x, -\left(\frac{f_L}{k_w}\right) k_y \right\} e^{i2k_w z} e^{-i\left(\frac{k_x^2 + k_y^2}{2k_w}\right) z} R\left(\frac{k_x}{k_w}, \frac{k_y}{k_w}\right)
 \end{aligned} \tag{2.12}$$

$$u_2^-(x, y) = F^{-1} \left\{ U_2^-(k_x, k_y) \right\} \tag{2.13}$$

Similarly with Eqn. 2.5 to Eqn. 2.7,  $u_1^-$  can be calculated as following.

$$\begin{aligned}
 u_1^-(x, y) &= \frac{e^{ik_w f_L (1+\bar{c}^2)}}{i\lambda_w f_L} P_2(x, y) F \left\{ u_2^-(x, y) \right\} \\
 &= \frac{e^{ik_w f_L (1+\bar{c}^2)}}{i\lambda_w f_L} P_2(x, y) U_2^-\left(\frac{k_w}{f_L} x, \frac{k_w}{f_L} y\right) \\
 u_1^-(x, y) &= -e^{i2k_w f_L (1+\bar{c}^2)} u_1^+(-x, -y) P_1(-x, -y) P_2(x, y) e^{-i\frac{k_w z}{f_L^2} (x^2 + y^2)} R\left(\frac{x}{f_L}, \frac{y}{f_L}\right)
 \end{aligned} \tag{2.14}$$

From the second equation in Eqn. 2.4,  $U_1^+(k_x, k_y) = U_0^+(k_x, k_y) e^{(ik_z d)}$ , the acoustic field  $u_1^+$  can be found in terms of  $u_0^+$  as shown below. Note that  $*$  represents the convolution operation and  $k_z'$  is z-component of the wave number in the buffer rod.

$$u_1^+(x, y) = u_0^+(x, y) * F^{-1} \left\{ e^{ik_z' d} \right\} \tag{2.15}$$

Similarly, the reflected acoustic field  $u_0^-$  on the transducer plane (plane 0) can be found in terms of  $u_1^-$  as below.

$$u_0^-(x, y) = u_1^-(x, y) * F^{-1} \left\{ e^{ik_z' d} \right\} \quad (2.16)$$

So far, the acoustic fields on each plane in both directions have been found. Now, the above equations will be utilized to expand the transducer's output voltage equation and find the  $V(z)$  equation. Equation 2.17 is the representation of the transducer's output voltage as a function of  $z$ , the distance between the front focal plane and the specimen plane.  $z=0$  when the front focal plane lies on the specimen plane.  $z=+z$  when the front focal plane is above the specimen plane.  $z=-z$  when the front focal plane is below the specimen plane, and the ultrasonic beam is focused in the specimen.

$$V(z) = \int_{-\infty}^{+\infty} \int_{-\infty}^{+\infty} u_0^+(x', y') u_0^-(x', y') dx' dy' \quad (2.17)$$

By substituting Eqn. 2.16 into Eqn. 2.17, it can be rewritten as shown below.

$$V(z) = \int_{-\infty}^{+\infty} \int_{-\infty}^{+\infty} u_0^+(x', y') \left\{ u_1^-(x', y') * F^{-1} \{ e^{ik_z' d} \} \right\} \Big|_{x=x' \& y=y'} dx' dy' \quad (2.18)$$

Equation 2.18 can be revised with the definition of convolution as shown below.

$$V(z) = \int_{-\infty}^{+\infty} \int_{-\infty}^{+\infty} u_0^+(x', y') \left\{ \int_{-\infty}^{+\infty} \int_{-\infty}^{+\infty} u_1^-(\xi, \eta) F^{-1} \{ e^{ik_z' d} \} \Big|_{x=x'-\xi \& y=y'-\eta} d\xi d\eta \right\} dx' dy' \quad (2.19)$$

By changing the order, Eqn. 2.19 can be rewritten as the following.

$$V(z) = \int_{-\infty}^{+\infty} \int_{-\infty}^{+\infty} u_1^-(\xi, \eta) \left\{ \int_{-\infty}^{+\infty} \int_{-\infty}^{+\infty} u_0^+(x', y') F^{-1} \{ e^{ik_z' d} \} \Big|_{x=x'-\xi \& y=y'-\eta} dx' dy' \right\} d\xi d\eta \quad (2.20)$$

Since  $k_z' = \sqrt{k_{Lens}^2 - k_x'^2 - k_y'^2}$  is an even function of  $k_x'$  and  $k_y'$ , the below relation is possible.

$$F^{-1}\{e^{ik'_z d}\}\Big|_{x=x'-\xi \& y=y'-\eta} = F^{-1}\{e^{ik'_z d}\}\Big|_{x=\xi-x' \& y=\eta-y'} \quad (2.21)$$

Here  $k'_x$  and  $k'_y$  are the x and y components of the wave number, and  $k_{Lens}$  is the wavenumber in the buffer rod.

From the Eqn. 2.21, it can be noticed that the integral inside the brackets in the Eqn. 2.20 is a convolution as shown below.

$$V(z) = \int_{-\infty}^{+\infty} \int_{-\infty}^{+\infty} u_1^-(\xi, \eta) \left[ u_0^+(\xi, \eta) * F^{-1}\{e^{ik'_z d}\}\Big|_{x=\xi \& y=\eta} \right] d\xi d\eta \quad (2.22)$$

By substituting Eqn. 2.15,  $u_1^+(x, y) = u_0^+(x, y) * F^{-1}\{e^{ik'_z d}\}$ , Eqn. 2.22 can be simply expressed as shown below.

$$V(z) = \int_{-\infty}^{+\infty} \int_{-\infty}^{+\infty} u_1^-(\xi, \eta) u_1^+(\xi, \eta) d\xi d\eta \quad (2.23)$$

$$\text{Eqn. 2.14, } u_1^-(x, y) = -e^{i2k_w f_L (1+\bar{c}^2)} u_1^+(-x, -y) P_1(-x, -y) P_2(x, y) e^{-i\frac{k_w z}{f_L^2}(x^2+y^2)} R\left(\frac{x}{f_L}, \frac{y}{f_L}\right)$$

can be plugged into Eqn. 2.23 and the following equation can be found.

$$V(z) = \int_{-\infty}^{+\infty} \int_{-\infty}^{+\infty} u_1^+(-x, -y) u_1^+(x, y) P_1(-x, -y) P_2(x, y) R\left(\frac{x}{f_L}, \frac{y}{f_L}\right) e^{-i\frac{k_w z}{f_L^2}(x^2+y^2)} dx dy \quad (2.24)$$

Equation 2.24 is the V(z) curve equation in rectangular coordinates. Since the case is symmetric about the z-axis, Eqn. 2.24 can be transformed into cylindrical coordinates. From circular symmetry, the following can be applied to Eqn. 2.24

$$\begin{aligned} u_1^+(x, y) &= u_1^+(r), \\ P(x, y) &= P(r), \\ R\left(\frac{k_x}{k_w}, \frac{k_y}{k_w}\right) &= R\left(\frac{k_r}{k_w}\right) \end{aligned} \quad (2.25)$$

Where  $k_r = \sqrt{k_x^2 + k_y^2}$ ,  $r = \sqrt{x^2 + y^2}$ , and  $r = 0 \sim R_t$  as the radial distance on the transducer.  $R_t$  is the radius of the transducer in Fig. 2-8. Therefore, the  $V(z)$  curve equation can be expressed as below in cylindrical coordinates.

$$V(z) = \int_0^\infty u_1^+(r)^2 P(r)^2 R\left(\frac{r}{f_L}\right) e^{-i\frac{k_w z}{f_L^2}(r^2)} r dr \quad (2.26)$$

Note that a factor of  $2\pi$  is disregarded and  $P_1(r)$  and  $P_2(r)$  are simply multiplied since in most cases  $P_1(r) = P_2(r)$ . Again,  $f_L$  is not frequency.  $f_L$  is the focal length in Fig. 2-8 in this discussion.

Furthermore, Eqn. 2.26 can be expressed in terms of the incident angles ( $\theta_i$ ) of wave fronts. The transducer has its maximum output voltage when  $z=0$  and which is stated below.

$$V(z=0) = \int_0^\infty u_1^+(\theta_i)^2 P(\theta_i)^2 R(\theta_i) r dr \quad (2.27)$$

The following relations can be applied to Eqn. 2.27

$$r = f_L \sin \theta_i, \quad dr = f_L \cos \theta_i d\theta_i, \quad (2.28)$$

Then, Eqn. 2.27 can be re-expressed as shown below.

$$V(z=0) = f_L \int_0^{\theta_{ap}/2} u_1^+(\theta_i)^2 P(\theta_i)^2 R(\theta_i) \sin \theta_i \cos \theta_i d\theta_i \quad (2.29)$$

Here  $\theta_{ap}$  is the aperture angle of the acoustic lens. When the ultrasonic beam is defocused toward the specimen by  $-z$  (Right in Fig. 2-9) then the phase of the wave will be changed by  $2k_w z \cos \theta_i$ . Therefore, the  $V(z)$  equation can be written as shown below. Figure 2-9 graphically shows both cases with geometries.

$$V(z) = f_L \int_0^{\theta_{ap}/2} u_1^+(\theta_i)^2 P(\theta_i)^2 R(\theta_i) \sin \theta_i \cos \theta_i e^{-i2k_w z \cos \theta_i} d\theta_i \quad (2.30)$$

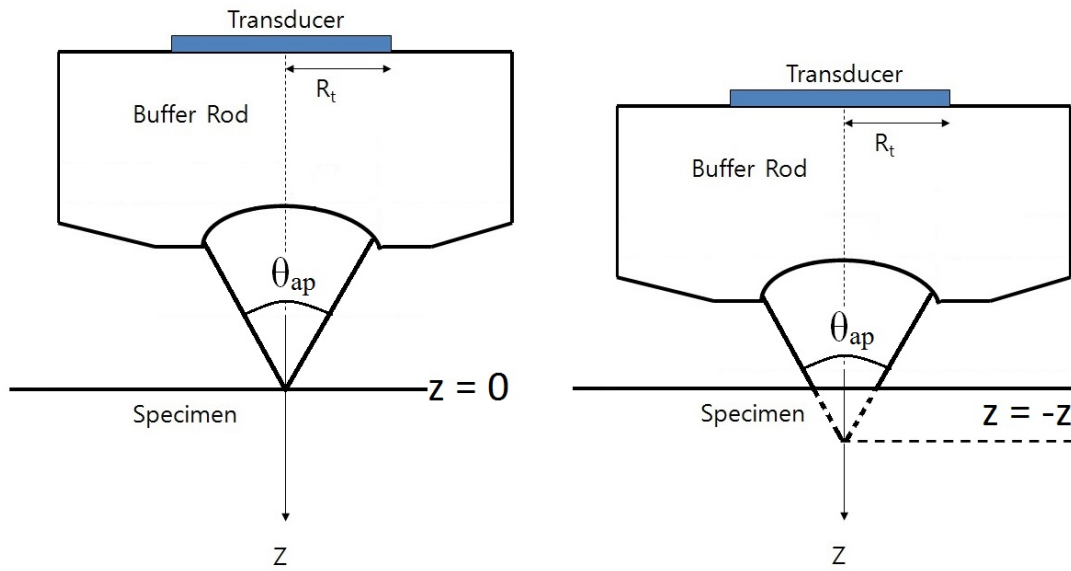


Figure 2-9. Geometries when the ultrasonic beam is focused on the surface of the specimen (Left) and when it is defocused toward the specimen (Right).

Now, the physical meaning of each term in the  $V(z)$  equation needs to be explored. First,  $u_1^+$  is the acoustic field on the back focal plane (plane 1), and it can be found from the specifications of the transducer. Second,  $P$  is the pupil function which can be determined by the geometry of the acoustic lens. Third,  $R$  is the reflectance function and it depends on the acoustic-elastic properties of the specimen. Lastly, the exponential is the defocusing factor which is decided by the geometry of the acoustic lens and mechanical system.

Table 2-1. Terms in the  $V(z)$  equation and their physical meanings and dependence.

Terms in the $V(z)$ Equation	Physical Meaning	Depends on
$u_1^+$	Acoustic field on back focal plane	Transducer's specification
$P$	Pupil function	Lens geometry
$R$	Reflectance function	Material's acoustic elastic properties
$e^{2k_w z \cos \theta_l}$	Defocusing factor	Lens geometry and mechanical system

Table 2-1 shows the terms, their physical meaning, and what they depend on. Among the four terms, only the reflectance function is determined by the acoustic elastic properties of the materials while the others can be found from the system specifications. That is, if the reflectance function can be calculated then the  $V(z)$  equation can be formulated and  $V(z)$  curve can be simulated. Thus, the next step will be finding the reflectance function, particularly in multilayered solids.

### 2.3 Reflectance Function in Multilayered Solids

The reflectance function plays a key role in simulating the  $V(z)$  curve. In this study, multilayered cases are considered and the following model is implemented in the  $V(z)$  curve simulation program. The model for the reflectance function in multilayered solids was proposed by T. Kundu [36] and can be also found in Z. Yu's paper [40]. In the model, the Thomson-Haskell transfer matrix method is used for the calculation. Figure 2-10 is the geometry to model the reflectance function.

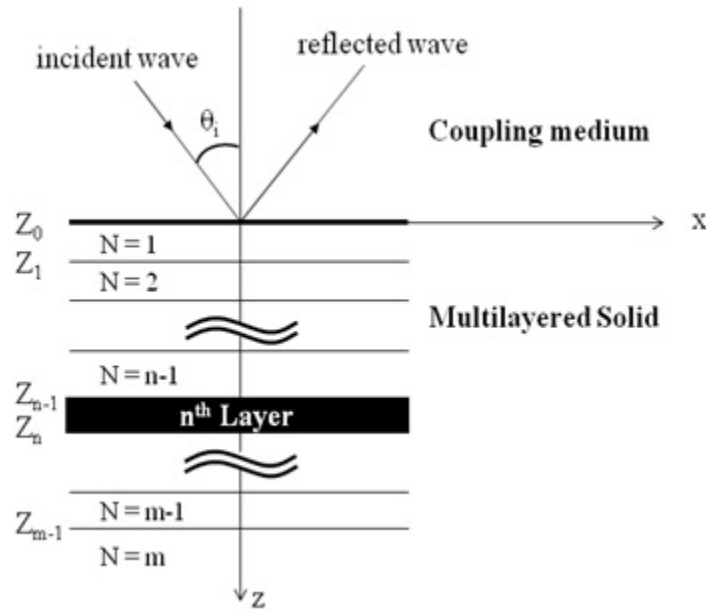


Figure 2-10. Geometry of incident wave from coupling medium to the multilayered solid to model the reflectance function,  $R(\theta)$ .

In Fig. 2-10 each layer is assumed as isotropic, homogeneous, and elastic and these layers are indexed as  $N$ . At the top layer,  $N=1$  and for  $n^{\text{th}}$  layer  $N=n$ . In the  $n^{\text{th}}$  layer, the density is  $\rho_n$ , the longitudinal wave velocity is  $\alpha_n$ , and the shear wave velocity is  $\beta_n$ . Each plane is denoted as  $Z_{N-1}$ , so the plane at the boundary between the coupling medium and the solid is  $Z=Z_0$ . The longitudinal wave velocity, wave number, and density in the coupling medium are noted as  $V_w$ ,  $k_w$ ,



and  $\rho$  respectively. A plane wave with amplitude of 1 is incident on the coupling medium-solid interface with incident angle,  $\theta_i$ . The total reflected field back into the coupling medium is our interest in the calculation.

The modeling approach can be explained in three steps. First, an interface condition between top and bottom plane ( $Z_{n-1}$  &  $Z_n$  in Fig. 2-10) of  $n^{\text{th}}$  layer is defined. Then, the interface condition found will be applied through on the layers and a relationship between the top surface ( $Z_0$  plane in Fig. 2-10) and the bottom layer ( $m^{\text{th}}$  layer) will be determined. Finally, boundary and interface conditions will be applied to the model and the reflectance function will be calculated from the equation which relates the top surface and the bottom layer.

First, the  $n^{\text{th}}$  layer longitudinal and shear wave potentials, given by  $\phi_n$  and  $\psi_n$  satisfying the wave equations, can be represented as shown below.

$$\begin{aligned}\phi_n &= [a_n e^{-i\eta_{\alpha n}(z_n - z_{n-1})} + b_n e^{i\eta_{\alpha n}(z_n - z_{n-1})}] e^{i(k_{nx}x - \omega t)} \\ \psi_n &= [c_n e^{-i\eta_{\beta n}(z_n - z_{n-1})} + d_n e^{i\eta_{\beta n}(z_n - z_{n-1})}] e^{i(k_{nx}x - \omega t)}\end{aligned}\quad (2.31)$$

$\omega$  is the angular frequency and the z component of longitudinal and shear wave vectors are  $\eta_{\alpha n}$  and  $\eta_{\beta n}$  respectively as given below.

$$\eta_{\alpha n}^2 = k_{\alpha n}^2 - k_x^2, \quad \eta_{\beta n}^2 = k_{\beta n}^2 - k_x^2 \quad (2.32)$$

$k_x$  is the x-component of the wave number and expressed as

$$k_x = k_w \sin \theta_i = k_{\alpha n} \sin \theta_n = k_{\beta n} \sin \gamma_n \quad (2.33a)$$

$$k_w = \omega / V_w, \quad k_{\alpha n} = \omega / \alpha_n, \quad \text{and} \quad k_{\beta n} = \omega / \beta_n. \quad (2.33b)$$

The unknown constants,  $a_n$ ,  $b_n$ ,  $c_n$ , and  $d_n$  will be designated as below.

$$\{C_n\} = \{c_n \quad a_n \quad b_n \quad d_n\}^T \quad (2.34)$$

$\{C_n\}$  will be called an unknown constant vector which will be found from the interface and boundary conditions later. Now, the displacement and stress vectors in the  $n^{\text{th}}$  layer will be defined.  $u_n$  and  $v_n$  for tangential and normal components of displacement vectors and  $\sigma_n$  and  $\tau_n$  for tangential and normal components of stress vectors will be assigned as shown below.

$$\{S_n\} = \{u_n \quad v_n \quad \sigma_n \quad \tau_n\}^T \quad (2.35)$$

$\{S_n\}$  will be denoted as the displacement and stress vector. Note that in the following equations  $e^{i(k_x x - \omega t)}$  will be omitted for simplicity. The two vectors,  $\{S_n\}$  and  $\{C_n\}$ , can be related as given.

$$\{S_n\} = [Q(n)][E(z - \zeta)]\{C_n\} \quad (2.36a)$$

or

$$\begin{Bmatrix} u_n \\ v_n \\ \sigma_n \\ \tau_n \end{Bmatrix} = [Q(n)][E(z - \zeta)] \begin{Bmatrix} c_n \\ a_n \\ b_n \\ d_n \end{Bmatrix} \quad (2.36b)$$

Where  $\zeta$  can be an arbitrary constant less than the thickness of the  $n^{\text{th}}$  layer.  $[Q(n)]$  and  $[E(z)]$  are given below.

$$[E(z)] = \begin{pmatrix} e^{-i\eta_{\beta n} z} & 0 & 0 & 0 \\ 0 & e^{-i\eta_{\alpha n} z} & 0 & 0 \\ 0 & 0 & e^{i\eta_{\alpha n} z} & 0 \\ 0 & 0 & 0 & e^{i\eta_{\beta n} z} \end{pmatrix} \quad (2.37)$$

$$[Q(n)] = \begin{bmatrix} i\eta_{\beta n} & ik_x & ik_x & -i\eta_{\beta n} \\ ik_x & -i\eta_{\alpha n} & i\eta_{\alpha n} & ik_x \\ 2\mu_n\eta_{\beta n}k_x & \mu_n(2k_x^2 - k_{\beta n}^2) & \mu_n(2k_x^2 - k_{\beta n}^2) & -2\mu_n\eta_{\beta n}k_x \\ -\mu_n(2k_x^2 - k_{\beta n}^2) & 2\mu_n\eta_{\alpha n}k_x & -2\mu_n\eta_{\alpha n}k_x & -\mu_n(2k_x^2 - k_{\beta n}^2) \end{bmatrix} \quad (2.38)$$

$\mu_n$  is the shear modulus or Lamé's 2<sup>nd</sup> parameter in the n<sup>th</sup> layer. Equation 2.36a can be expressed in terms of the  $Z_{n-1}$  and  $Z_n$  planes for the n<sup>th</sup> layer as below.

$$\{S_n(z_n)\} = [Q(n)][E(z - z_{n-1})]\{C_n\} \quad (2.39)$$

A plane can be expressed not only as a top plane of a layer but also as a bottom plane of the upper layer. For example, a plane,  $Z_{n-1}$  in Fig. 2-10, can be denoted as a top plane of n<sup>th</sup> layer and also as a bottom plane of n-1<sup>th</sup> layer as

$$\{S_n(z_{n-1})\} = \{S_{n-1}(z_{n-1})\} \quad (2.40a)$$

Equation 2.40a can be expanded

$$\begin{aligned} \{S_n(z_{n-1})\} &= \{S_{n-1}(z_{n-1})\} \\ &= [Q(n)][E(z_{n-1} - z_{n-1})]\{C_n\} \\ &= [Q(n)]\{C_n\} \end{aligned} \quad (2.40b)$$

Since  $[Q(n)]$  can be inverted,  $\{C_n\}$ , the unknown constant vector in n<sup>th</sup> layer, can be found as shown below.

$$\{C_n\} = [Q(n)]^{-1}\{S_{n-1}(z_{n-1})\} \quad (2.41)$$

By substituting Eqn. 2.41 into Eqn. 2.39 a relation between the displacement & stress vector of top and bottom plane of n<sup>th</sup> layer can be determined.

$$\{S_n(z_n)\} = [Q(n)][E(z_n - z_{n-1})][Q(n)]^{-1}\{S_{n-1}(z_{n-1})\} \quad (2.42)$$

The Thomson-Haskell layer matrix,  $[P(n)]$  replaces  $[Q(n)][E(z_n - z_{n-1})][Q(n)]^{-1}$  and Eqn. 2.42 is expressed below.

$$\{S_n(z_n)\} = [P(n)]\{S_{n-1}(z_{n-1})\} \quad (2.43)$$

The first step, finding an interface condition between the top and bottom planes ( $Z_{n-1}$  &  $Z_n$  in Fig. 2-10) of the  $n^{\text{th}}$  layer has been completed.

The second step is to define a relation between the top surface ( $Z_0$  in Fig. 2-10) and the bottom layer ( $m^{\text{th}}$  layer in Fig. 2-10). By recursively applying the  $[P(n)]$  equation, a relation between the displacement and stress vector of the top surface,  $\{S_0\}$ , and that of the top-plane of the bottom layer,  $\{S_{m-1}(z_{m-1})\}$  can be obtained as shown below.

$$\{S_{m-1}(z_{m-1})\} = [P(m-1)][P(m-2)]\dots[P(n)]\dots[P(1)]\{S_0\} \quad (2.44)$$

By applying Eqn. 2.40,  $\{C_n\} = [Q(n)]^{-1}\{S_{n-1}(z_{n-1})\}$  to the bottom layer, the unknown constant vector in the layer can be found as shown below.

$$\{C_m\} = [Q(m)]^{-1}\{S_{m-1}(z_{m-1})\} \quad (2.45)$$

By substituting Eqn. 2.44 into Eqn. 2.45 and expanding it, a relation between the displacement and stress vector of the top surface,  $\{S_0\}$ , and an unknown constant vector in the bottom layer,  $\{C_m\}$ , is acquired as shown below.

$$\begin{aligned} \{C_m\} = & [Q(m)]^{-1}[P(m-1)][P(m-2)]\dots \\ & \dots[P(n+1)][P(n)][P(n-1)]\dots[P(1)]\{S_0\} \end{aligned} \quad (2.46)$$

$[J(m,1)]$  is introduced to replace the matrix multiplications and Eqn. 2.46 is rewritten as

$$\{C_m\} = [J(m,1)]\{S_0\} \quad (2.47)$$

Note that the  $[J(m,1)]$  does not represent a Jacobian matrix but simply replaces the multiplication of the matrixes. It is a 4 by 4 matrix since  $\{C_m\}$  and  $\{S_0\}$  are 4 by 1 matrixes.

As the next step,  $\{C_m\}$  and  $\{S_0\}$  will be determined from interface and boundary conditions. In the coupling medium, there is no shear wave since it is a liquid. So longitudinal and shear wave potentials can be written as below.

$$\begin{aligned}\phi &= Re^{-i\eta z} + 1e^{i\eta z} \\ \psi &= 0\end{aligned}\tag{2.48}$$

Since it is assumed that a plane wave with amplitude of one is incident on the coupling medium-solid interface, the amplitude  $R$  in Eqn. 2.48 becomes the reflectance function of what is being sought through this section. From Eqn. 2.48 an unknown constant vector on the interface is expressed as shown below.

$$\{C_0\} = \{0 \quad 1 \quad R \quad 0\}^T\tag{2.49}$$

On the liquid-solid interface, a normal component of the stress vector,  $\tau_0$ , is zero ( $\tau_0 = 0$ ). Then,  $\{S_0\}$  can be written as

$$\{S_0\} = [u_0 \quad v_0 \quad \sigma_0 \quad \tau_0 = 0]^T\tag{2.50}$$

From Eqn. 2.36a,  $\{S_n\} = [Q(n)][E(z - \zeta)]\{C_n\}$  where  $\zeta = 0$ , Eqn. 2.50 can be expanded as

$$\{S_0\} = [u_0 \quad v_0 \quad \sigma_0 \quad \tau_0 = 0]^T = [Q(0)][E(z)]\{C_0\}\tag{2.51}$$

By applying another interface condition, which is the shear modulus,  $\mu_0 = 0$  in the  $[Q(0)]$  in Eqn. 2.38 on the interface and by substituting Eqn. 2.49 into Eqn. 2.51, the displacement and stress vector on the interface  $\{S_0\}$  is obtained as shown below.

$$\{S_0\} = \begin{bmatrix} u_0 & i\eta(1-R) & -\rho V_w^2 k_w^2(1+R) & 0 \end{bmatrix}\tag{2.52}$$

In the bottom ( $m^{\text{th}}$ ) layer, it can be assumed that there are only downward travelling waves. Then, longitudinal and shear wave potentials in the layer can be written as shown below.

$$\begin{aligned}\phi_m &= 0e^{-i\eta_{\alpha m} z} + b_m e^{i\eta_{\alpha m} z} \\ \psi_m &= 0e^{-i\eta_{\beta m} z} + d_m e^{i\eta_{\beta m} z}\end{aligned}\quad (2.53)$$

Then, from Eqn. 2.53 an unknown constant vector in the bottom layer,  $\{C_m\}$ , can be found as shown below.

$$\{C_m\} = [0 \quad 0 \quad b \quad d]^T \quad (2.54)$$

The displacement and stress vector on the interface,  $\{S_0\}$ , and an unknown constant vector in the bottom layer,  $\{C_m\}$ , are found in Eqn. 2.52 and Eqn. 2.54. They are related to each other as Eqn. 2.47,  $\{C_m\} = [J(m,1)]\{S_0\}$ , and as shown below.

$$\begin{Bmatrix} 0 \\ 0 \\ b_m \\ d_m \end{Bmatrix} = [J(m,1)] \begin{Bmatrix} u_0 \\ i\eta(1-R) \\ -\rho V_w^2 k_w^2 (1+R) \\ 0 \end{Bmatrix} \quad (2.55)$$

By solving Eqn. 2.55 for  $R$  with eliminating  $u_0$ , the reflectance function in multilayered solids is finally discovered as shown below.

$$R = \frac{\eta(J_{11}J_{22} - J_{12}J_{21}) + i\rho V_w^2 k_w^2 (J_{11}J_{23} - J_{21}J_{13})}{\eta(J_{11}J_{22} - J_{12}J_{21}) - i\rho V_w^2 k_w^2 (J_{11}J_{23} - J_{21}J_{13})} \quad (2.56)$$

Here  $J_{ij}$  is the  $(i,j)$  element of the matrix  $[J]$ .

## Chapter 3

### Simulation Software

Based on the theory and the equations introduced in the previous chapter, a  $V(z)$  curve simulation software system was developed. The  $V(z)$  simulation software was coded with Matlab 2011b and all input and output interfaces were incorporated in a graphical user interface (GUI) for users' convenience. The  $V(z)$  simulation software is organized into two main parts – simulation of a  $V(z)$  curve and calculation of surface acoustic wave velocity. In this chapter, the  $V(z)$  simulation software is described by its execution sequence with corresponding screen shots of the two main parts. Details about the scripts and functions of the software can be found in Appendix A.

Figure 3-1 shows the initial view of the executed  $V(z)$  simulation software. It has four sub-figures which display acoustic fields on the four planes in Fig. 2-8 in the outgoing direction, and the incoming direction, the amplitude and phase of the reflectance function, and a  $V(z)$  curve, respectively from the left to the right.

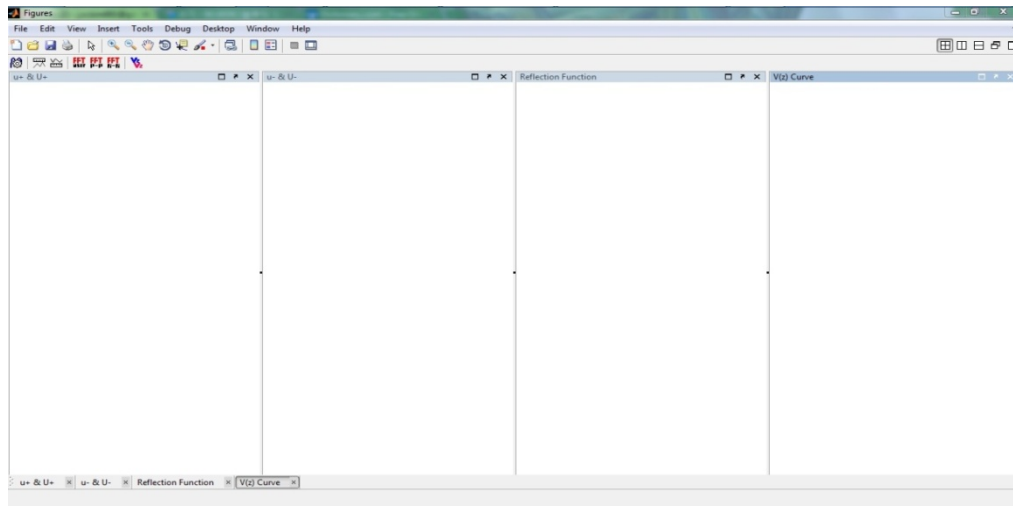



Figure 3-1. Initial view of the  $V(z)$  simulation software.

### 3.1 Simulation of a $V(z)$ Curve

#### 3.1.1 Simulation Setup

Prior to running a  $V(z)$  curve simulation, one needs to set simulation parameters. The  icon opens the ‘Simulation Setup’ window. Figure 3-2 shows the setup window (Right) and input parameters (Left).

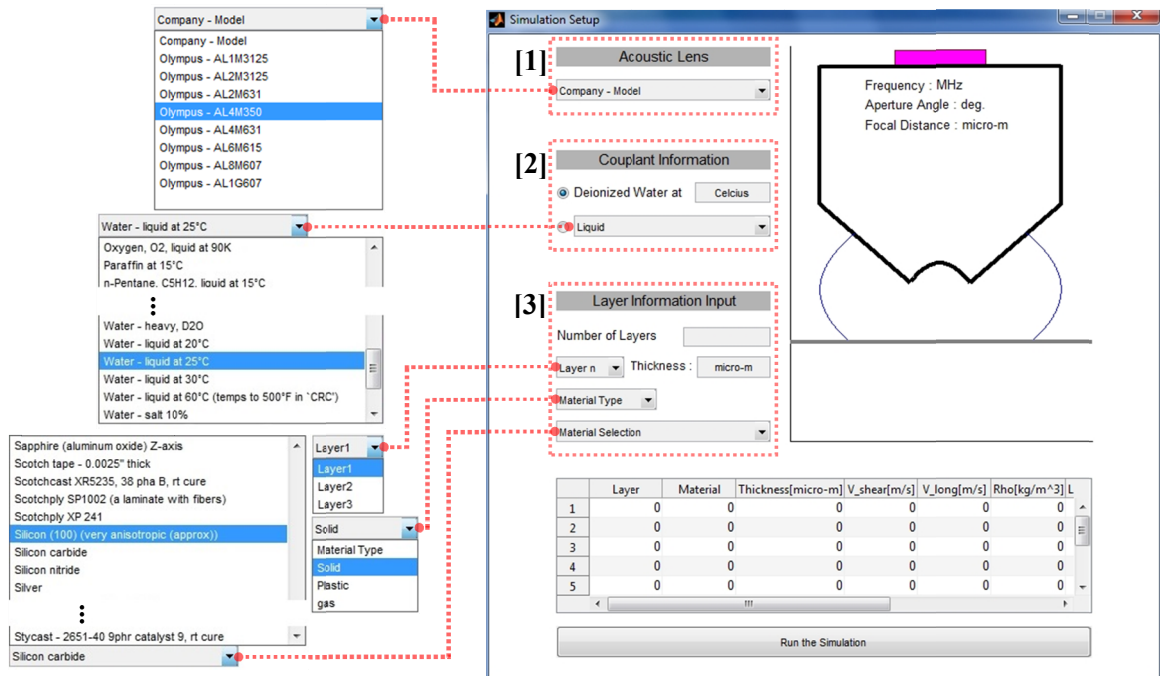


Figure 3-2. Initial view of ‘Simulation Setup’ window (Right) and drop-down lists (Left).

First, the software takes a selection of an acoustic lens, [1] in Fig. 3-2. Specifications of the listed acoustic lenses are described in Appendix B. Additional lenses and their specifications can simply be added into the ‘AcousticLens\_ParameterList.xlsx’ file located in the same directory with the  $V(z)$  simulation software and the  $V(z)$  simulation software automatically updates its acoustic lens list.



Second, information about the coupling medium is requested, [2] in Fig. 3-2. A user can choose either de-ionized water with temperature in Celsius or a substance from the liquid list. When a user selects de-ionized water and enters its temperature, then the temperature equation, Eqn. 3.1, is applied to calculate the velocity of sound wave in the water ( $V_w$ ).

$$V_w = 1402.736 + 5.03358t - 0.0579506t^2 + 3.31636 \times 10^{-4}t^3 - 1.45262 \times 10^{-6}t^4 + 3.0449 \times 10^{-9}t^5 \quad (3.1)$$

Then, the focal length ( $f_L$ ) of the selected acoustic lens in the given de-ionized water is found by Eqn. 3.2.

$$f_L = \frac{R_C}{\left(1 - \frac{V_w}{V_{Lens}}\right)} \quad (3.2)$$

$R_C$  is the curvature radius of the lens and  $V_{Lens}$  is the velocity of sound waves in the acoustic lens, which is given in the lens specification.

Third, information for the layer/layers is required, [3] in Fig. 3-2. Here, a user inputs the number of layers of the specimen and chooses a layer from the 'Layer n' drop-down list. Then, the user specifies the thickness in  $\mu\text{m}$ , material type, and a material of the selected layer on the 'Thickness' input box, from the 'Material Type' drop-down list, and from the 'Material Selection' drop-down list, respectively. Note that 'Layer1' always represents the top layer and the bottom layer (substrate) is always denoted as 'Layer n' where n is the number of layers. In Fig. 3-3, for example, 'Layer1', 'Layer2', and 'Layer3' represent the platinum coating, titanium deposition, and silicon (100) substrate respectively.

The materials and material properties are saved in the 'MaterialProp.xlsx' file placed in the same directory with the V(z) simulation software. Additional materials can easily be added

into a proper tab (Solid, Plastic, or Gas) in the ‘MaterialProp.xlsx’ file, and the V(z) simulation software automatically updates the ‘Material Selection’ list with the newly entered materials.

Figure 3-3 shows the updated ‘Simulation Setup’ window after entering all the required parameters to simulate a V(z) curve for the given specimen. In Fig. 3-3, one can see that the information of the acoustic lens and coupling medium is displayed as well as layers of the specimen in the graphical view of the lens and the specimen. In the table on the bottom of the window, the elastic properties of the materials selected for the layers are displayed.

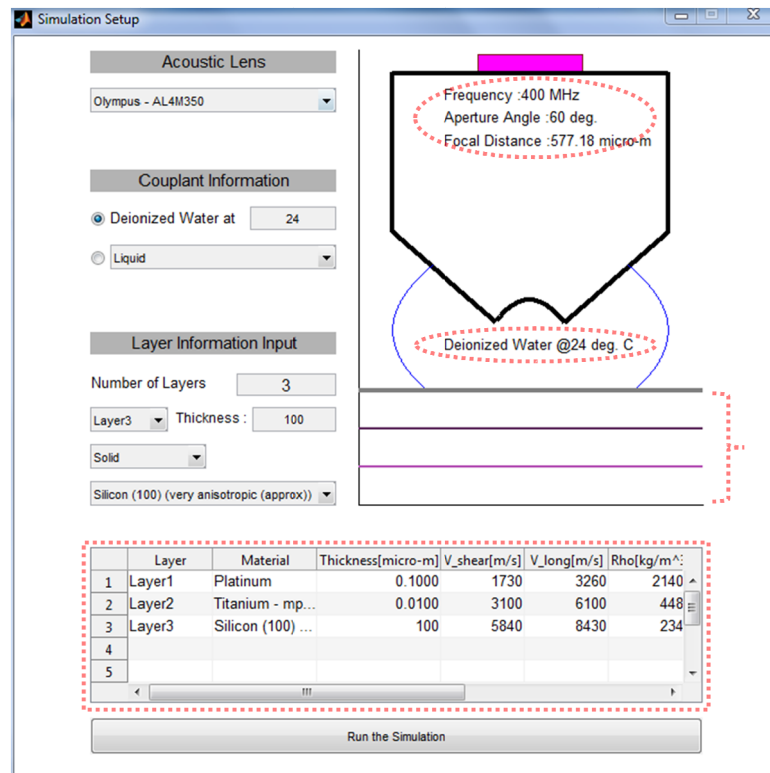


Figure 3-3. Updated view of the ‘Simulation Setup’ window.

Now, the V(z) curve simulation can be executed by clicking the ‘Run the Simulation’ button on the bottom of the interface.

### 3.1.2 Simulation Result

The simulated acoustic fields on the four planes in both outgoing and incoming directions, the reflectance function, and a  $V(z)$  curve are displayed as shown in Fig. 3-4.

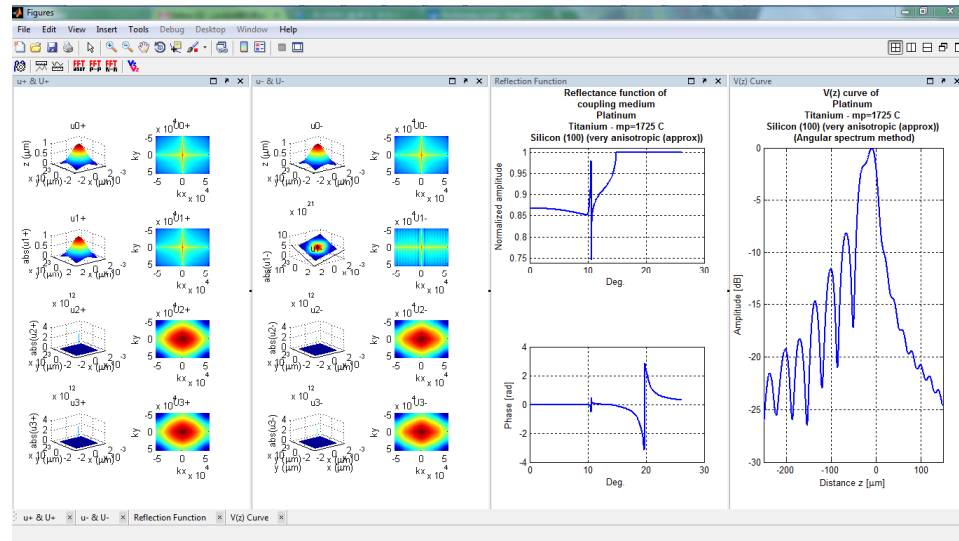



Figure 3-4. Simulation result. From the left to the right, acoustic fields in outgoing and incoming direction, amplitude and phase of the reflectance function, and a  $V(z)$  curve of the given model.

Each sub-figure can be maximized by clicking the  icon on the upper-right corner as shown in Fig. 3-5.

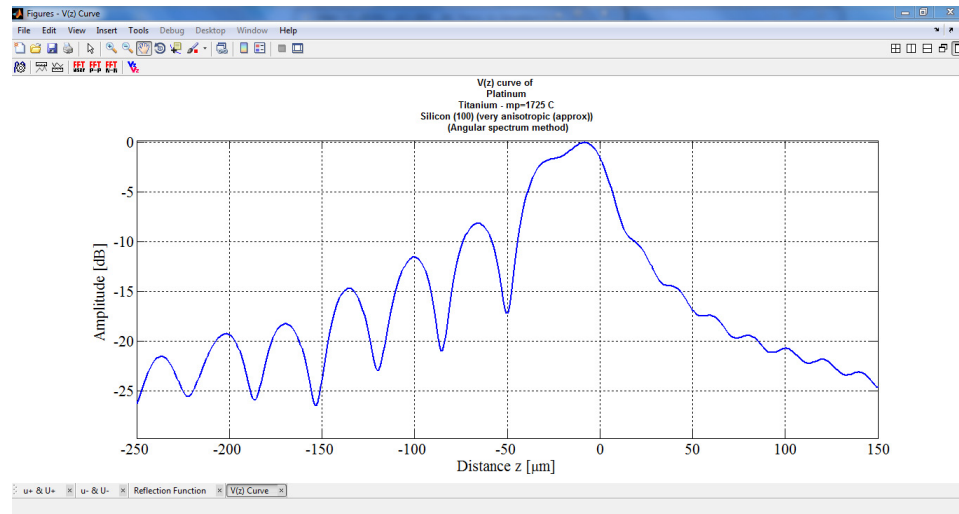


Figure 3-5. Maximized  $V(z)$  curve simulation figure.

### 3.2 Calculation of Surface Acoustic Wave Velocity

The next task, following the  $V(z)$  curve simulation, is to calculate the surface acoustic wave velocity from the  $V(z)$  curve. In this simulation software, signal processing techniques are applied to extract the surface acoustic wave component from a  $V(z)$  curve and to calculate the surface acoustic wave velocity from the extracted component rather than using Eqn. 2.1 [41]. This is due to the fact that the space between minima is not actually constant in both experimentally taken and simulated  $V(z)$  curves. In this section, calculating the surface acoustic wave velocity from  $V(z)$  curves by using signal processing techniques is explained step by step. Figure 3-6 shows the steps to calculate the surface acoustic wave velocity.

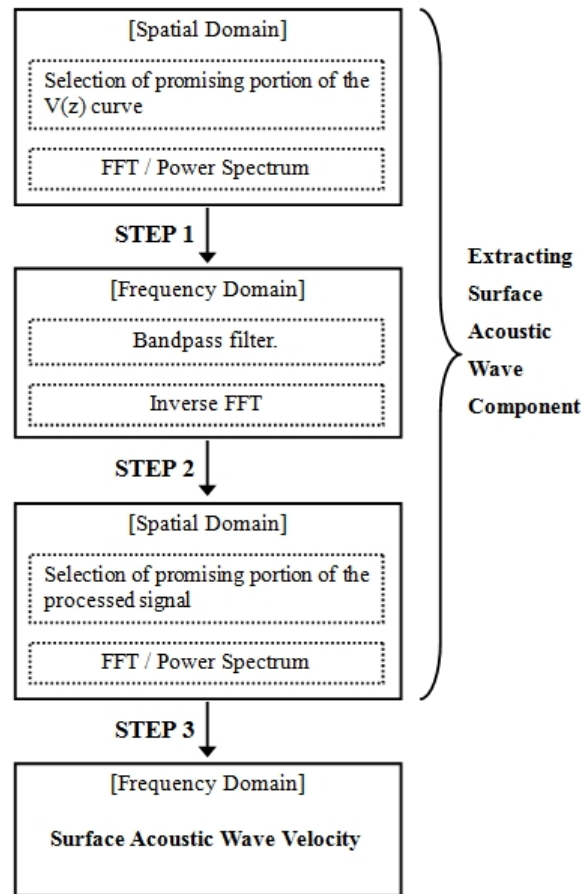









Figure 3-6. Steps to calculate the surface acoustic wave velocity from a simulated  $V(z)$  curve.

### 3.2.1 STEP 1. Spatial Domain to Frequency Domain

These    (FFT user, FFT P-P, FFT N-N) icons allow a user to choose a portion of a simulated  $V(z)$  curve and take a fast Fourier transform (FFT) of it.  (FFT user) can be used to select any part of a plot where a user wants to choose and take an FFT of it.  (FFT P-P) automatically finds the nearest peaks from where a user clicks to select from a peak to peak portion of a plot and take an FFT of it. Oppositely,  (FFT N-N) automatically finds the nearest minima from where a user clicks to select from a null to null (trough to trough) portion of a plot and take an FFT of it. In the following process,  (FFT N-N) is mostly used. The selected part for the FFT is displayed in red. Figure 3-7 shows a selected portion of a simulated  $V(z)$  curve for FFT.

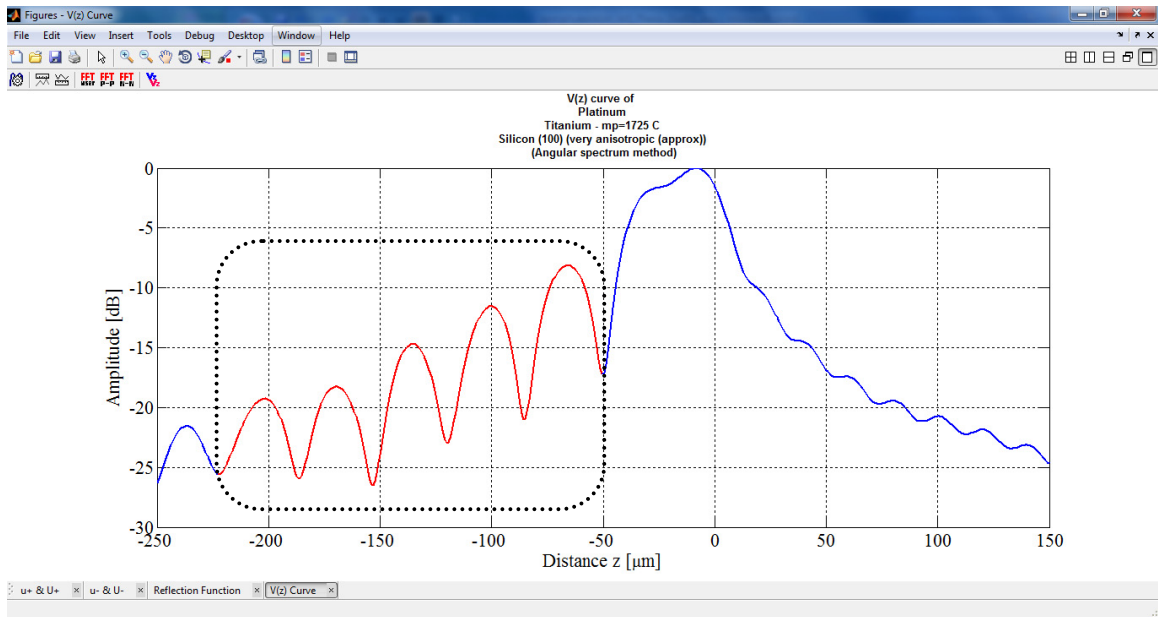


Figure 3-7. Selected portion (in the dotted box here, red in the software) of a simulated  $V(z)$  curve for FFT.

The  $V(z)$  curve simulation software processes the FFT of the selected signal and displays the power spectrum of it in an additional figure window. Figure 3-8 shows the power spectrum of the selected signal in Fig. 3-7.

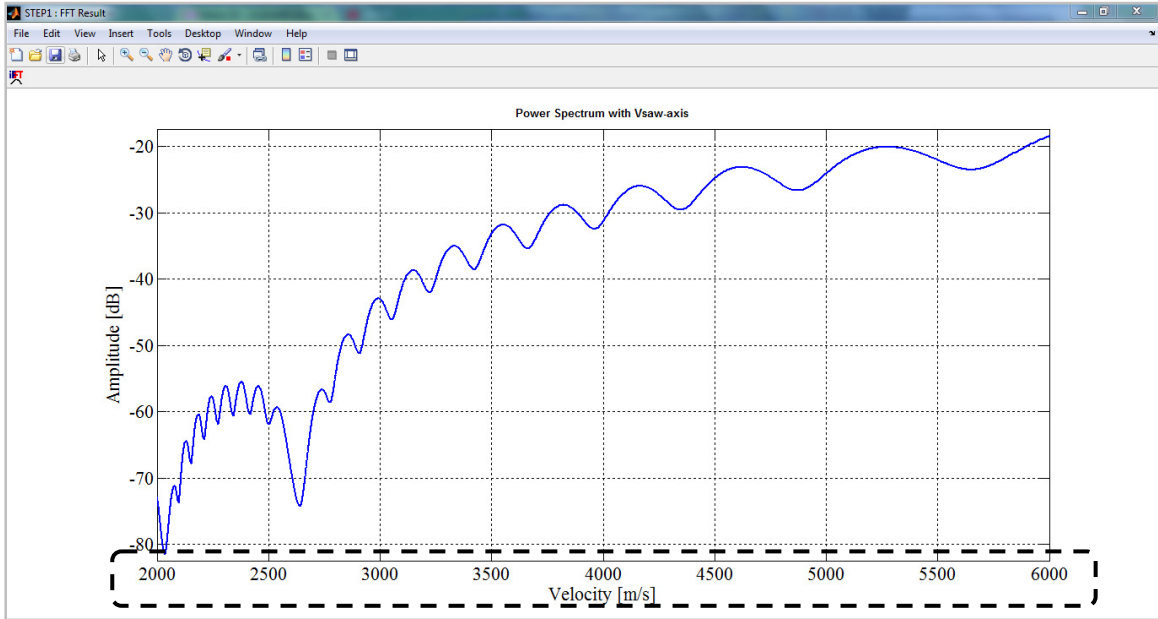


Figure 3-8. Power spectrum of the selected signal.

In Fig. 3-8, it can be noticed that the x-axis is velocity in m/s instead of frequency even though the processed signal is supposed to be in the frequency domain. Actually, the plot is in the frequency domain but the x-axis is converted from frequency to velocity. The conversion is an important part of the surface acoustic wave velocity calculation process and is explained in the next section.

### 3.2.2 Converting Frequency Axis to Velocity Axis

In this section, the frequency axis is conversion to velocity axis in the power spectrum plot is discussed before moving forward to ‘Step 2’.

The converting process can be explained from Eqn. 2.1b in Chapter 2.

$$V_{saw} \cong \sqrt{V_w \cdot f \cdot \Delta z} \quad (2.1b)$$

In Eqn. 2.1b, the acoustic wave velocity in the water ( $V_w$ ), and the operating frequency ( $f$ ) are known and  $\Delta z$  can be found from the following equation.


$$\Delta z = Dz / f_{ps} \quad (3.3)$$

$Dz$  is the total vertical movement distance of the acoustic lens for  $V(z)$  curve and  $f_{ps}$  is the frequency in the power spectrum plot.  $Dz$  for each acoustic lens can be found in Appendix B. Then, Eqn. 2.1b can be rewritten as shown below.

$$V_{saw} \cong \sqrt{V_w \cdot f \cdot Dz / f_{ps}} \quad (3.4)$$

Equation 3.4 converts the frequency values ( $f_{ps}$ ) to velocities in the x-axis of the power spectrum for the surface acoustic wave velocity calculation process since the velocity of a wave depends on its frequency.

### 3.2.3 STEP 2. Frequency Domain to Spatial Domain

Now the user has to choose the most promising lobe from the power spectrum and take an inverse FFT to extract the surface acoustic wave component. The selection of the lobe should be based on knowledge of the material's acoustic elastic properties and/or experimental data. In this example the substrate, silicon (100), dominates the propagation of acoustic waves and its surface acoustic wave velocity that was found from a series of experiments is 4762.32 m/s with the same setup as in Fig. 3-3. Thus, an appropriate choice could be similar to the choice in Fig. 3-9. The  (iFFT) icon can be used to make a selection. The software automatically finds the nearest minima from where a user clicks and selects a lobe. The chosen lobe is highlighted in red.

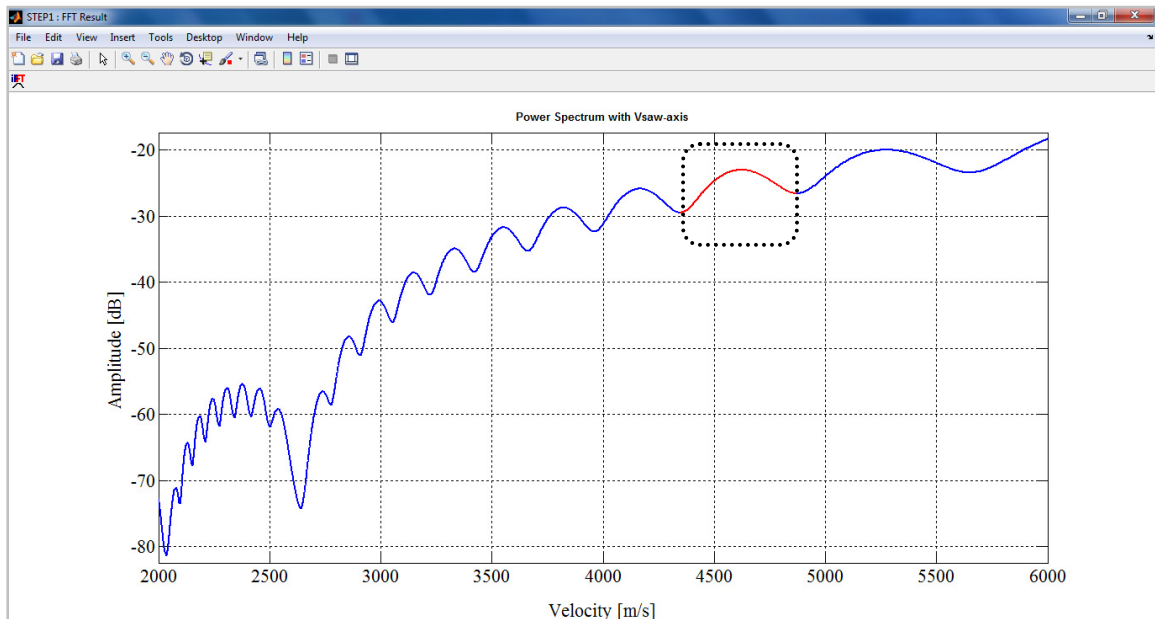


Figure 3-9. Selection of a lobe (in the dotted box here, red in the software) for an inverse FFT.

The software calculates the inverse FFT of the lobe and displays the result as in Fig. 3-10.

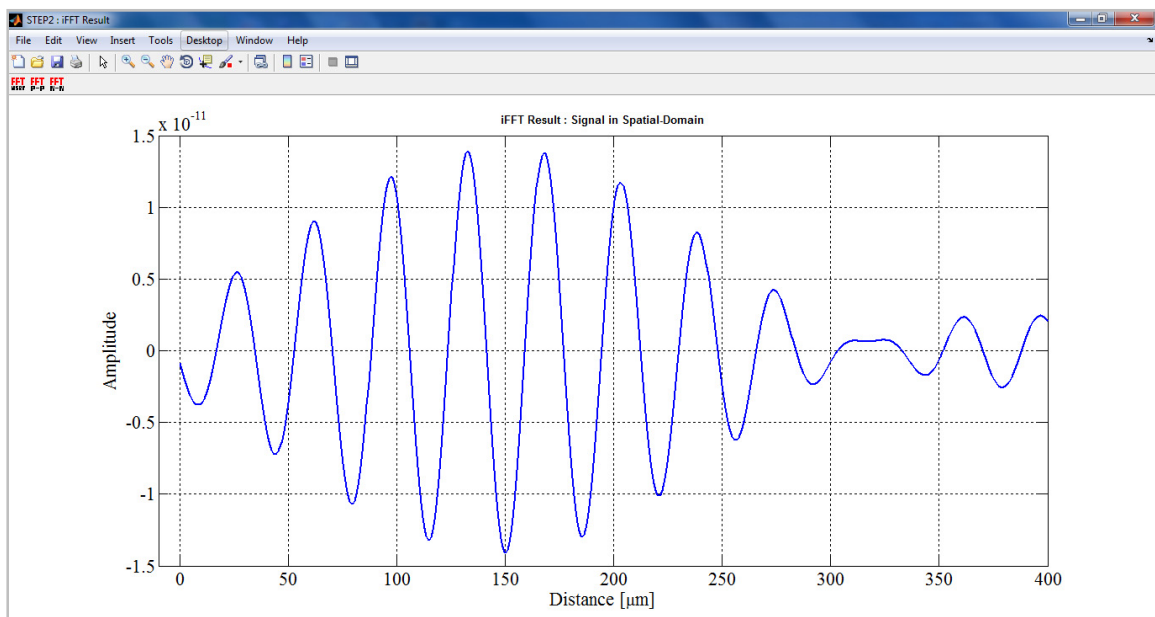






Figure 3-10. Inverse FFT of the selected lobe.



Now, the surface acoustic wave component is extracted as shown in Fig. 3-10 from the  $V(z)$  curve and only one more step is left to find the surface acoustic wave velocity.

### 3.2.4 STEP 3. Spatial Domain to Frequency Domain

The last step is almost the same as step 1. In this step selecting a proper portion of the signal is also critical. One useful tip is to make a symmetrical selection of the signal. Again the  (FFT user, FFT P-P, FFT N-N) icons can be used to make a selection.  (FFT user) and  (FFT P-P) act in the same way as they were described in section 3.2.1. The  (FFT N-N) icon finds the nearest zero crossing value, in other words, the minimum absolute value, from where a user clicks instead of finding minima. Figure 3-11 shows a symmetrical selection of the signal. The selected portion is highlighted in red.

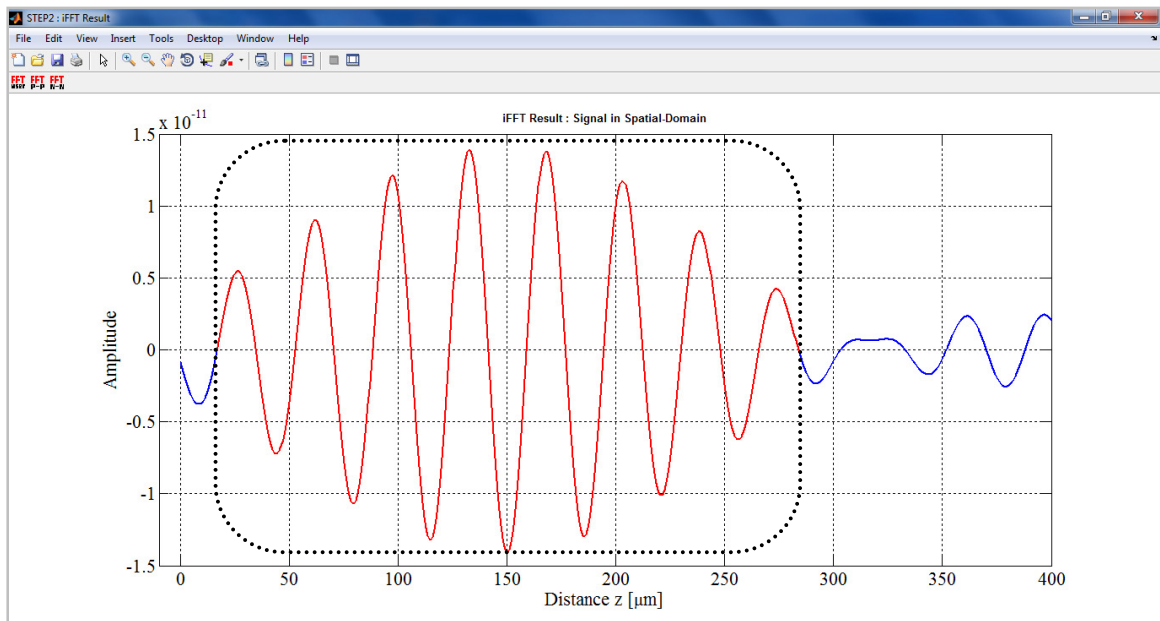


Figure 3-11. Selection of a portion (in the dotted box here, red in the software) of the signal for FFT.

The  $V(z)$  curve simulation software calculates an FFT of the selected signal and displays the result in a new figure window. Finally, the x-axis value for the highest peak of the calculated signal is the surface acoustic wave velocity found from the  $V(z)$  curve in Fig. 3-5. The simulation software automatically detects the peak and its x-axis value and displays it on the upper-right corner of the figure. Figure 3-12 shows the final result.

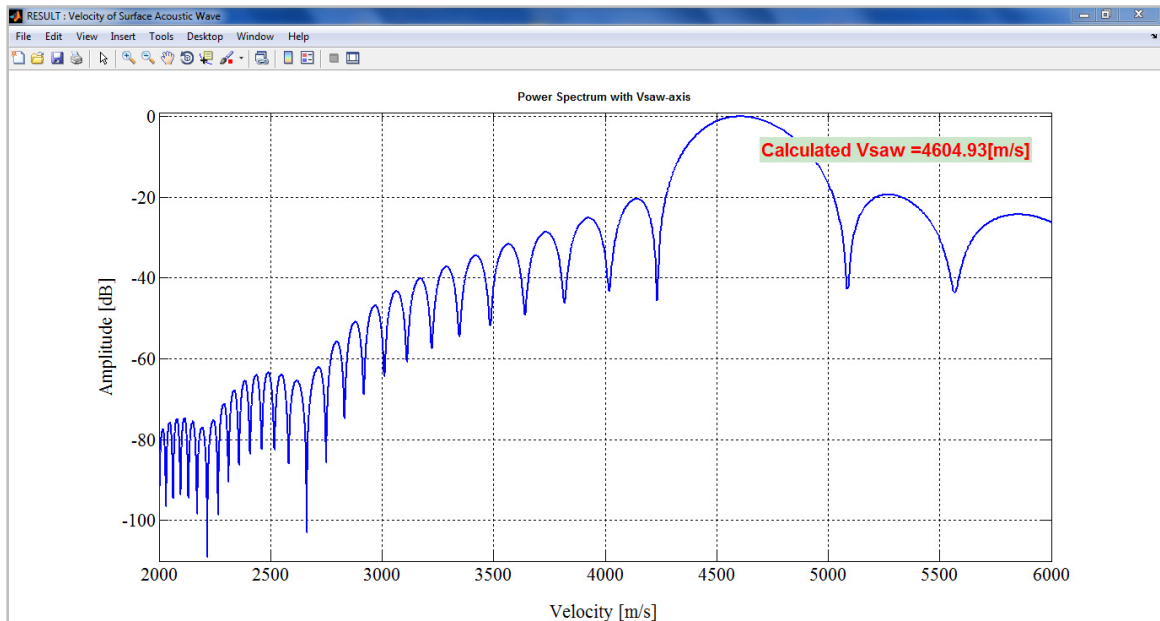




Figure 3-12. Surface acoustic wave velocity calculated from the  $V(z)$  curve in Fig. 3-5.

There are additional features, the icons  and , in the  $V(z)$  simulation software. They are added to measure space between peaks and minima, and to display two  $V(z)$  curves in one figure to compare each other, respectively. These features are discussed in Appendix C.

## Chapter 4

### Simulation and Experiment

To validate the simulation's reliability, a series of comparisons against experimental results and simulations of different models were carried out. First, the surface acoustic wave velocity calculated from simulation and from experiment in bulk silicon (100) were compared. Then, the simulation's thickness sensitivity was examined. Finally, the simulation and the experiments in a multilayered solid were inspected. Table 4-1 shows the elastic properties of the materials selected for the simulation and the experiment and the simulation and experimental parameters setup. In the table, longitudinal acoustic wave velocity and shear acoustic wave velocity in the material are respectively noted as  $V_L$  and  $V_S$ . Density is denoted as  $\rho$ .

Table 4-1. Elastic properties of selected materials and parameters for simulation and experiment

Elastic Properties of Selected Materials					Simulation and Experiment Parameters		
	Silicon (100)	Titanium	Platinum	Gold	Operation frequency		400 MHz
$V_L$ [m/s]	8430	6100	3260	3240	Acoustic lens	Aperture angle	60 deg.
$V_S$ [m/s]	5840	3100	1730	1200		Aperture diameter	500 $\mu\text{m}$
$\rho$ [kg/m <sup>3</sup> ]	2340	4480	21400	19700		Focal distance	577.50 $\mu\text{m}$
Thickness [ $\mu\text{m}$ ]	bulk	0.01	0.1	0.1	Operation temperature		24 °C

Please note that even though silicon is an anisotropic material, crystalline orientation of silicon (100) allows silicon (100) can be treated as an isotropic material, and a spherical acoustic

lens to be applicable to silicon (100). Crystalline orientation of silicon with the different Miller indices and directions of energy propagation are graphically described in Fig. 4-1 [55].

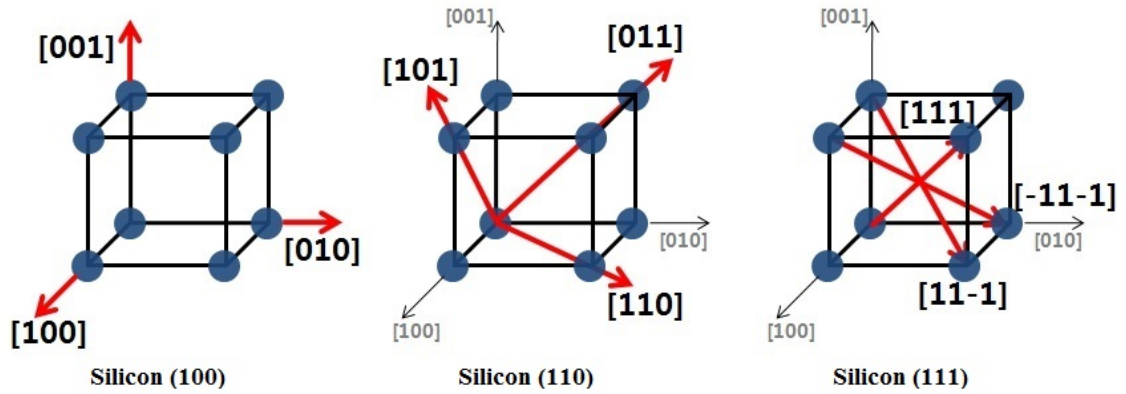


Figure 4-1. Crystalline orientation of different types of silicon

#### 4.1 Simulation vs. Experiment in bulk material (Silicon (100))

The first step was to verify the  $V(z)$  simulation software's reliability. The surface acoustic wave velocity calculated from a simulated  $V(z)$  curve was compared with that found from an experimentally taken  $V(z)$  curve for bulk silicon (100).

Note that for this simulation and experiment a different acoustic lens than what is stated in the Table 1 was used. The lens has the same 400 MHz operating frequency but with an aperture angle of 120 degrees, an aperture diameter of 866  $\mu\text{m}$ , and a 577.50  $\mu\text{m}$  focal length. Also, the operating temperature was 20  $^{\circ}\text{C}$ .

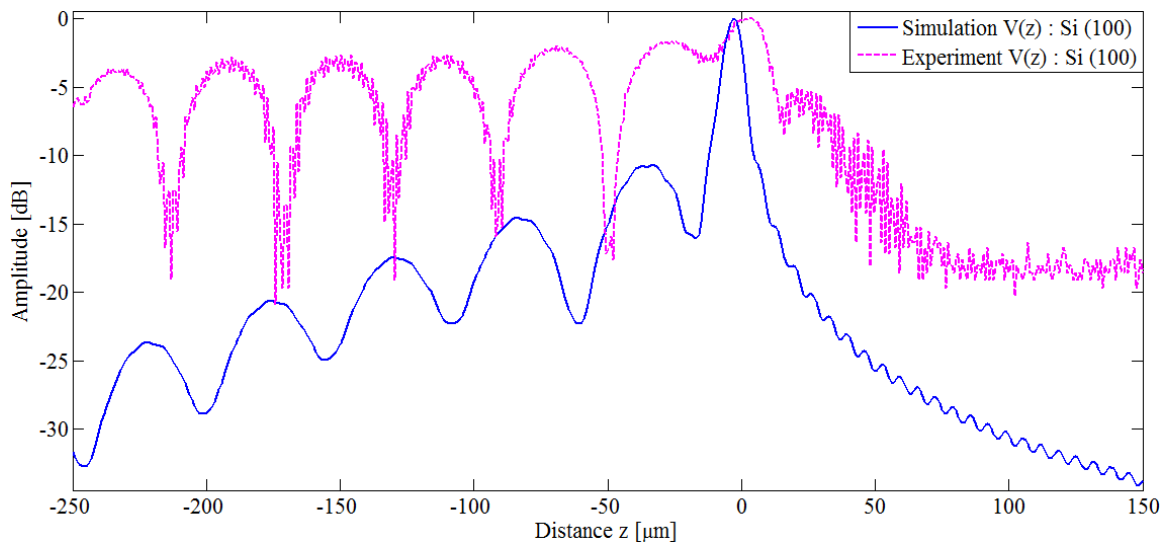


Figure 4-2. Two  $V(z)$  curves from a simulation and an experiment for silicon (100).

Figure 4-1 shows a simulated  $V(z)$  curve and an experimentally taken  $V(z)$  curve for silicon (100). Even though the two plots do not exactly look alike, especially in amplitude, it is just due to a simplification of the pupil function and the difference in amplitude does not affect the accuracy of surface acoustic wave velocity calculation. It is because what matters in the

calculation of surface acoustic wave velocity is space between peaks of nulls ( $\Delta z$ ) not amplitude.

The simplified pupil function applied in the V(z) simulation software is shown below.

$$P_1(x, y) = \text{circ} \left\{ \frac{\sqrt{x^2 + y^2}}{R_{ap}} \right\} \quad (4.1)$$

$$\text{circ} \left( \frac{\sqrt{x^2 + y^2}}{R_{ap}} \right) = 1, \text{ if } \frac{\sqrt{x^2 + y^2}}{R_{ap}} < 1 \quad (4.2)$$

$$\text{circ} \left( \frac{\sqrt{x^2 + y^2}}{R_{ap}} \right) = 0, \text{ if } \frac{\sqrt{x^2 + y^2}}{R_{ap}} > 1 \quad (4.3)$$

Methods to find more precise pupil function are described in Chapter 5.

Table 4-2. Surface acoustic wave velocity of silicon (100)

Surface acoustic wave velocity	
Calculation from the simulated V(z)	4921.70 [m/s]
Calculation from the experimental V(z)	4929.56 [m/s]

Table 4-2 presents the surface acoustic wave velocities calculated from the two V(z) curves. As it can be noticed in Table 4-2, that the two calculations agree each other very well and the discrepancy is small enough to be neglected. The difference could be from the approximation of material properties used in the simulation program and discretization of the signals since signal processing techniques are applied to calculate the surface acoustic wave velocities.

## 4.2 Thickness Sensitivity of Simulation

Sensitivity to thickness is extremely important especially when it comes to evaluating and/or diagnosing multilayer structured thin film systems. In this case, thickness sensitivity was examined. The following four models were simulated and compared to each other in two divided groups as shown in Fig. 4-2.

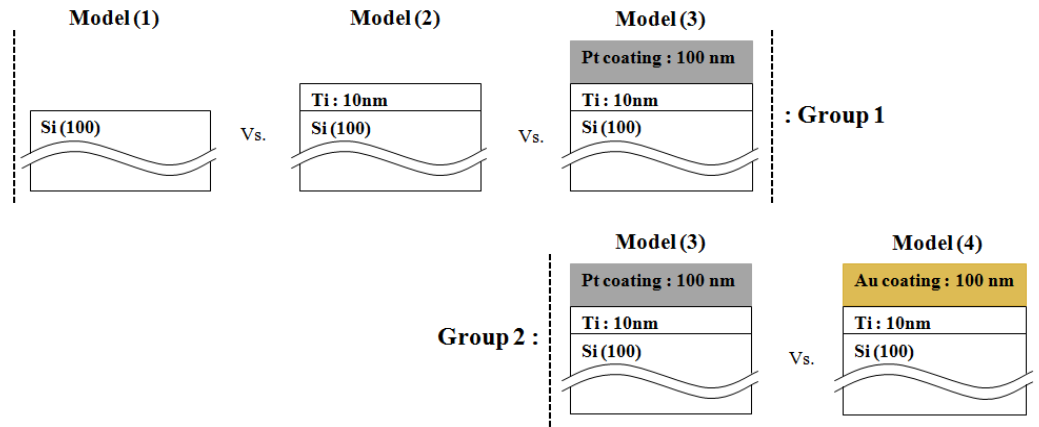


Figure 4-3. Simulation models to examine the thickness sensitivity

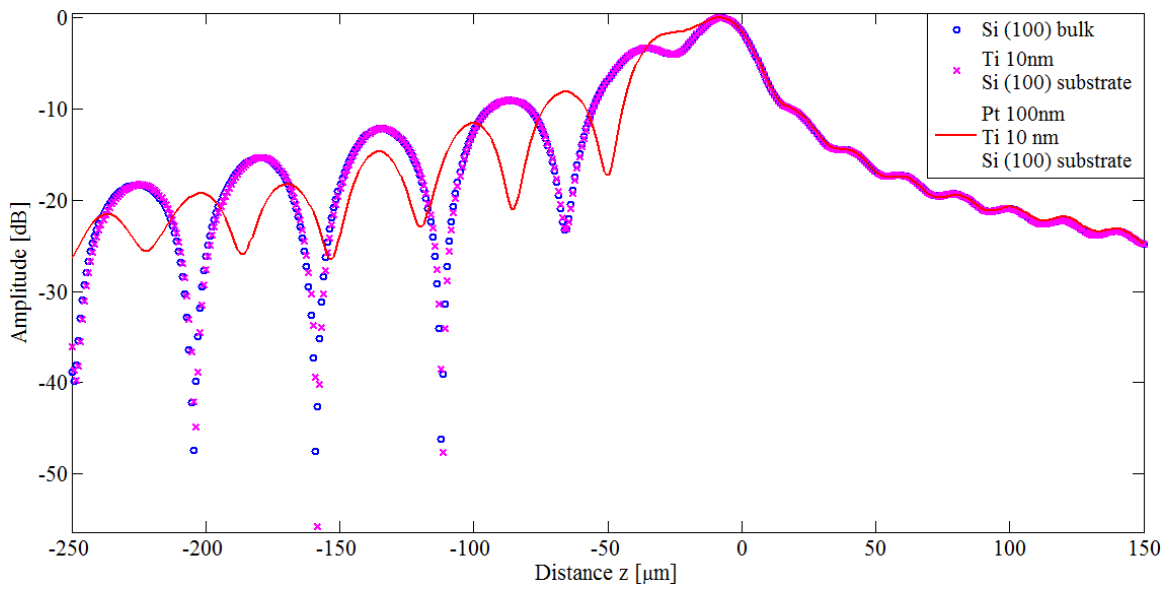


Figure 4-4. Three V(z) curve simulations of the models in Group 1.

Table 4-3. Surface acoustic wave velocities calculated from the  $V(z)$  curves in Fig. 4-3.

Surface acoustic wave velocity	
Model (1)	4762.32 [m/s]
Model (2)	4762.32 [m/s]
Model (3)	4604.93 [m/s]

Figure 4-3 and Table 4-3 present the three simulated  $V(z)$  curves and the surface acoustic wave velocities of the models in Group 1. From Fig 4-3 and Table 4-3, first, it can be observed that the  $V(z)$  curves of Model (1) and Model (2) are hardly distinguished from each other and their calculated surface acoustic wave velocities are the same. That is, the simulation is not sensitive enough to distinguish 10 nm of thickness change of titanium with a 400 MHz operating frequency. Yet, Model (3) yields a very different shape of  $V(z)$  curve and surface acoustic wave velocity than the two others. This result indicates that the thickness sensitivity of the simulation is precise enough to differentiate the 100 nm thickness platinum coating with an operating frequency of 400 MHz.

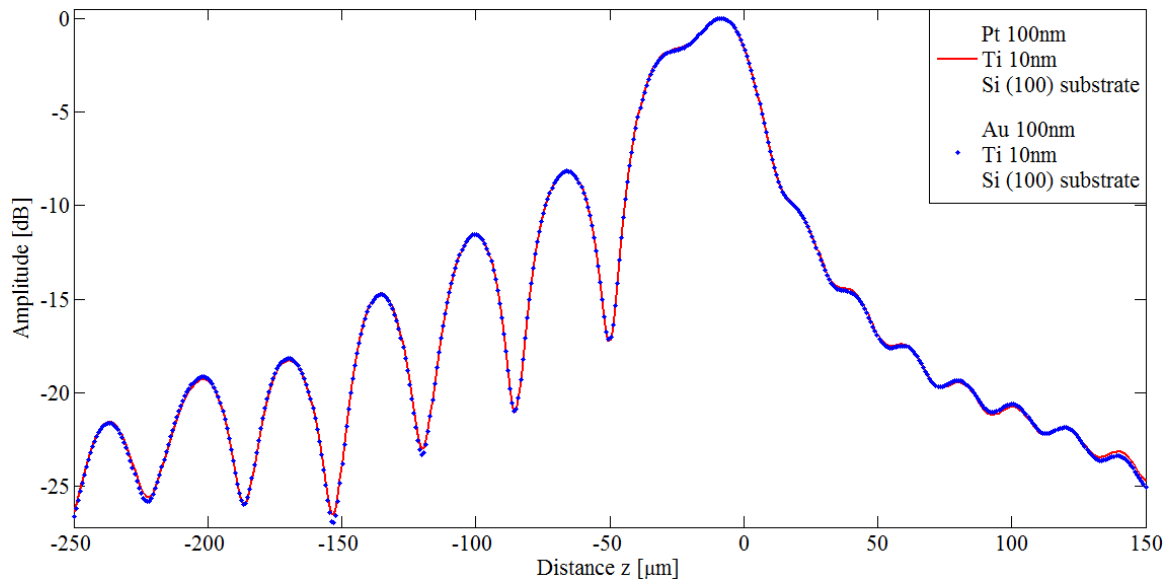
Figure 4-5. Two  $V(z)$  curve simulations of the models in Group 1.



Table 4-4. Surface acoustic wave velocities calculated from the  $V(z)$  curves in Fig. 4-4.

Surface acoustic wave velocity	
Model (3)	4604.93 [m/s]
Model (4)	4608.11 [m/s]

Figure 4-4 and Table 4-4 show the two simulated  $V(z)$  curves and the surface acoustic wave velocities of the models in Group 2. From Fig 4-4, it can be observed that the  $V(z)$  curves of Model (3) and Model (4) are indistinguishable from each other. Yet, even though it is subtle, Model (3) and Model (4) yield different surface acoustic wave velocities in Table 4-4. This result implicates that the simulation is sensitive enough to differentiate platinum and gold which have the same thickness with an operating frequency of 400 MHz.

### 4.3 Simulation vs. Experiment in Multilayered Materials

The last step of validating the credibility of the  $V(z)$  simulation software will be a comparison between simulation and experiment in multilayered materials. This step was conducted not only to explore how well the simulation results matched with experimental results but also to observe if the simulation result could be utilized as a reference to evaluate the adhesive status of materials and the applied adhesion process. The following model and samples were prepared and shown in Fig. 4-5.

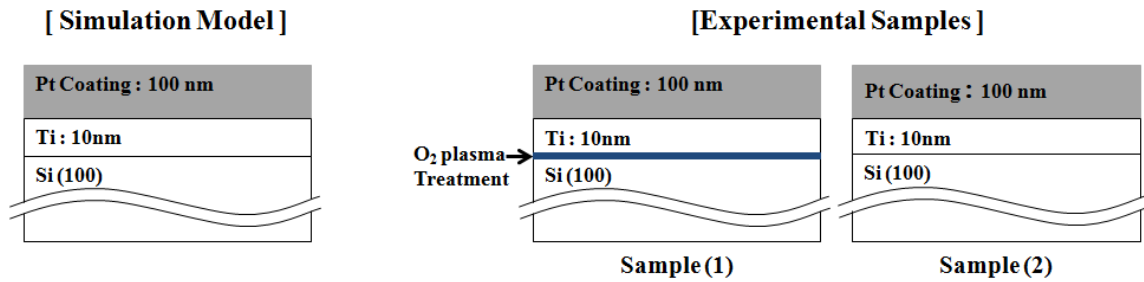


Figure 4-6. A multilayered model for simulation (Left) and its real samples prepared for experiment (Right).

Prior to the comparison discussion it would be beneficial to look at the samples and the difference in their preparation process briefly.

- Sample (1) : 10 nm of titanium was deposited to a silicon (100) substrate prior to the deposition of 100 nm of platinum. To enhance the adhesion of the metal, the sample was pre-treated with O<sub>2</sub> plasma. The plasma condition was 150 sccm of O<sub>2</sub> flow, 50 sccm of He flow, up to 500 mTorr of pressure, 300 W of power, and 1 minute of treatment time.
- Sample (2) : 10 nm of titanium was deposited to the silicon (100) substrate prior to the deposition of 100 nm of platinum without the treatment.

Figure 4-6 shows the three  $V(z)$  curves from the simulation and the experiment and Table 4-5 exhibits surface acoustic wave velocities calculated from the three  $V(z)$  curves.

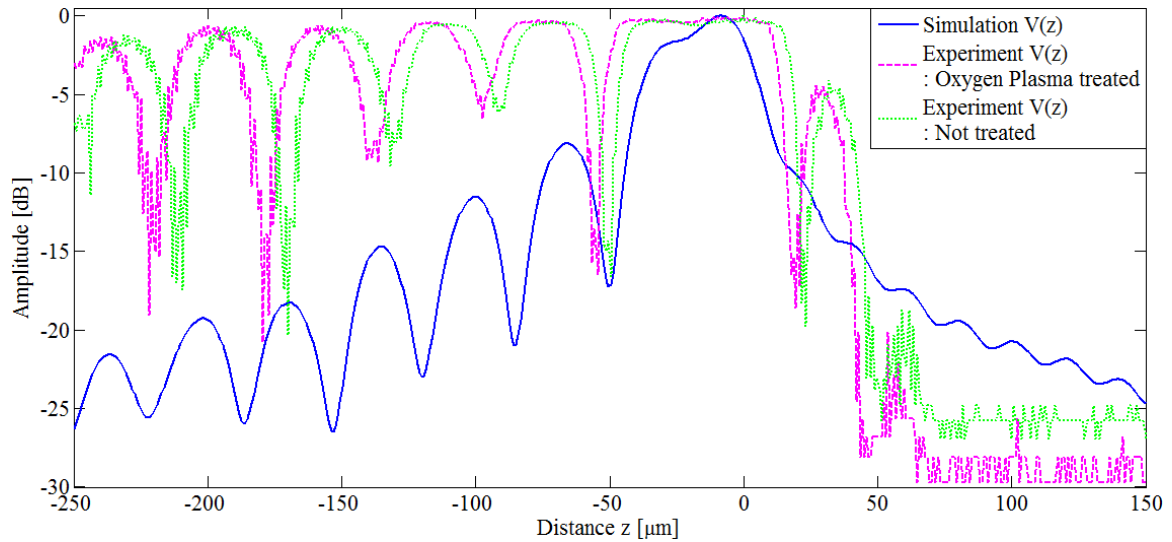


Figure 4-7.  $V(z)$  curves obtained from the simulation and the experiment.

Table 4-5. Surface acoustic wave velocities calculated from  $V(z)$  curves in Fig. 4-6.

Surface acoustic wave velocity	
Simulation Model	4604.93 [m/s]
Experimental Sample (1)	4323.99 [m/s]
Experimental Sample (2)	4259.55 [m/s]

From Table 4-5, it can be observed that the Simulation Model has the fastest surface acoustic wave velocity and Experimental Sample (1), which had  $O_2$  plasma treatment, has a faster surface acoustic wave velocity than Experimental Sample (2), which had no treatment. This is very legitimate since the simulation assumes a perfect bonding of each layer and the  $O_2$  plasma treatment in Experimental Sample (1) was performed to provide better adhesion. Moreover, it suggests that a simulation result can be utilized as a reference to assess the adhesive status of the materials and/or performance of the treatment method/process for strengthening adhesion. In a

similar manner, the 6% discrepancies between the surface acoustic wave velocity of the Simulation Model and that of Experiment Sample (1) and the 8% discrepancies between the surface acoustic wave velocity of the Simulation Model and that of Experimental Sample (2) could be explained.

## Chapter 5

### Discussion and Future Works

The results of the previous chapters validate the simulation program's reliability and usefulness. In the first comparison, the simulation software's accuracy was tested by comparing the surface acoustic wave velocity the simulation produced and the surface acoustic wave velocity calculated with the experiment in silicon (100). The two calculations matched with a great degree of agreement with a discrepancy of 0.16 %.

Secondly, the following four models were simulated, silicon (100), 10 nm of titanium on a silicon (100) substrate, 100 nm of platinum coating on a 10 nm thick titanium deposit on a silicon (100) substrate, and 100 nm of gold coating on a 10 nm thick titanium deposit on a silicon (100) substrate. By comparing the  $V(z)$  curves and the calculated surface wave velocities of the four models, the thickness sensitivity of the simulation was tested. Silicon (100) could not be differentiated from the 10 nm of titanium deposited on a silicon (100) substrate which has 10 nm of thickness difference by inspecting the respective  $V(z)$  curves and surface acoustic wave velocities. However, a significant change could be seen in the  $V(z)$  curve with 100 nm of platinum coating applied. This verifies that scanning acoustic microscopy can be applied to nanoscale materials using a 400 MHz operating frequency acoustic lens. Also the simulation could distinguish a sample with 100 nm of platinum coating deposited and one with 100 nm of gold coating deposited. Although the difference was subtle, the calculations of surface acoustic wave velocities yielded different values so one could discriminate between the two.

Finally simulation and experiments in a multilayered solid were compared. A model with a 100 nm platinum coating on 10 nm titanium deposited on silicon (100) was simulated.

Experiments were carried out with specimens that had the same properties, one with an O<sub>2</sub> plasma treatment between titanium and silicon (100) layers and one without any treatment. The results showed the surface acoustic wave velocity of the simulation was faster than that of the experiment with the O<sub>2</sub> plasma treated sample and the slowest velocity for the experiment was with the sample that was not treated. From this result the effectiveness of the treatment could be shown, along with possible applications of  $V(z)$  curves, and reasons for the discrepancy between the simulation and the experiments.

During this research certain things that could be addressed in future works were discovered to improve the  $V(z)$  curve simulation software in terms of accuracy and applications. First, the  $V(z)$  curve simulation can be improved by applying a more accurate pupil function in the  $V(z)$  equation. The pupil function applied in the simulation software is very simplified, and the simplification of the pupil function causes the amplitude of the simulated  $V(z)$  curves to be different from the amplitude of the experimentally taken  $V(z)$  curves. This limitation can be overcome by finding a more sophisticated pupil function. The pupil function can be mathematically obtained by modeling an acoustics lens, and calculating the pressure field in front of the transducer at the focal point, and then fitting a polynomial to the calculated pressure field. The pupil function for an acoustic lens can also be experimentally acquired by getting an image of the fringe of a circle from scanning the tip of a needle, and writing code to map the fringe image to a three-dimensional function which is the pupil function of the acoustic lens.

Moreover, the scope of the  $V(z)$  curve simulation software can be extended to simulate  $V(z)$  curves for nanoscaled multilayered thin film systems with anisotropic substrates. This can be done not only for nanoscaled multilayered thin film systems with isotropic substrates, or for cubicle substrates with perpendicular angle, such as silicon (100) but also for anisotropic substrates. There have been works to evaluate elastic properties of anisotropic bulk materials by applying line-focused acoustic lenses but not for multilayered thin film systems with anisotropic

substrates. Mathematical models of line-focused acoustic lenses can be found and applied to the  $V(z)$  curve simulation software to extend the application range to nanoscaled multilayered thin film systems with anisotropic substrates.

## **Chapter 6**

### **Conclusion**

To extend the application range of the  $V(z)$  curve method, especially to multilayer structured thin film systems, a  $V(z)$  curve simulation software was developed. To verify the credibility of the software package, the  $V(z)$  equation and reflectance function for multilayered solids were analyzed. By taking advantage of the computing and programming capability of MATLAB, the  $V(z)$  equation was applied and the transfer matrix method was utilized to calculate the reflectance function in the simulation software. It was designed to simulate the transducer's output voltage when ultrasound is emitted to the specimen in a scanning acoustic microscope. From the simulated  $V(z)$  curve, the surface acoustic wave velocity was calculated. To verify the performance several comparisons were conducted. Through the comparisons, the simulation's reliability and thickness sensitivity were shown. The possibility to extend the use of the software to other applications such as the evaluation of the adhesive condition and adhesion process in multilayer structured thin film systems was also illustrated.



## References

- [1] K. L. MITTAL, "ADHESION MEASUREMENT OF THIN FILMS", Electro component Science and Technology", Vol. 3. 21-42 (1976)
- [2] S. Pathasarathi, M. D. Aesope, K. Sampath, and B. R. Tittmann, "Thermal Wave Imaging and Ultrasonic Characterization of Defects in Plasma Sprayed Coating", Journal of Materials and Manufacturing Processes, Vol. 10, No. 5, 1077-1086 (1995)
- [3] B. Roge, A. Fahr, J. S. R. Giguere, and K. I. Mcare, "Nondestructive Measurement of Porosity in Thermal Barrier Coating", Journal of Thermal Spray Technology, Vol. 12, No. 4, 530-535 (2003)
- [4] E. R. Doering, G. J. Havrilla, and T. C. Miller, "Disilicide Diffusion Coating Inspection by Micro X-Ray Fluorescence Imaging", Journal of Nondestructive Evaluation, Vol. 23, No. 3, 95-105 (2004)
- [5] S. Pathasarathi, "Rayleigh wave potential for thin film characterization", Ph. D Thesis, The Pennsylvania State University.
- [6] J. Du, "Toward the Acoustic Evaluation of Low Modulus Thin Film Structures", Ph. D Thesis, The Pennsylvania State University.
- [7] D. P. Almond, R. L. Cox, M. Moghi, and H. Reiter, "Acoustic Properties of Plasma Sprayed Coatings and their Application to Nondestructive Evaluation", Thin Solid Film", Vol. 83, 311-324 (1989)
- [8] D. Jiao, and J. L. Rose, "An ultrasonic interface model for bond evaluation", Journal of Adhesion Science and Technology, Vol. 5, No. 8, 631-646 (1991)
- [9] P. Xu, K. E. Lindenschmidt, and S. A. Meguid, "A new high-frequency analysis of coating using leaky Lamb waves", Journal of Acoustic Society of America, Vol. 94, No. 5, 2954-2962 (1993)
- [10] C. C. Berndt, "Failure Processes within ceramic Coating at High Temperatures", Journal of Materials Sciences, Vol. 24, 3511-3520 (1989)
- [11] W. T. Thomson, "Transmission of Elastic Waves through a Stratified Solid Medium", Journal of Applied Physics, Vol. 21, No. 2, 89-93 (1987)
- [12] V. K. Kinra, and C. Zhy, "Ultrasonic Nondestructive Evaluation of Thin Coatings", Journal of Acoustic Society of America, Vol. 93, No. 5, 2454-2467 (1993)
- [13] R. C. Bray, C. F. Quate, J. Calhoun, and R. Koch, "Film Adhesion Studies with the Acoustic Microscope", Thin Solid films, Vol. 74, 295-302 (1980)

- [14] R. C. Addison Jr., M. Somekh, and G. A. D. Briggs, "Techniques for the Characterization of Film Adhesion", Proceedings of IEEE Ultrasonic Symposium, Williamsburg, U.S.A., November 17-19, 775-782 (1986)
- [15] R. C. Addison, and D. B. Marshall, "Correlation of Thin-Film Bond Compliance and Bond Fracture Resistance", Review of Progress in Quantitative Nondestructive Evaluation, 7B, Plenum, 1185-1194 (1988)
- [16] A. K. Mal, and R. D. Weglein, "Characterization of Film Adhesion by Acoustic Microscopy", Review of Progress in Quantitative Nondestructive Evaluation, 7B, Plenum, 903-910 (1988)
- [17] P. Richard, G. Gremaud, and A. Kulik, "Thin Film Adhesion Investigation With the Acoustic Microscope", Proceedings of the IEEE Ultrasonics Symposium, 1425-1428 (1994)
- [18] P. Richard, J. Thomas, D. Landolt, and G. Gremaud, "Combination of scratch-test and acoustic microscopy imaging for the study of coating adhesion", Surface Coatings Technology, Vol. 91, 83-90 (1997)
- [19] S. Parthasarathi, B. R. Tittmann, and R. J. Ianno, "Quantitative Acoustic Microscopy for Characterization of the Interface Strength of Diamond-Like Carbon Thin Films", Thin Solid Films, Vol. 300, 42-50 (1997)
- [20] S. Parthasarathi, B. R. Tittmann, and M. Nishida, "Characterization of Film Interface Integrity through Scanning Acoustic microscopy", Surface & Coatings Technology, Vol. 105, 1-7 (1998)
- [21] K. Kosbi, T. Blum, U. Scheer, and S. Boseck, "Evaluation of imperfect gold/ glass interfaces using scanning acoustic microscopy", Proc. SPIE, 3581, 314, (1998)
- [22] A. Pageler, T. Blum, K. Kosbi, U. Scheer and S. Boseck, "Determination of Bonding Properties in Layered Metal Silicon Systems Using Sezawa Wave Modes", Acoustic imaging, Vol. 24, 229-235 (2000)
- [23] Z. Guo, and J. D. Achenbach, "Modeling Quantitative Acoustic Microscopy for Layered Coatings", Review of Progress in Quantitative Nondestructive Evaluation, 18B, 1409-1416 (1999)
- [24] Z. Guo, J. D. Achenbach, A. Madan, K. Martin, and M. E. Graham, "Modeling and Acoustic Microscopy Measurements for Evaluation of the Adhesion between a Film and a Substrate", Thin Solid Films, Vol. 394, 188-200 (2001)
- [25] J. Du, B. R. Tittmann, and H. S. Ju, "Evaluation of film adhesion to substrates by means of surface acoustic wave dispersion", Thin Solid Films, Vol. 518, 5786-5795 (2010)
- [26] S. Y. Sokolov, "The Ultrasonic microscope", Academia Nauk SSSR Doklady, 64(3), 333-335, (1949)

- [27] R. A. Lemons, and C. F. Quate, "Acoustic microscope-scanning version", *Appl. Phys. Lett.* 24, 163-165 (1974).
- [28] A. Atalar, C. F. Quate, and H. K. Wickramasinghe, "Phase imaging in reflection with the acoustic microscope", *Appl. Phys. Lett.* 13, 791 (1977).
- [29] R. D. Weglein, "A model for predicting acoustic material signatures", *Appl. Phys. Lett.* 34, 179-181 (1979).
- [30] H. L. Bertoni, and T. Tamir, "Unified theory of Rayleigh-angle phenomena for acoustic beams at liquid-solid interfaces", *Appl. Phys.* 2, 157-172 (1973).
- [31] M. A. Breazeale, L. Adler, and G. W. Scott, "Interaction of ultrasonic waves incident at the Rayleigh angle onto a liquid solid interface", *J. Appl. Phys.* 48, 530-537 (1977).
- [32] A. Atalar, "An angular-spectrum approach to contrast in reflection acoustic microscopy", *Appl. Phys. Lett.* 49, 1530-1539 (1978).
- [33] J. W. Goodman, [Introduction to Fourier Optics], McGraw-Hill, New York, 48 (1968).
- [34] W. Parmon, and H. L. Bertoni, "Ray interpretation of the material signature in the acoustic microscope", *Electron. Lett.* 15, 648-686 (1979).
- [35] R. G. Wilson, and R. D. Weglein, "Acoustic microscopy of materials and surface layers", *J. Appl. Phys.* 55, 3261-3275 (1984).
- [36] T. Kundu, A. K. Mal, and R. D. Weglein, "Calculation of the acoustic material signature of a layered solid", *J. Acoust. Soc. Am.*, Vol.77, No.2, 353-361 (1985).
- [37] T. Endo, C. Abe, M. Sakai, and M. Ohono, "Measurement of Dispersion Relations in Acoustic Velocities for the Thin Film on an Anisotropic Substrate Using Acoustic Microscope," *Proc. Ultrasonic International 93 Conference*, 45 (1993).
- [38] F. Zhang, S. Krishnaswamy, D. Fei, D. A. Rebinsky, and B. Feng, "Ultrasonic characterization of mechanical properties of Cr- and W-doped diamond-like carbon hard coatings," *Thin Solid Films*, 503, 250-258 (2006).
- [39] M. Schlesinger, [Modern Aspects of Electrochemistry No. 44 Modelling and Numerical Simulations II], Springer, Dordrecht, Heidelberg, London, New York, Chapter 9, 409-450 (2009).
- [40] Z. Yu, and S. Boseck, "Scanning acoustic microscopy and its applications to material characterization," *Rev. Mod. Phys.* 67(4), 863-891 (1995).
- [41] Olympus, [Olympus UH3 Scanning Acoustic Microscopy Application Software Manual volume 2], Olympus, 122-126 (1993).
- [42] J. Kushibiki, and N. Chubachi, "Material Characterization by Line-Focus-Beam Acoustic

Microscope," IEEE Trans. Sonics., SU-32(2), 189-212 (1985).

[43] B.R. Tittmann, and C. Miyasaka, [Encyclopedia of Imaging Science and Technology], ISBN: 9780471443391, Wiley, Malden MA, USA, 1228-1248 (2002)

[44] Website of VN Instruments Ltd, <http://www.vninstruments.com/SignalTypesPage.htm>

[45] Y. Sasaki, T. Endo, T. Yamagishi, M. Sakai, "Thickness measurement of a thin-film layer on an anisotropic substrate by phase-sensitive acoustic microscope", IEEE Trans UFFC-39(5), 638-642 (1992)

[46] K. Liang, G. S. Kino, and B. T. Khuri-Yakub, "Material characterization by the inversion of  $V(z)$ ", IEEE Trans SU-32, 213 (1985)

[47] T. Endo, Y. Sasaki, T. Yamagishi, and M. Sakai, "Determination of Sound Velocities by High Frequency Complex  $V(z)$  Measurement in Acoustic Microscopy", Jpn J. Appl Phys 31, 160 (1992)

[48] J. Kushibiki, K. Horii, and N. Chubachi, "Velocity measurement of multiple leaky waves on germanium by line-focus-beam acoustic microscope using FFT", Electron Lett. 19(11), 404-405 (1983)

[49] J. Kushibiki, T. Kobayashi, H. Ishiji, and N. Chubachi, "Elastic properties of 5-mol % MgO doped  $\text{LiNbO}_3$  crystals measured by line focus beam acoustic microscopy", Appl Phys Lett. 61(18), 2164 -2166 (1992)

[50] J. Kushibiki, M. Miyashita, and N. Chubachi, "Quantitative characterization of proton-exchanged layers in  $\text{LiTaO}_3$  optoelectronic devices by line-focus-beam acoustic microscopy", IEEE Photonics Techno. Lett. 8(11), 1516-1518 (1996)

[51] J. Kushibiki, and M. Miyashita, "Characterization of Domain-Inverted Layers in  $\text{LiTaO}_3$  by Line-Focus-Beam Acoustic Microscopy", Jpn J. Appl. Phys. 36(7B), 959-961 (1997)

[52] J. Kushibiki, and M. Arakawa, "A method for calibrating the line-focus-beam acoustic microscopy system", IEEE Trans UFFC-45(2), 421-430 (1998)

[54] Website of Onda Corporation, <http://www.ondacorp.com/contact.shtml>

[55] [http://www.cleanroom.byu.edu/EW\\_orientation.phtml](http://www.cleanroom.byu.edu/EW_orientation.phtml)

## Appendix A

### V(z) simulation software – Scripts and Functions

The V(z) simulation software consists of nine script and eight function source files. In this section, configurations of the main source files are discussed with flow charts. Figure A-1 shows the script and function files of the V(z) simulation software.

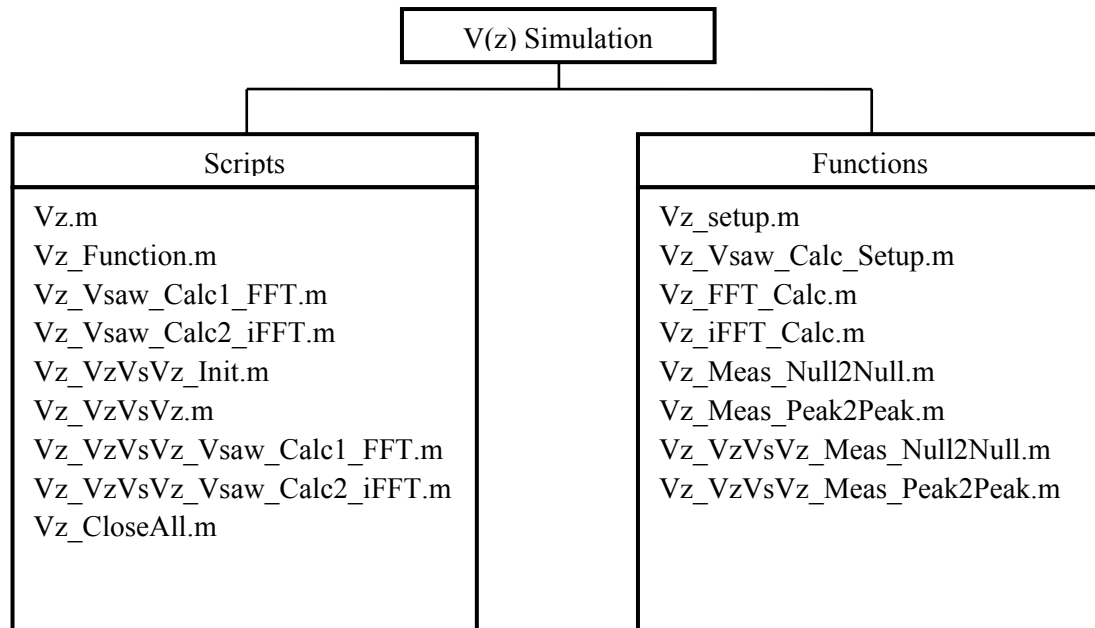


Figure A-1. Scripts and functions that construct the V(z) simulation software.

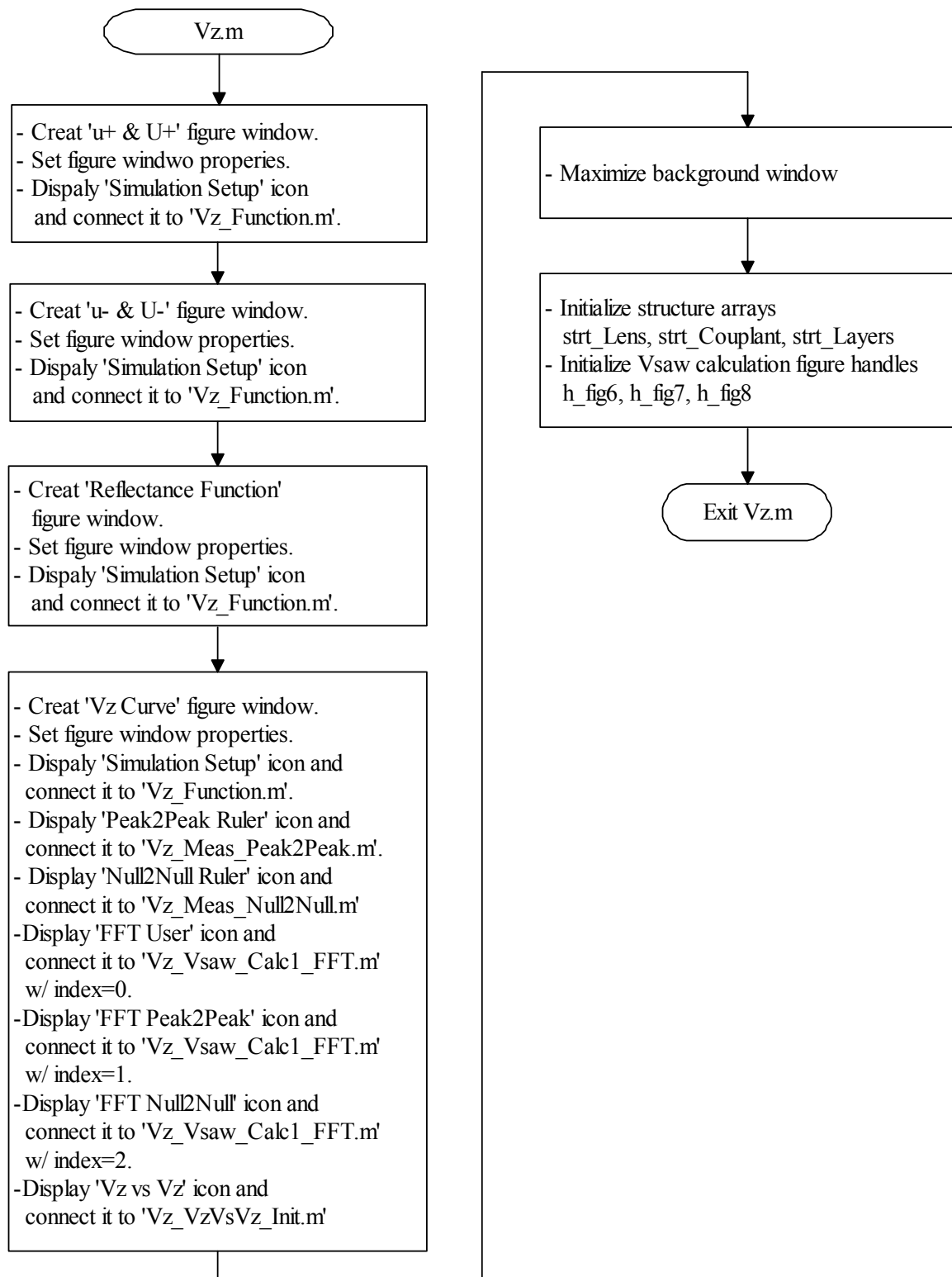


Figure A-2. Flow chart for a source code, Vz.m

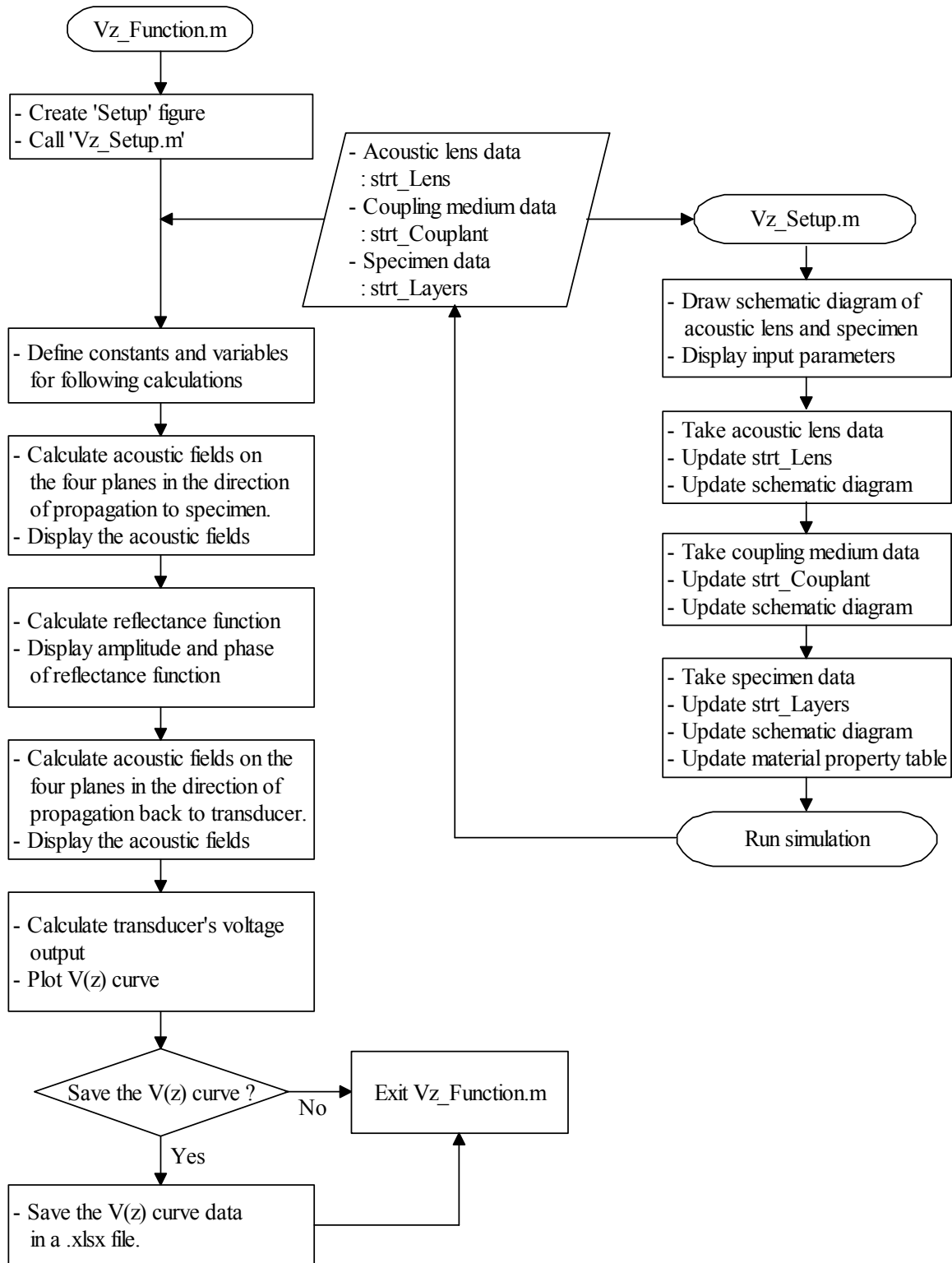


Figure A-3. Flow chart for source codes, `Vz_Function.m` and `Vz_Setup.m`

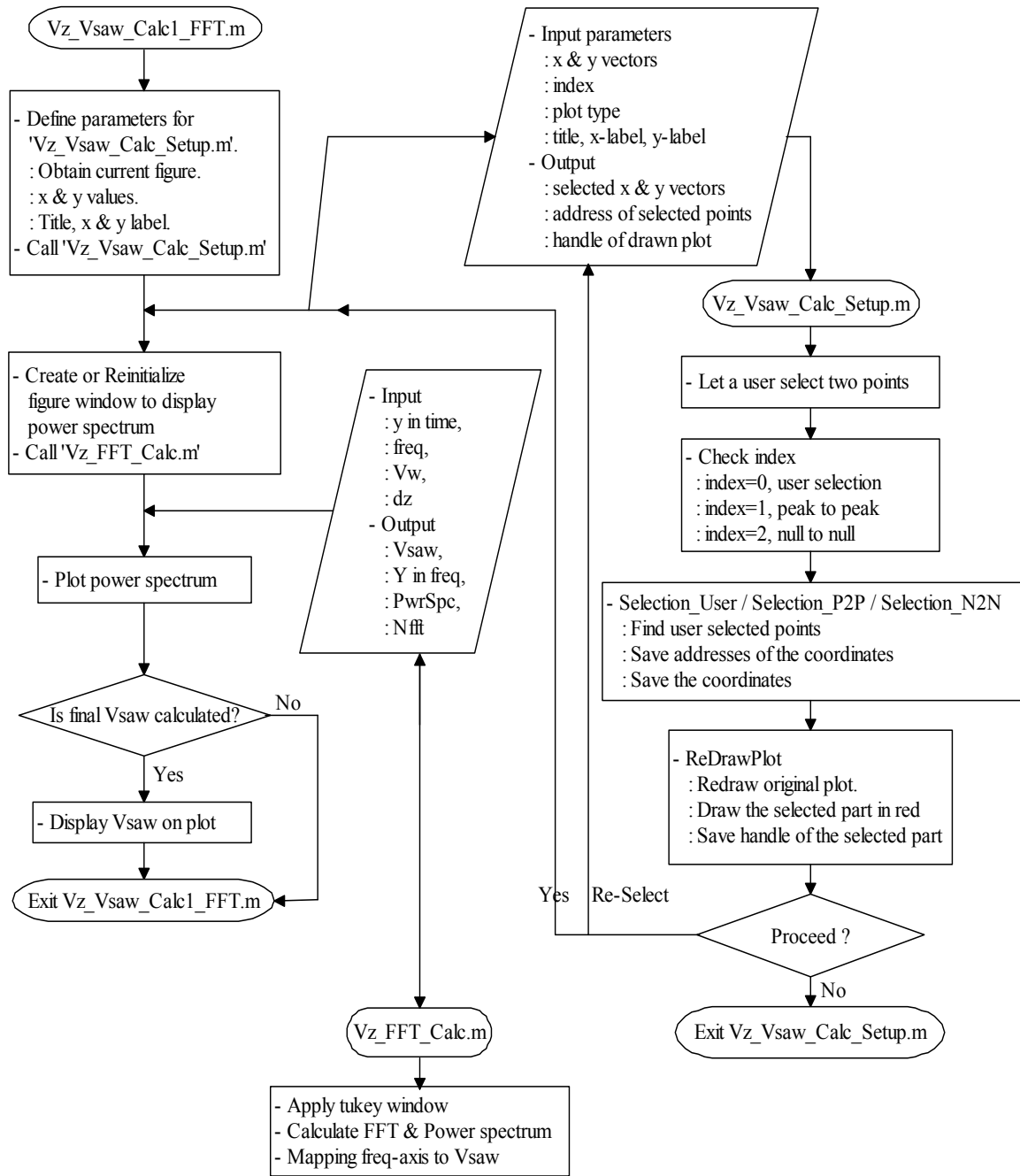


Figure A-4. Flow chart for source codes, `Vz_Vsaw_Calc1_FFT.m`, `Vz_Vsaw_Calc_Setup.m`, and `Vz_FFT_Calc.m`



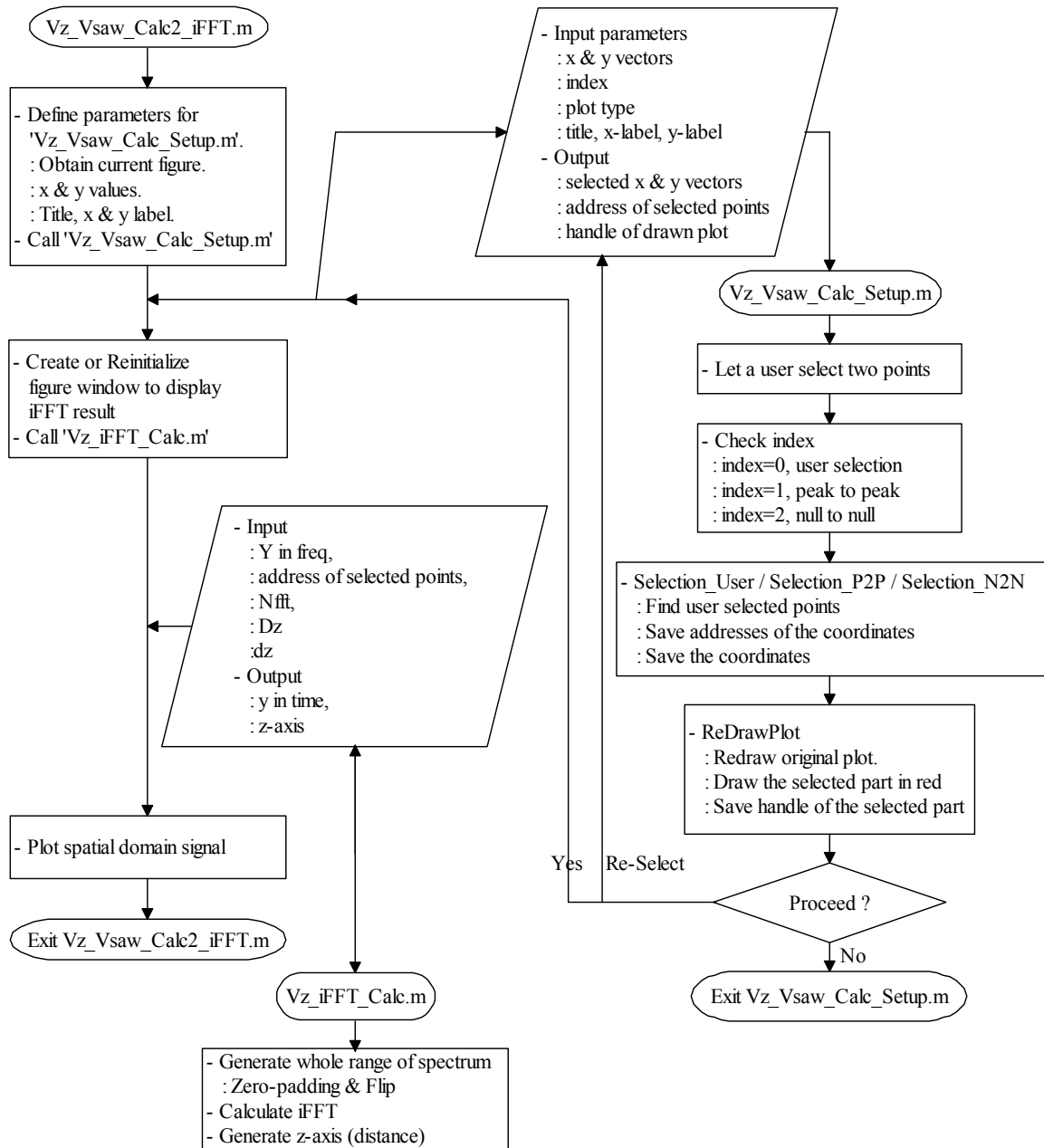


Figure A-5. Flow chart for source codes, `Vz_Vsaw_Calc2_iFFT.m`, `Vz_Vsaw_Calc_Setup.m`, and `Vz_iFFT_Calc.m`.

## Appendix B

### Specifications of Acoustic Lenses

In this section, specifications of the acoustic lenses listed in the V(z) simulation software are introduced. Additional lenses can be simply added in the ‘AcousticLens\_ParameterList.xlsx’ file with proper specification. Then, the V(z) simulation software automatically update its list.

Table B-1. Specification of AL1M3125

AL1M3125 (manufacturer : Olympus)		
Transducer	Material	Zinc Oxide
	Center Frequency [MHz]	100.00
	Radius [μm]	500.00
	Distance to Back Focal Plane [μm]	7011.00
Buffer Rod	Material	Sapphire (C-cut)
	Longitudinal acoustic wave velocity [m/sec]	11175.00
	Shear acoustic wave velocity [m/sec]	6950.00
	Density [kg/m <sup>3</sup> ]	3980.00
Lens	Aperture Angle [degree]	60.0
	Aperture Diameter [μm]	1250.00
	Curvature of the Radius [μm]	1250.00
	Focal Distance [μm]	1443.80
Matching Layer (AARC)	Material	Silicon Oxide
	Longitudinal acoustic wave velocity [m/sec]	5970.00
	Shear acoustic wave velocity [m/sec]	3760.00
	Density [kg/m <sup>3</sup> ]	2200.00
	Thickness [μm]	1392.00
Measuring Property	Measuring Range [μm]	800.00
	Measuring Pitch [μm]	1.60

Table B-2. Specification of AL2M3125

AL2M3125 (manufacturer : Olympus)		
Transducer	Material	Zinc Oxide
	Center Frequency [MHz]	200.00
	Radius [μm]	500.00
	Distance to Back Focal Plane [μm]	7011.00
Buffer Rod	Material	Sapphire (C-cut)
	Longitudinal acoustic wave velocity [m/sec]	11175.00
	Shear acoustic wave velocity [m/sec]	6950.00
	Density [kg/m <sup>3</sup> ]	3980.00
Lens	Aperture Angle [degree]	60.0
	Aperture Diameter [μm]	1250.00
	Curvature of the Radius [μm]	721.70
	Focal Distance [μm]	833.60
Matching Layer (AARC)	Material	Silicon Oxide
	Longitudinal acoustic wave velocity [m/sec]	5970.00
	Shear acoustic wave velocity [m/sec]	3760.00
	Density [kg/m <sup>3</sup> ]	2200.00
	Thickness [μm]	696.00
Measuring Property	Measuring Range [μm]	800.00
	Measuring Pitch [μm]	1.60

Table B-3. Specification of AL2M631

AL2M631 (manufacturer : Olympus)		
Transducer	Material	Zinc Oxide
	Center Frequency [MHz]	200.00
	Radius [ $\mu\text{m}$ ]	383.00
	Distance to Back Focal Plane [ $\mu\text{m}$ ]	6122.00
Buffer Rod	Material	Sapphire (C-cut)
	Longitudinal acoustic wave velocity [m/sec]	11175.00
	Shear acoustic wave velocity [m/sec]	6950.00
	Density [ $\text{kg/m}^3$ ]	3980.00
Lens	Aperture Angle [degree]	120.0
	Aperture Diameter [ $\mu\text{m}$ ]	866.00
	Curvature of the Radius [ $\mu\text{m}$ ]	500.00
	Focal Distance [ $\mu\text{m}$ ]	577.50
Matching Layer (AARC)	Material	Silicon Oxide
	Longitudinal acoustic wave velocity [m/sec]	5970.00
	Shear acoustic wave velocity [m/sec]	3760.00
	Density [ $\text{kg/m}^3$ ]	2200.00
	Thickness [ $\mu\text{m}$ ]	696.00
Measuring Property	Measuring Range [ $\mu\text{m}$ ]	400.00
	Measuring Pitch [ $\mu\text{m}$ ]	0.80

Table B-4. Specification of AL4M350

AL4M350 (manufacturer : Olympus)		
Transducer	Material	Zinc Oxide
	Center Frequency [MHz]	400.00
	Radius [μm]	383.00
	Distance to Back Focal Plane [μm]	6122.00
Buffer Rod	Material	Sapphire (C-cut)
	Longitudinal acoustic wave velocity [m/sec]	11175.00
	Shear acoustic wave velocity [m/sec]	6950.00
	Density [kg/m <sup>3</sup> ]	3980.00
Lens	Aperture Angle [degree]	60.0
	Aperture Diameter [μm]	500.00
	Curvature of the Radius [μm]	500.00
	Focal Distance [μm]	577.50
Matching Layer (AARC)	Material	Silicon Oxide
	Longitudinal acoustic wave velocity [m/sec]	5970.00
	Shear acoustic wave velocity [m/sec]	3760.00
	Density [kg/m <sup>3</sup> ]	2200.00
	Thickness [μm]	348.00
Measuring Property	Measuring Range [μm]	400.00
	Measuring Pitch [μm]	0.80

Table B-5. Specification of AL4M631

AL4M631 (manufacturer : Olympus)		
Transducer	Material	Zinc Oxide
	Center Frequency [MHz]	400.00
	Radius [μm]	383.00
	Distance to Back Focal Plane [μm]	6122.00
Buffer Rod	Material	Sapphire (C-cut)
	Longitudinal acoustic wave velocity [m/sec]	11175.00
	Shear acoustic wave velocity [m/sec]	6950.00
	Density [kg/m <sup>3</sup> ]	3980.00
Lens	Aperture Angle [degree]	120.0
	Aperture Diameter [μm]	866.00
	Curvature of the Radius [μm]	500.00
	Focal Distance [μm]	577.50
Matching Layer (AARC)	Material	Silicon Oxide
	Longitudinal acoustic wave velocity [m/sec]	5970.00
	Shear acoustic wave velocity [m/sec]	3760.00
	Density [kg/m <sup>3</sup> ]	2200.00
	Thickness [μm]	348.00
Measuring Property	Measuring Range [μm]	400.00
	Measuring Pitch [μm]	0.80

Table B-6. Specification of AL6M615

AL6M615 (manufacturer : Olympus)		
Transducer	Material	Zinc Oxide
	Center Frequency [MHz]	600.00
	Radius [μm]	361.00
	Distance to Back Focal Plane [μm]	7690.00
Buffer Rod	Material	Sapphire (C-cut)
	Longitudinal acoustic wave velocity [m/sec]	11175.00
	Shear acoustic wave velocity [m/sec]	6950.00
	Density [kg/m <sup>3</sup> ]	3980.00
Lens	Aperture Angle [degree]	120.0
	Aperture Diameter [μm]	433.00
	Curvature of the Radius [μm]	250.00
	Focal Distance [μm]	288.80
Matching Layer (AARC)	Material	Silicon Oxide
	Longitudinal acoustic wave velocity [m/sec]	5970.00
	Shear acoustic wave velocity [m/sec]	3760.00
	Density [kg/m <sup>3</sup> ]	2200.00
	Thickness [μm]	232.00
Measuring Property	Measuring Range [μm]	200.00
	Measuring Pitch [μm]	0.40

Table B-7. Specification of AL8M607

AL8M607 (manufacturer : Olympus)		
Transducer	Material	Zinc Oxide
	Center Frequency [MHz]	800.00
	Radius [μm]	216.50
	Distance to Back Focal Plane [μm]	5033.00
Buffer Rod	Material	Sapphire (C-cut)
	Longitudinal acoustic wave velocity [m/sec]	11175.00
	Shear acoustic wave velocity [m/sec]	6950.00
	Density [kg/m <sup>3</sup> ]	3980.00
Lens	Aperture Angle [degree]	120.0
	Aperture Diameter [μm]	217.00
	Curvature of the Radius [μm]	125.30
	Focal Distance [μm]	144.70
Matching Layer (AARC)	Material	Silicon Oxide
	Longitudinal acoustic wave velocity [m/sec]	5970.00
	Shear acoustic wave velocity [m/sec]	3760.00
	Density [kg/m <sup>3</sup> ]	2200.00
	Thickness [μm]	174.00
Measuring Property	Measuring Range [μm]	100.00
	Measuring Pitch [μm]	0.20



Table B-8. Specification of AL1G607

AL1G607 (manufacturer : Olympus)		
Transducer	Material	Zinc Oxide
	Center Frequency [MHz]	1000.00
	Radius [μm]	216.50
	Distance to Back Focal Plane [μm]	5033.00
Buffer Rod	Material	Sapphire (C-cut)
	Longitudinal acoustic wave velocity [m/sec]	11175.00
	Shear acoustic wave velocity [m/sec]	6950.00
	Density [kg/m <sup>3</sup> ]	3980.00
Lens	Aperture Angle [degree]	120.0
	Aperture Diameter [μm]	217.00
	Curvature of the Radius [μm]	125.30
	Focal Distance [μm]	144.70
Matching Layer (AARC)	Material	Silicon Oxide
	Longitudinal acoustic wave velocity [m/sec]	5970.00
	Shear acoustic wave velocity [m/sec]	3760.00
	Density [kg/m <sup>3</sup> ]	2200.00
	Thickness [μm]	139.00
Measuring Property	Measuring Range [μm]	100.00
	Measuring Pitch [μm]	0.20


## Appendix C


### V(z) simulation software – Additional Features

There are additional features in the V(z) simulation software which are introduced in Chapter 3. In this section, how to use those features are explained.

Icon(s) :  and 

Description : Rulers to measure distance between peaks or nulls(troughs) .

 automatically finds the nearest maximum amplitude values from where a user clicks and calculate distance between the two chosen peaks.

 automatically finds the nearest minimum amplitude values from where a user clicks and calculate distance between the two chosen minima.

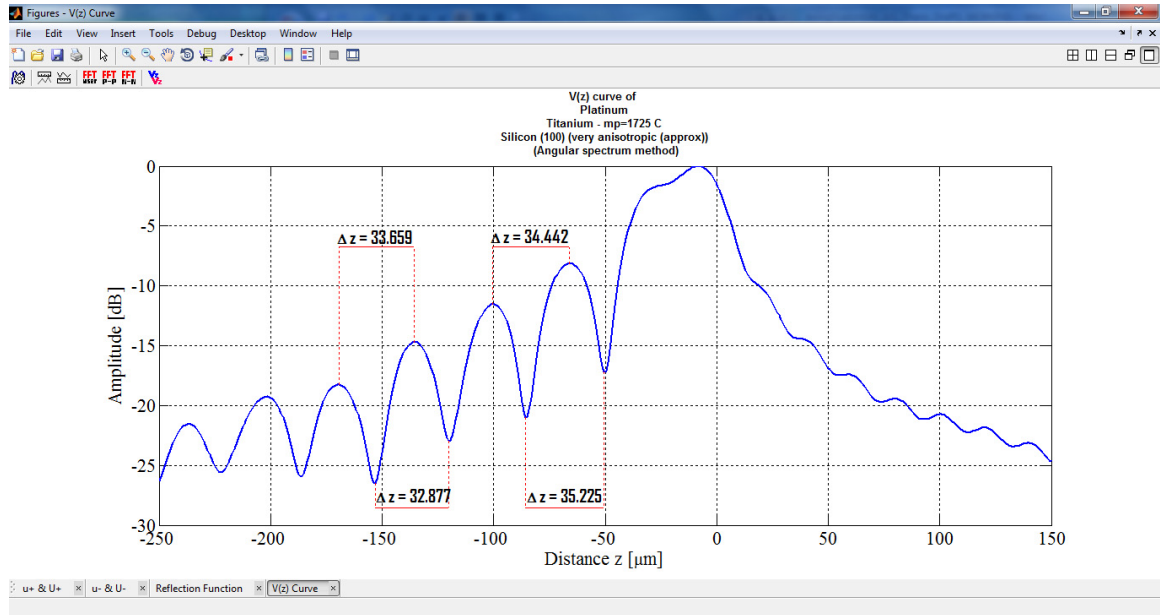



Figure C-1. Usage example of the ruler icons.

Icon(s) : 

Description : Opens a new figure window to read two  $V(z)$  curves in one plot to compare each other. Surface acoustic wave velocity can be calculated for each  $V(z)$  curve.

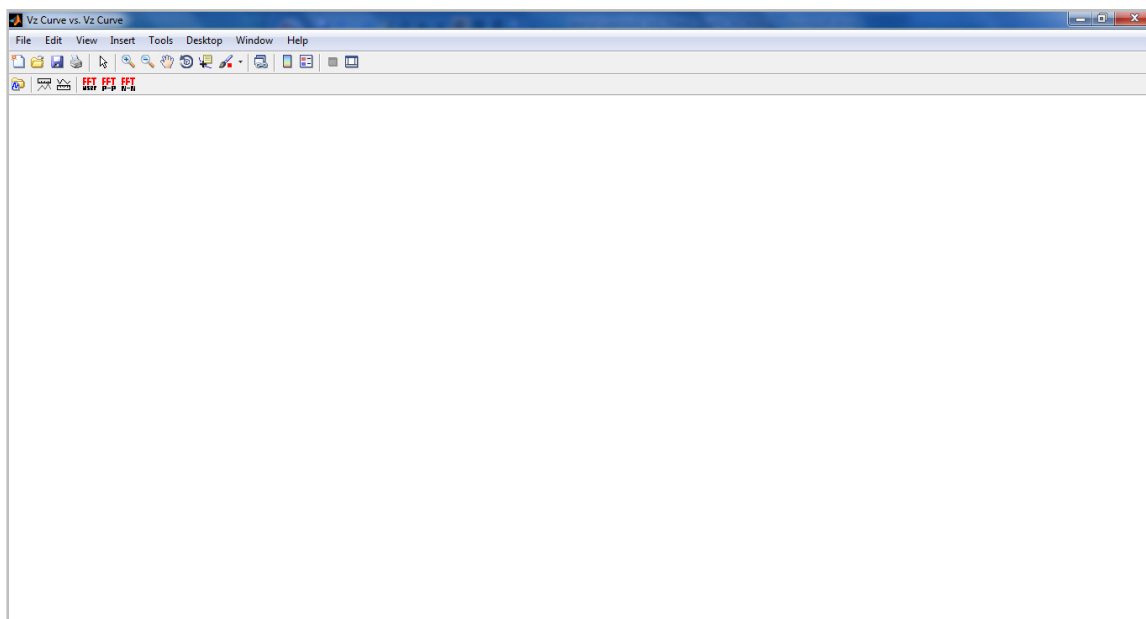



Figure C-2.  $V(z)$  curve vs.  $V(z)$  curve figure window.

Icon(s) : 

Description : Opens 'OPEN  $V(z)$  curves' dialog. Up to two  $V(z)$  curves can be selected to compare each other.  $V(z)$  curves from different directories also can be separately opened.

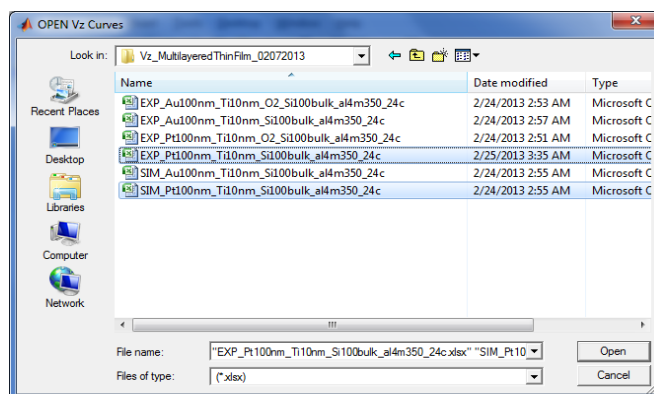


Figure C-3. 'OPEN  $Vz$  Curves' dialog.

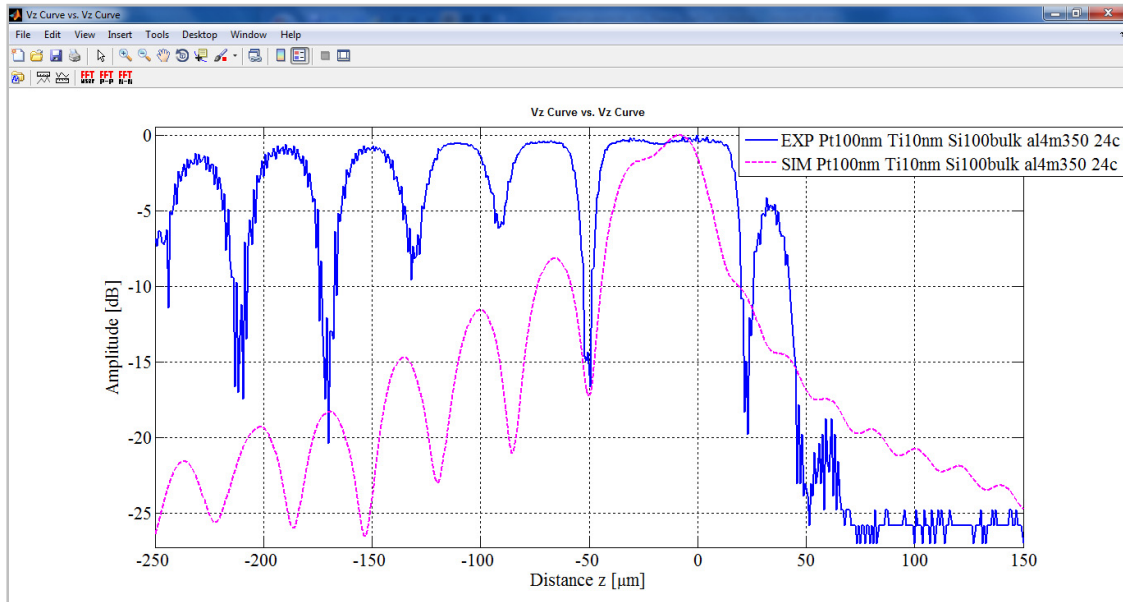


Figure C-4. Two selected  $V(z)$  curves for comparison.

By clicking the right button on a mouse, a user can choose which  $V(z)$  curve to display to calculate the surface acoustic wave velocity from it. The calculation process is introduced in Chapter 3.

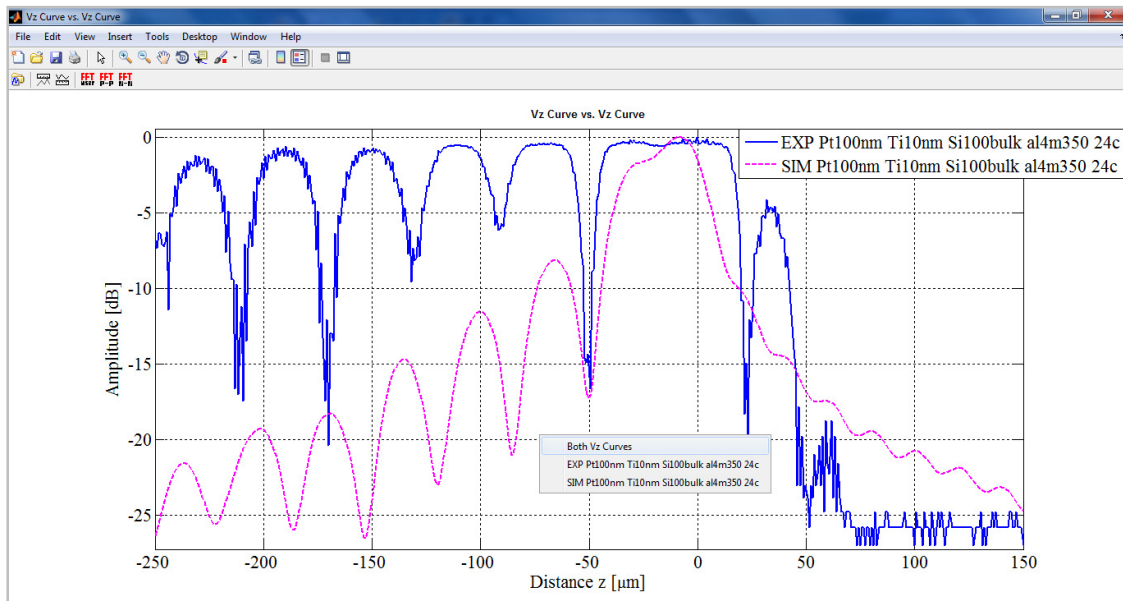


Figure C-5. Selection of a  $V(z)$  curve or both  $V(z)$  curves to display.

## Appendix D

### Material Properties

Materials and material properties used in the  $V(z)$  simulation software is from a website, [http://www.ondacorp.com/tecref\\_acoustictable.shtml](http://www.ondacorp.com/tecref_acoustictable.shtml) [54].  $V_s$ ,  $V_L$ , and  $Z_L$  denote shear acoustic wave velocity, longitudinal acoustic wave velocity, and longitudinal impedance respectively.

Table D-1. Properties of solid materials.

Material	$V_s$ (m/s)	$V_L$ (m/s)	Density (kg/m <sup>3</sup> )	Lame Con. ( $\lambda$ )	Lame Con. ( $\mu$ )	$Z_L$ (kg/s-m <sup>2</sup> )
Alumina		10520	3860			40607200
Aluminum - rolled	3040	6420	2700	61379640000	24952320000	17334000
Aluminum - 6262-T9		6380	2730			17417400
AMD Res-in-all - 502/118, 5:1		2670	1350			3604500
AMD Res-in-all - 502/118, 9:1		2730	1350			3685500
Araldite - 502/956		2620	1160			3039200
Araldite - 502/956, 10phe C5W		2600	1230			3198000
Araldite - 502/956, 20phe C5W		2540	1390			3530600
Araldite - 502/956, 30phe C5W		2410	1500			3615000
Araldite - 502/956, 40phe C5W		2310	1670			3857700
Araldite - 502/956, 50phe C5W		2130	1950			4153500
Araldite - 502/956, 60phe C5W		2100	2240			4704000
Araldite - 502/956, 70phe C5W		1880	3170			5959600
Araldite - 502/956, 80phe C5W		1720	4710			8101200

Araldite - 502/956, 50phe 325mesh W		2160	2860			6177600
Araldite - 502/956, 60phe 325mesh W		1910	2780			5309800
Araldite - 502/956, 70phe 325mesh W		1820	3210			5842200
Araldite - 502/956, 80phe 325mesh W		1640	4550			7462000
Araldite - 502/956, 90phe 325mesh W		1520	8400			12768000
Arsenic tri sulphide As <sub>2</sub> S <sub>3</sub>	1400	2580	3200	8756480000	6272000000	8256000
Bacon P38	2170	4000	1900	12506180000	8946910000	7600000
Bearing babbit		2300	10100			23230000
Beryllium	8880	12890	1870	15788971000	1.47458E+11	24104300
Bismuth	1100	2200	9800	23716000000	11858000000	21560000
Boron carbide		11000	2400			26400000
Boron nitride	3860	5030	1965	-8839159500	29277714000	9883950
Brass - yellow, 70% Cu, 30% Zn	2100	4700	8640	1.14653E+11	38102400000	40608000
Brick		4300	1700			7310000
Cadmium	1500	2800	8600	28724000000	19350000000	24080000
Carbon -pyrolytic, soft, variable properties		3310	2210			7315100
Carbon - vitreous, very hard material	2680	4260	1470	5560716000	10558128000	6262200
Carbon - vitreous, Sigradur K		4630	1590			7361700
Columbium (same as Niobium) m.p. 2468°C	2100	4920	8570	1.31861E+11	37793700000	42164400
Concrete		3100	2600			8060000
Copper, rolled	2270	5010	8930	1.32113E+11	46015397000	44739300
DER317 - 9phr DEH20, 110phr W, r3	960	2180	2040	5934768000	1880064000	4447200

DER317 - 9phr DEH20, 115phr W, r3		1930	2370			4574100
DER317 - 9phr EH20, 910phr T1167, r3		1500	7270			10905000
DER317 - 10.5phr DEH20 rt, outgass		2750	1180			3245000
DER317 - 10.5phr DEH20, 110phr W, r3		2070	2230			4616100
DER317 - 13.5phr mpda, 50phr W, r1		2400	1600			3840000
DER317 - 13.5phr mpda, 100phr W, r1		2190	2030			4445700
DER317 - 13.5phr mpda, 250phr W, r1	930	1860	3400	5881320000	2940660000	6324000
DER332 - 10phr DEH20, rt cure 48 hours		2600	1200			3120000
DER332 - 10phr DEH20, 120phr alumina, r2	1620	3180	1760	8559936000	4618944000	5596800
DER332 - 10.5phr DEH20, 10phr alumina, r2		2610	1260			3288600
DER332 - 10.5phr DEH20, 14phr alumina, r2		2650	1290			3418500
DER332 - 10.5phr DEH20, 30phr alumina, r2		2750	1370			3767500
DER332 - 11phr DEH20, 14phr alumina, r10		2710	1290			3495900
DER332 - 11phr DEH20, 150phr alumina, r2		3250	1830			5947500
DER332 - 11phr DEH20, 150phr alumina, 50phr LP3, rt		2350	1720			4042000
DER332 - 14phr mpda, 30phr LP3, 70°C cure		2590	1250			3237500
DER332 - 15phr mpda, 60°C cure	1150	2680	1210	5490254000	1600225000	3242800
DER332, 15phr mpda, 25phr LP3, 76°C cure	1180	2550	1240	4609948000	1726576000	3162000
DER332 - 15phr mpda, 30phr LP3, 80°C cure		2660	1240			3298400
DER332 - 15phr mpda, 50phr alumina, 60°C cure	1430	2800	1490	5587798000	3046901000	4172000
DER332 - 15phr mpda, 60phr alumina, 80°C cure	1450	2780	1540	5426036000	3237850000	4281200

DER332 - 15phr mpda, SiC, r5		3900	2240			8736000
DER332 - 15phr mpda, SiC, 25phr LP3, r5		3750	2150			8062500
DER332 - 15phr mpda, 6 micron W, r5		1750	6450			11287500
DER332 - 50phr V140, rt cure	970	2340	1130	4060994000	1063217000	2644200
DER332 - 64phr V140, rt cure		2360	1130			2666800
DER332 - 75phr V140, rt cure		2350	1120			2632000
DER332 - 100phr V140, rt cure		2320	1100			2552000
DER332 - 100phr V140, 30phr LP3, r8	1130	2270	2550	6627705000	3256095000	5788500
DER332 - 100phr V140, 30phr LP3, r9		2360	1160			2737600
DER332 - 100phr V140, 50phr LP3, r8		2320	1130			2621600
DER332 - 50phr V140, 50phr St. Helens Ash,60°C		2430	1940			4714200
Duraluminin 17S	3130	6320	2790	56772594000	27333351000	17632800
Duxseal		1490	1680			2503200
E.pox.e glue, EPX-1 or EPX-2, 100phA of B		2440	1100			2684000
Eccosorb - CR 124 - 2PHX of Y		2620	4590			12025800
Ecosorb - MF 110		2610	1600			4176000
Ecosorb - MF 112		2400	2190			5256000
Ecosorb - MF 114		2290	2900			6641000
Ecosorb - MF 116		2450	3690			9040500
Ecosorb - MF 124		2600	4500			11700000
Eccosorb - MF 190		2670	4450			11881500
Epon - 828, mpda	1230	2829	1210	6022703610	1830609000	3423090



Epotek - 301		2640	1080			2851200
Epotek - 330		2570	1140			2929800
Epotek - H70S		2910	1680			4888800
Epotek - V6, 10phA of B, r6		2610	1230			3210300
Epotek - V6, 10phA of B, r7		2550	1230			3136500
Epotek - V6, 10phA of B, 20phA LP3, r6		2600	1250			3250000
Epotek - V6, 10phA of B, 20phA LP3, r7		2550	1260			3213000
Fused silica (Fused Quartz)	3750	5700	2200	9603000000	30937500000	12540000
Germanium, mp=937.4°C, transparent to infrared		5410	5470			29592700
Glass - corning 0215 sheet		5660	2490			14093400
Glass - crown	2800	5100	2240	23139200000	17561600000	11424000
Glass - FK3	2850	4910	2260	17770606000	18356850000	11096600
Glass - FK6 (large minimum order)	2540	4430	2280	15325476000	14709648000	10100400
Glass - flint		4500	3600			16200000
Glass - macor machinable code 9658		5510	2540			13995400
Glass - pyrex	3280	5640	2240	23055872000	24098816000	12633600
Glass - quartz		5500	2200			12100000
Glass - silica		5900	2200			12980000
Glass - soda lime	3439	5664	2520			14273280
Glass - TIK		4380	2380			10424400
Glucose		3200	1560			4992000
Gold - hard drawn	1200	3240	19700	1.50067E+11	28368000000	63828000

Granite	2700	6500	2710			17615000
Hafnium, mp=2150°C, used in reactor control rods		3840	13290			51033600
Hydrogen, solid at 4.2K		2190	89			194910
Hysol - CAW795/25 phr HW796 50°C		2700	1180			3186000
Hysol - C8-4143/3404		2850	1580			4503000
Hysol - C9-4183/3561		2920	1480			4321600
Hysol - C9-4183/3561, 15phe C5W		2620	1800			4716000
Hysol - C9-4183/3561, 30phe C5W		2490	2140			5328600
Hysol - C9-4183/3561, 45phe C5W		2300	2660			6118000
Hysol - C9-4183/3561, 57.5phe C5W		2160	3270			7063200
Hysol - EE0067/H3719 76°C, formerly C9-H905		2530	1930			4882900
Hysol - EE4183/HD3469 90°C		2990	1570			4694300
Hysol - EE4183/HD3469, 20phr 3:1 Alumina		3070	1760			5403200
Hysol - ES 4212, 1:1		2320	1500			3480000
Hysol - ES 4412, 1:1		2020	1680			3393600
Hysol R8-2038/3404		2590	1180			3056200
Hysol R9-2039/3404		2590	1130			2926700
Hysol R9-2039/3469		2610	1170			3053700
Hysol R9-2039/3561		2530	1180			2985400
Hysol R9-2039/3561, 427phr WO3		2150	3510			7546500
Ice	1980	3990	917	7408718100	3595006800	3658830
Inconel	3000	5700	8280	1.19977E+11	74520000000	47196000

Indium		2560	7300			18688000
Iron	3200	5900	7690	1.10198E+11	78745600000	45371000
Iron - cast	2600	4600	7220	55160800000	48807200000	33212000
Lead	700	2200	11200	43232000000	5488000000	24640000
Lead metaniobate		3300	6200			20460000
Lithium niobate - 36°C, rotated Y-cut		7080	4700			33276000
Magnesium - various types listed in ref "M"	3000	5800	1738	27182320000	15642000000	10080400
Marble		3800	2800			10640000
Molybdenum	3400	6300	10000	1.657E+11	1.156E+11	63000000
Monel	2700	5400	8820	1.28596E+11	64297800000	47628000
Nickel	3000	5600	8840	1.18102E+11	79560000000	49504000
Niobium, m.p.= 2468°C	2100	4920	8570	1.31861E+11	37793700000	42164400
Paraffin		1940	910			1765400
Phillips 66 "Crystallor"	1030	2170	830	2147293000	880547000	1801100
Platinum	1730	3260	21400	99334520000	64048060000	69764000
Poco - DFP-1	1730	3090	1810	6447763000	5417149000	5592900
Poco - DFP-1C	1810	3200	3200	11800960000	10483520000	10240000
Polyester casting resin		2290	1070			2450300
Porcelain		5900	2300			13570000
PSN, potassium sodium niobate		6940	4460			30952400
Pressed graphite		2400	1800			4320000
PZT 5H - Vernitron		4440	7430			32989200

PZT - Murata		4720	7950			37524000
PVDF		2300	1790			4117000
Quartz - X-cut	2200	5750	2650	61963625000	12826000000	15237500
Resin Formulators - RF 5407		3060	2160			6609600
Resin Formulators - RF 5407, 30 PHR LP3		2560	1920			4915200
Rubidium, mp=38.9, a "getter" in vacuum tubes		1260	1530			1927800
Salt - NaCl, crystalline, X- direction		4780	2170			10372600
Sapphire (aluminum oxide) Z-axis	6040	11100	3990	2.00485E+11	1.45562E+11	44289000
Scotch tape - 0.0025" thick		1900	1160			2204000
Scotchcast XR5235, 38 pha B, rt cure		2480	1490			3695200
Scotchply SP1002 (a laminate with fibers)		3250	1940			6305000
Scotchply XP 241		2840	650			1846000
Silicon (100) (very anisotropic (approx))	5840	8430	2340	6677658000	79807104000	19726200
Silicon carbide	7270	13060	3217	2.08648E+11	1.70028E+11	42014020
Silicon nitride	6250	11000	3270	1.40201E+11	1.27734E+11	35970000
Silver	1600	3600	10600	83104000000	27136000000	38160000
Silver epoxy, e-solder 3022	980	1900	2710	4577732000	2602684000	5149000
Slate		4500	3000			13500000
Steel - mild	3200	5900	7800	1.11774E+11	79872000000	46020000
Steel - stainless 347, Zs = 24.5 Mrayl	3100	5790	7890	1.12859E+11	75822900000	45683100
Stycast - 1264, rt cure		2220	1190			2641800
Stycast - 1264, 45pha, 600pha W, r6		1650	4710			7771500

Stycast - 1264, 45pha, 800pha W, r6		1570	5500			8635000
Stycast - 1264, 45pha, vac. impreg. W, rt		1710	6030			10311300
Stycast - 1267		2570	1160			2981200
Stycast - 1970, costs \$109.00/lb		3200	1900			6080000
Stycast - 2651-40 9phr catalyst 9, rt cure		2770	1500			4155000
Stycast - 2651-40 9phr catalyst 9, 10phr SiC		2880	1570			4521600
Stycast - 2651-40 9phr catalyst 9, 20phr SiC		2950	1630			4808500
Stycast - 2651-40 9phr catalyst 9, 25phr SiC	1500	2900	1670	6529700000	3757500000	4843000
Stycast - 2741, 1:1		2290	1170			2679300
Sulphur - 9 isotropic forms exist, mp 112°C		1350	2000			2700000
Tantalum - mp=2996°C, very inert, hard	2900	4100	16600	-166000000	1.39606E+11	68060000
Tapox epoxy		2480	1110			2752800
Techform EA700, brittle material		2630	1200			3156000
Teflon		1390	2140			2974600
Thorium - mp=1700°C, fissionable, high melting oxide	1560	2400	11300	10088640000	27499680000	27120000
Tin	1700	3300	7300	37303000000	21097000000	24090000
Titanium - mp=1725 C	3100	6100	4480	80595200000	43052800000	27328000
Titanium carbide - mp=3140 C	5160	8270	5150	77979755000	1.37122E+11	42590500
Tracon - 401 ST		2970	1620			4811400
Tracon - 2135 D		2450	1030			2523500
Tracon - 2143 D		2370	1050			2488500
Tracon - 2162 D		2020	1190			2403800

Tracon - 3011		2120	1200			2544000
Tungsten	2900	5200	19400	1.98268E+11	1.63154E+11	100880000
Unobtainium (properties are proprietary!)						0
Uranium	2000	3400	18500	65860000000	74000000000	62900000
Uranium dioxide		5180	2116			10960880
Vanadium, mp=1890C	2780	6000	6030	1.23875E+11	46602252000	36180000
Wood - balsa		800	100			80000
Wood - cork		500	240			120000
Wood - cork		1150	130			149500
Wood - oak		000	720			2880000
Wood - pine		500	450			1575000
Zinc (often very granular)	2400	200	7000	42840000000	40320000000	29400000
Zinc oxide	2950	6400	5680	1.33792E+11	49430200000	36352000
Zircaloy	2360	4720	9360	1.04263E+11	52131456000	44179200
Zirconium, mp=1852°C, used in poison ivy lotion	2250	4650	6480	74503800000	32805000000	30132000

Table D-2. Properties of plastic materials.

Material	$V_s$ (m/s)	$V_L$ (m/s)	Density (kg/m <sup>3</sup> )	Lame Con. (lambda)	Lame Con. (mu)	$Z_L$ (kg/s-m <sup>2</sup> )
ABS, Beige		2230	1030			2296900
ABS, Black, Injection molded (Grade T, Color #4500, "Cycolac")		2250	1050			2362500
ABS, Grey, Injection molded (Grade T, Color #GSM 32627)		2170	1070			2321900
Acrylic, Clear, Plexiglas G Safety Glazing		2750	1190			3272500

Acrylic, Plexiglas MI-7		2610	1180			3079800
Bakelite		1590	1400			2226000
Cellulose Butyrate		2140	1190			2546600
Delrin, Black		2430	1420			3450600
Ethyl vinyl acetate, VE-630 (18% Acetate)		1800	940			1692000
Ethyl vinyl acetate, VE-634 (28% Acetate)		1680	950			1596000
Kydex, PVC Acrylic Alloy Sheet		2218	1350			2994300
Lexan, Polycarbonate		2300	1200			2760000
Lustran, SAN		2510	1060			2660600
Mylar		2540	1180			2997200
Kodar PETG, 6763, Copolyester		2340	1270			2971800
Melopas		2900	1700			4930000
Nylon, 6/6	1100	2600	1120	4860800000	1355200000	2912000
Nylon, Black, 6/6		2770	1140			3157800
Parylene C (byMM)		2150	1400			3010000
Parylene C (by Vikng)		2200	1180			2596000
Parylene D		2100	1360			2856000
Polycarbonate, Black, Injection molded (Grade 141R, Color No.701,"Lexan")		2270	1220			2769400
Polycarbonate, Blue, Injection molded (Grade M-40, Color No. 8087, "Merlon")		2260	1200			2712000
Polycarbonate, Clear, Sheet Material		2270	1180			2678600
Polyethylene	540	1950	900	2897370000	262440000	1755000
Polyethylene, high density, LB-861		2430	960			2332800

Polyethylene, low density, NA-117	540	1950	920	2961756000	268272000	1794000
Polyethylene DFDA 1137 NT7		1900	900			1710000
Polyethylene oxide, WSR 301		2250	1210			2722500
Polypropylene, Profax 6432, Hercules		2740	880			2411200
Polypropylene, White, Sheet Material		2660	890			2367400
Polystyrene, "Fostarene 50"		2450	1040			2548000
Polystyrene, "Lustrex", Injection molded (Resin #HF55-2020-347)		2320	1040			2412800
Polystyrene, Styron 666	1150	2400	1050	3270750000	1388625000	2520000
Polyvinyl butyral, Butacite, (used to laminate safety glass together)		2350	1110			2608500
PSO, Polysulfone		2240	1240			2777600
PVC, Grey, Rod Stock (normal impact grade)		2380	1380			3284400
Styrene Butadiene, KR 05 NW		1920	1020			1958400
TPX-DX845, Dimethyl pentene polymer		2220	830			1842600
Valox, Black, (glass filled polybutalene teraphlate "PTB")		2530	1520			3845600
Vinyl, Rigid		2230	1330			2965900

Table D-3. Properties of liquids

Material	$V_s$ (m/s)	$V_L$ (m/s)	Density (kg/m <sup>3</sup> )	Lame Con. ( $\lambda$ )	Lame Con. ( $\mu$ )	$Z_L$ (kg/s-m <sup>2</sup> )
Acetate, butyl		1270	871			1106170
Acetate, ethyl, C <sub>4</sub> H <sub>8</sub> O <sub>2</sub>		1190	900			1071000
Acetate, methyl, C <sub>3</sub> H <sub>6</sub> O <sub>2</sub>		1210	934			1130140
Acetate, propyl		1180	891			1051380



Acetone, (CH <sub>3</sub> ) <sub>2</sub> CO at 25°C		1174	791			928634
Acetonitrile, C <sub>2</sub> H <sub>3</sub> N		1290	783			1010070
Acetonyl acetone, C <sub>6</sub> H <sub>10</sub> O <sub>2</sub>		1400	729			1020600
Acetylendichloride, C <sub>2</sub> H <sub>2</sub> Cl <sub>2</sub>		1020	1260			1285200
Alcohol, butyl, C <sub>4</sub> H <sub>9</sub> OH at 30°C		1240	810			1004400
Alcohol, ethanol, C <sub>2</sub> H <sub>5</sub> OH, at 25°C		1207	790			953530
Alcohol, furfuryl, C <sub>5</sub> H <sub>4</sub> O <sub>2</sub>		1450	1135			1645750
Alcohol, isopropyl, 2-Propanol, at 20°C		1170	786			919620
Alcohol, methanol, CH <sub>3</sub> OH, at 25°C		1103	791			872473
Alcohol, propyl (n) C <sub>3</sub> H <sub>7</sub> OH at 30°C		1220	804			980880
Alcohol, t-amyl, C <sub>5</sub> H <sub>9</sub> OH		1200	810			972000
Alkazene 13, C <sub>15</sub> H <sub>24</sub>		1320	860			1135200
Aniline, C <sub>6</sub> H <sub>5</sub> NH <sub>2</sub>		1690	1022			1727180
Argon, liquid at 87K		840	1430			1201200
Benzene, C <sub>6</sub> H <sub>6</sub> , at 25°C		1295	870			1126650
Benzol		1330	878			1167740
Benzol, ethyl		1340	868			1163120
Bromobenzene C <sub>6</sub> H <sub>5</sub> Br at 22°C		1167	1522			1776174
Bromoform, CHBr <sub>3</sub>		920	2890			2658800
t-Butyl chloride, C <sub>4</sub> H <sub>9</sub> Cl		980	840			823200
Butyrate, ethyl		1170	877			1026090
CARBITOLTM, C <sub>6</sub> H <sub>14</sub> O <sub>3</sub>		1460	988			1442480

Carbon disulphide, CS <sub>2</sub> at 25°C		1149	1260			1447740
Carbon disulphide, CS <sub>2</sub> , 25°C, 3 GHz		1310	1221			1599510
Carbon tetrachloride, CCl <sub>4</sub> , at 25°C		926	1594			1476044
Cesium at 28.5°C the melting point		967	1880			1817960
Chloro-benzene, C <sub>6</sub> H <sub>5</sub> Cl, at 22°C		1304	1106			1442224
Chloro-benzene, C <sub>6</sub> H <sub>5</sub> Cl		1300	1100			1430000
Chloroform, CHCl <sub>3</sub> , at 25°C		987	1490			1470630
Cyclohexanol, C <sub>6</sub> H <sub>12</sub> O		1450	962			1394900
Cyclohexanone, C <sub>6</sub> H <sub>10</sub> O		1420	948			1346160
Diacetyl, C <sub>4</sub> H <sub>6</sub> O <sub>2</sub>		1240	990			1227600
1,3 Dichloroisobutane C <sub>4</sub> H <sub>8</sub> Cl <sub>2</sub>		1220	1140			1390800
Diethyl ketone		1310	813			1065030
Dimethyl phthalate, C <sub>8</sub> H <sub>10</sub> O <sub>4</sub>		1460	1200			1752000
Dioxane		1380	1033			1425540
Ethanol amide, C <sub>2</sub> H <sub>7</sub> NO, at 25°C		1724	1018			1755032
Ethyl ether, C <sub>4</sub> H <sub>10</sub> O, at 25°C		985	713			702305
d-Fenchone		1320	940			1240800
Florosilicone oil, Dow FS-1265		760				
Formamide, CH <sub>3</sub> NO		1620	1134			1837080
Furfural, C <sub>5</sub> H <sub>4</sub> O <sub>2</sub>		1450	1157			1677650
Fluorinert FC-40		640	1190			761600
Fluorinert FC-70		687	1940			1332780

Fluorinert FC-72		512	1680			860160
Fluorinert FC-75		585	1760			1029600
Fluorinert FC-77		595	1780			1059100
Fluorinert FC-104		575	1760			1012000
Fluorinert FG-43		655	1850			1211750
Fluoro-benzene, C <sub>6</sub> H <sub>5</sub> F, at 22°C		1180	1024			1208320
Freon, TF		716	1570			1124120
Gallium at 30°C mp=28.8°C (expands 3% freezes)		2870	6090			17478300
Gasoline		1250	803			1003750
Glycerin - CH <sub>2</sub> OHCHOHCH <sub>2</sub> OH, at 25°C		1904	1260			2399040
Glycol - 2,3 butylene		1480	1019			1508120
Glycol - diethylene C <sub>4</sub> H <sub>10</sub> O <sub>3</sub>		1580	1116			1763280
Glycol - ethylene 1,2-ethanediol @ 25°C		1658	1113			1845354
Glycol - ethylene Preston II		1590	1108			1761720
Glycol - polyethylene 200		1620	1087			1760940
Glycol - polyethylene 400		1620	1060			1717200
Glycol - polypropylene (Polyglycol P-400) at 38°C		1300				
Glycol - polypropylene (Polyglycol P-1200) at 38°C		1300				
Glycol - polypropylene (Polyglycol E-200) at 29°C		1570				
Glycol - tetraethylene C <sub>8</sub> H <sub>18</sub> O <sub>6</sub>		1580	1120			1769600
Glycol, triethylene, C <sub>6</sub> H <sub>14</sub> O <sub>4</sub>		1610	1123			1808030
Helium-4, liquid at 0.4K		238	147			34986

Helium-4, liquid at 2K		227	145			32915
Helium-4, liquid at 4.2K		183	126			23058
n-Hexane, C <sub>6</sub> H <sub>14</sub> , liquid at 30°C		1103	659			726877
n-Hexanol, C <sub>6</sub> H <sub>14</sub> O		1300	819			1064700
Honey, sue bee orange		2030	1420			2882600
Hydrogen, liquid at 20°K		1190	70			83300
Iodo-benzene, C <sub>6</sub> H <sub>5</sub> I, at 22°C		1104	1183			1306032
Isopentane, C <sub>5</sub> H <sub>12</sub>		992	620			615040
Kerosene		1324	810			1072440
Linalool		1400	884			1237600
Mercury at 25.0°C		1450	13500			19575000
Mesityloxide, C <sub>6</sub> H <sub>16</sub> O		1310	850			1113500
Methylethylketone		1210	805			974050
Methylene iodide		980				
Methyl naphthalene, C <sub>11</sub> H <sub>10</sub>		1510	1090			1645900
Monochlorobenzene, C <sub>6</sub> H <sub>5</sub> Cl		1270	1107			1405890
Morpholine, C <sub>4</sub> H <sub>9</sub> NO		1440	1000			1440000
Neon, liquid at 27K		1200	1200			1440000
Nicotin, C <sub>10</sub> H <sub>14</sub> N <sub>2</sub> , at 20°C		1490	1010			1504900
Nitrobenzene, C <sub>6</sub> H <sub>6</sub> NO <sub>2</sub> , at 25°C		1463	1200			1755600
Nitrogen N <sub>2</sub> , liquid at 77K		860	800			688000
Nitromethane CH <sub>3</sub> NC <sub>2</sub>		1330	1130			1502900

Oil - baby		1430	821			1174030
Oil - castor, C11H10O10 @ 25°C		1477	969			1431213
Oil - castor, @ 20.2°C @ 4.224 MHz		1507	942			1419594
Oil - corn		1460	922			1346120
Oil - diesel		1250				
Oil - gravity fuel AA		1490	990			1475100
Oil - jojoba		1455	1170			1702350
Oil - linseed		1460	940			1372400
Oil - linseed		1770	922			1631940
Oil - mineral, light		1440	825			1188000
Oil - mineral, heavy		1460	843			1230780
Oil - olive		1445	918			1326510
Oil - paraffin		1420	835			1185700
Oil - peanut		1436	914			1312504
Oil - SAE 20		1740	870			1513800
Oil - SAE 30		1700	880			1496000
Oil - silicon Dow 200, 1 centistoke		960	818			785280
Oil - silicon Dow 200, 10 centistoke		968	940			909920
Oil - silicon Dow 200, 100 centistoke		980	968			948640
Oil - silicon Dow 200, 1000 centistoke		990	972			962280
Oil - silicon Dow 704 @ 79°F		1409	1020			1437180
Oil - silicon Dow 705 @ 79°F		1458	1150			1676700

Oil - silicon Dow 710 @ 20°C		1352	1110			1500720
Oil - safflower		1450	900			1305000
Oil - soybean		1430	930			1329900
Oil - sperm		1440	880			1267200
Oil - sunflower		1450	920			1334000
Oil - transformer		1390	920			1278800
Oil - wintergreen (methyl salicylate)		1380	1600			2208000
Oxygen, O <sub>2</sub> , liquid at 90K		900	1110			999000
Paraffin at 15°C		1300				
n-Pentane, C <sub>5</sub> H <sub>12</sub> , liquid at 15°C		1027	626			642902
Polypropylene oxide (Ambiflo) at 38°C		1370				
Potassium at 100°C, mp=63.7°C ('M' other temps)		1820	830			1510600
Pyridine		1410	982			1384620
Sodium, liquid at 300°C (see 'M' for other temps)		2420	8810			21320200
Solvesso #3		1370	877			1201490
Sonotrack couplant		1620	1040			1684800
Tallow at 16°C		390				
Thallium, mp=303.5°C, used in photocells		1620	11900			19278000
Trichorethylene		1050	1050			1102500
Turpentine, at 25°C		1255	880			1104400
Univis 800		1350	870			1174500
Water - heavy, D <sub>2</sub> O		1400	1104			1545600

Water - liquid at 20°C		1480	1000			1480000
Water - liquid at 25°C		1496.7	998			1493706.6
Water - liquid at 30°C		1509	1000			1509000
Water - liquid at 60°C (temps to 500°F in °C)		1550	1000			1550000
Water - salt 10%		1470				
Water - salt 15%		1530				
Water - salt 20%		1600				
Water - sea, at 25°C		1531	1025			1569275
Xenon - liquid at 166K		630	2860			1801800
Xylene Hexafluoride, C <sub>8</sub> H <sub>4</sub> F <sub>6</sub> , at 25°C		879	1370			1204230
m-Xylol, C <sub>8</sub> H <sub>10</sub>		1320	864			1140480

To the best of our knowledge, this work does not infringe upon anyone's copyright nor violate any proprietary rights, and none of the ideas, techniques, quotations, or any other material comes from the work of other people. The results relating to this work have been fully acknowledged in accordance with the standard referencing practices.